

Wrocław University of Technology-
Centre of Advanced Materials and Nanotechnology

Materials Science

**International Conference on Sol-Gel Materials
SGM2001, Rokosowo, Poland**

Vol. 20

•

No.

2

•

2002



Oficyna Wydawnicza Politechniki Wrocławskiej

Materials Science is an interdisciplinary journal devoted to experimental and theoretical research into the synthesis, structure, properties and applications of materials.

Among the materials of interest are:

- glasses and ceramics
- sol-gel materials
- photoactive materials (including materials for nonlinear optics)
- laser materials
- photonic crystals
- semiconductor micro- and nanostructures
- piezo-, pyro- and ferroelectric materials
- high- T_c superconductors
- magnetic materials
- molecular materials (including polymers) for use in electronics and photonics
- novel solid phases
- other novel and unconventional materials

The broad spectrum of the areas of interest reflects the interdisciplinary nature of materials research. Papers covering the modelling of materials, their synthesis and characterisation, physicochemical aspects of their fabrication, properties and applications are welcome. In addition to regular papers, the journal features issues containing conference papers, as well as special issues on key topics in materials science.

Materials Science is published under the auspices of the Centre of Advanced Materials and Nanotechnology of the Wrocław University of Technology, in collaboration with the Institute of Low Temperatures and Structural Research of the Polish Academy of Sciences and the Wrocław University of Economics.

All accepted papers are placed on the Web page of the journal and are available at the address:
<http://MaterialsScience.pwr.wroc.pl>

Editor-in-Chief

Juliusz Sworakowski

Institute of Physical and Theoretical Chemistry
Wrocław University of Technology
Wybrzeże Wyspiańskiego 27
50-370 Wrocław, Poland
sworakowski@pwr.wroc.pl

Associate Editors

Wiesław Stręk

Institute of Low Temperature
and Structure Research
Polish Academy of Sciences
P.O. Box 1410
50-950 Wrocław 2, Poland
strek@int.pan.wroc.pl

Jerzy Hanuza

Department of Bioorganic Chemistry
Faculty of Industry and Economics
Wrocław University of Economics
Komandorska 118/120
53-345 Wrocław, Poland
hanuza@credit.ae.wroc.pl

Scientific Secretary

Krzysztof Maruszewski

Institute of Materials Science and Applied Mechanics
Wrocław University of Technology
Wybrzeże Wyspiańskiego 27
50-370 Wrocław, Poland
maruszewski@pwr.wroc.pl

Advisory Editorial Board

Michel A. Aegerter, Saarbrücken, Germany
Ludwig J. Balk, Wuppertal, Germany
Victor E. Borisenko, Minsk, Belarus
Mikheylo S. Brodyn, Kyiv, Ukraine
Maciej Bugajski, Warszawa, Poland
Alexander Bulinski, Ottawa, Canada
Roberto M. Faria, Sao Carlos, Brazil
Reimund Gerhard-Multhaupt, Potsdam, Germany
Paweł Hawrylak, Ottawa, Canada
Jorma Hölsä, Turku, Finland
Alexander A. Kaminskii, Moscow, Russia
Wacław Kasprzak, Wrocław, Poland
Andrzej Kłonkowski, Gdańsk, Poland
Seiji Kojima, Tsukuba, Japan
Shin-ya Koshihara, Tokyo, Japan
Marian Kryszewski, Łódź, Poland
Krzysztof J. Kurzydłowski, Warsaw, Poland
Jerzy M. Langer, Warsaw, Poland
Janina Legendziewicz, Wrocław, Poland
Benedykt Licznarski, Wrocław, Poland

Tadeusz Luty, Wrocław, Poland
Joop H. van der Maas, Utrecht, The Netherlands
Bolesław Mazurek, Wrocław, Poland
Gerd Meyer, Cologne, Germany
Jan Misiewicz, Wrocław, Poland
Jerzy Mroziński, Wrocław, Poland
Robert W. Munn, Manchester, U.K.
Krzysztof Nauka, Palo Alto, CA, U.S.A.
Stanislav Nešpůrek, Prague, Czech Republic
Romek Nowak, Santa Clara, CA, U.S.A.
Tetsuo Ogawa, Osaka, Japan
Renata Reisfeld, Jerusalem, Israel
Marek Samoć, Canberra, Australia
Jan Stankowski, Poznań, Poland
Leszek Stoch, Cracow, Poland
Jan van Turnhout, Delft, The Netherlands
Jacek Ulański, Łódź, Poland
Walter Wojciechowski, Wrocław, Poland
Vladislav Zolin, Moscow, Russia

The Journal is supported by the State Committee for Scientific Research

Editorial Office

Anna Sofińska
Łukasz Maciejewski

Editorial layout

Hanna Basarowa

Cover design

Zofia i Dariusz Godlewscy

Printed in Poland

© Copyright by Oficyna Wydawnicza Politechniki Wrocławskiej, Wrocław 2002

Contents

Papers presented at the International Conference on Sol-Gel Materials, SGM 2001, Rokosowo, Poland

R. Reisfeld, Rare earth complexes in sol-gel glasses.....	5
V. E. Gaishun, O.I. Tulenkova, I.M. Melnichenko, S.A. Baryshnin, Y.A. Potapenok, A.P. Xlebo- kazov, W. Stręk, Preparation and properties of colloidal nanosize silica dioxide for polishing of monocrystalline silicon wafers.....	19
S. A. Geveluyk, I.K. Doycho, L.P. Prokopovich, E. Rysiakiewicz-Pasek, E.D. Safronsky, Hu- midity dependencies of porous sol-gel and silica glass linear sizes	23
V. S. Gurin, A.A. Alexeenko, V.B. Prakapenka, D.L. Kovalenko, K.V. Yumashev, P.V. Proko- shin, Incorporation of copper and its oxides and chalcogenides into silica sol-gel materials	29
D. Hreniak, W. Stręk, P. Mazur, Preparation, spectroscopy and morphology of Nd:YAG nanos- tructures	39
L. Q. Minh, N.T. Huong, C. Barthou, P. Benalloul, W. Stręk, T.K. Anh, Eu^{3+} - and Er^{3+} -doped $\text{SiO}_2\text{-TiO}_2$ sol-gel films for active planar waveguides.....	47
E. N. Poddenezhny, A.A. Boika, B.V. Plusch, M.N. Kapshai, I.P. Kravchenko, I.M. Mel- nichenko, Role of fluorine ions in the formation of silica gel structure and gel glass.....	53
M. Przybyt, B. Białkowska, Enzyme electrodes constructed on the basis of oxygen electrode with oxidases immobilised by sol-gel technique.....	63

Regular papers

S. S. Gerashchenko, O.V. Miloslavskaya, Yu.N. Kharchenko, V.I. Kutko, N.M. Nesterenko, L. Macalik, K. Hermanowicz, M. Mączka, J. Hanuza, Bi-doping effect on the Jahn-Teller phase transition in $\text{CsDy}(\text{MoO}_4)_2$ crystal	81
J. Małecka, A. Kochel, J. Mroziński, $(\text{Ph}_4\text{P})_2[\text{ReCl}_5(\text{tcm})]$ – a new precursor of molecular mag- nets.....	91
C. R. Neri, A.P.J. Maestrin Prado, A.O. Ribeiro, O.A. Serra, Y. Iamamoto, Determination of the photodynamic activity of porphyrins: Potential photosensitizers for treatment of age-related macular degeneration	97

Rare earth complexes in sol-gel glasses*

RENATA REISFELD

Department of Inorganic and Analytical Chemistry, The Hebrew University,
91-904 Jerusalem, Israel, renata@vms.huji.ac.il

The origin of the spectra of rare earth ions arising from $f \rightarrow f$ and $f \rightarrow d$ transitions is discussed. The parity-forbidden luminescence of lanthanide ions can be strongly intensified by excitation via molecules characterized by high transition probabilities. Such behaviour opens a route for creation of a class of new sophisticated materials. Luminescent materials based on heteroaromatic lanthanide cryptates are attractive as labels for advanced time-resolved fluoroimmunoassays and molecular markers, their potential use is also conceivable in the field of luminescent displays, molecular photonics and highly luminescent materials in hybrid organic/inorganic glasses. The recent findings of lanthanide complexes trapped in sol-gel inorganic glasses based on silica and zirconia networks are discussed and the theoretical basis of their spectroscopy is presented.

Key words: *rare earths, electronic spectra*

1. Electronic spectra of rare earth ions

Rare earth (RE) ions incorporated in a solid or liquid environment show distinct spectral lines of absorption and emission due to the electronic transition within $4f^N$ shell configuration. Figure 1 shows an example partial energy diagram of a RE ion – Eu^{3+} – indicating splitting of the electronic levels due to spin-orbit interaction, which are further split by the ligand field (the j splitting). Figure 2 shows a similar diagram for Tb^{3+} .

Since the f orbital is strongly shielded from the outside ligands, the positions of the spectral lines vary only slightly with the environment, however, their intensities are strongly dependent on the host in which the rare earth is embedded [1–3].

The radiative intensities of the trivalent rare earth ions can be easily calculated by the use of Judd–Ofelt theory from the experimentally measured absorption spectra and theoretically calculated matrix element of the ion.

*The paper presented at the International Conference on Sol-Gel Materials, SGM 2001, Rokosowo, Poland.

The following approach is applied for $f \rightarrow f$ transition: the total oscillator strength P of a transition at frequency ν is given by

$$P(aJ; bJ') = \frac{8\pi^2 m \nu}{3h(2J+1)} \left[\frac{(n^2 + 2)^2}{9n} S_{ed} + nS_{md} \right] \quad (1)$$

The connection between integrated absorbance of an electric dipole with line-strength S is:

$$\int k(\lambda) d\lambda = \rho \frac{8\pi^3 m \nu}{3hc(2J+1)} \frac{1}{n} \frac{(n^2 + 2)^2}{9} S_{ed} \quad (2)$$

where $k(\lambda)$ is the absorption coefficient at the wavelength λ , ρ is the RE ion concentration, λ is the mean wavelength of the absorption band, J is the total angular momentum of the initial level and $n = n(\lambda)$ is the bulk index of refraction at wavelength λ . The factor $(n^2 + 2)^2/9$ represents the local field correction for the ion in a dielectric medium.

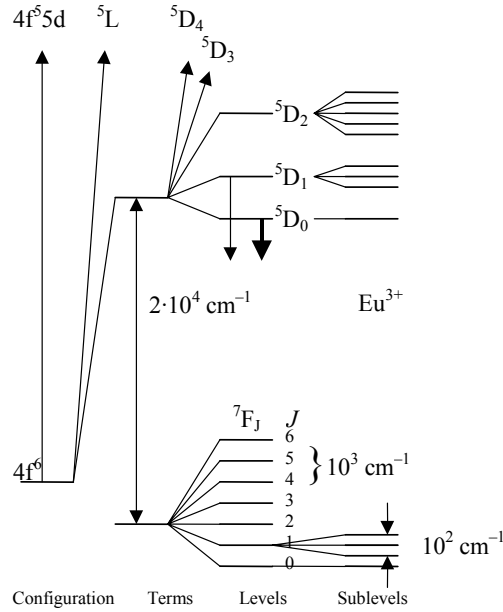
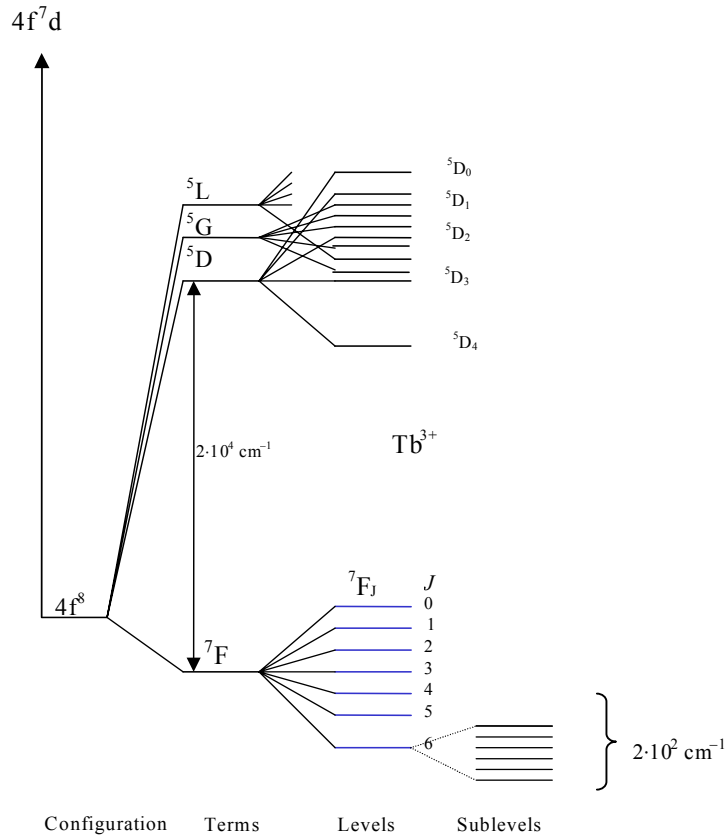


Fig. 1. Partial energy diagram for Eu(III) ion

The spontaneous emission rate is

$$A(aJ; bJ') = \frac{64\pi^4 \nu^3}{3hc^2(2J+1)} \left[\frac{n(n^2 + 2)^2}{9} S_{ed} + nS_{md} \right] \quad (3)$$

Fig. 2. Partial energy diagram for Tb^{3+} ion

in the case of electric dipole emission Eq. (3) takes the form of:

$$A(aJ; bJ') = \frac{64\pi\nu^3}{3hc^2(2J+1)} \left[\frac{n(n^2+2)^2}{9} \right] e^2 \sum_{t=2,4,6} \Omega_t | \langle (S, L)J \| U^{(t)} \| (S', L')J' \rangle |^2 \quad (4)$$

where Ω is the Judd–Offelt parameter, n is the index of refraction of the matrix. The integrated absorption cross-section is related to the oscillator strength by:

$$\int \sigma(\bar{\nu}) d\bar{\nu} = \frac{\pi e^2}{mc^2} P \quad (5)$$

where $\bar{\nu}$ is measured in inverse centimeters. For a Lorentzian line

$$\sigma(\nu) = \frac{\sigma_0}{1 + \frac{4(\nu - \nu_0)^2}{(\Delta\nu)^2}} \quad (6)$$

where $\Delta\nu$ is the full width at the half maximum, ν_0 is the frequency at the peak, and σ_0 is the peak cross-section. Then:

$$\int \sigma(\nu) d\nu = \frac{\pi}{2} \sigma_0 \Delta\nu \quad (7)$$

$$\sigma_0 = \frac{2e^2}{mc^2 \Delta\nu} P \quad (8)$$

Thus, for a given linewidth, the peak cross-section for stimulated emission is proportional to the oscillator strength. Equation (8) also shows the importance of the line width $\Delta\nu$ in the determination of the cross-section.

The peak induced emission cross-section is related to the radiative probability by the equation:

$$\sigma(\lambda p) = \frac{\lambda p^4}{8\pi c n^2 \Delta\lambda_{\text{eff}}} aJ : bJ' \quad (9)$$

where the effective line width $\Delta\lambda_{\text{eff}}$ is used, since for glasses the absorption and emission bands are characteristically asymmetrical.

The cross-section may also be written as:

$$\sigma_p \Delta\bar{\nu} = \int \sigma(\bar{\nu}) d\bar{\nu} = \frac{\lambda p^2}{8\pi c n^2} A(aJ; bJ') \quad (10)$$

The radiative lifetime of level J can be expressed in terms of the spontaneous emission probabilities as:

$$\tau_J^{-1} = \sum_{J'} A(J, J') \quad (11)$$

where the summation is over all terminal levels J' . The fluorescence-branching ratio from level J to J'' is given by

$$\beta_{JJ''} = \frac{A(J, J'')}{\sum_{J'} A(J, J')} \quad (12)$$

In addition to the spectroscopic properties, the Judd–Ofelt intensity parameters can also be used to estimate excited-state absorption and the probability of ion-ion interactions that enter into energy-transfer and fluorescence-quenching phenomena.

2. Relaxation processes in trivalent Re

Relaxation processes in trivalent Re include ion-ion energy transfer which can give rise to concentration quenching and non-exponential decay and relaxation by multiphonon emission which is usually essential to complete the overall scheme and can affect the quantum efficiency.

For low concentration of rare earth dopant ions, nonradiative decay mechanism is a multiphonon emission. The results of the theory of multiphonon emission in amorphous materials were recently summarized [4].

The *ab initio* calculation of the transition rate between two electronic states with the emission of p phonons involves a very complicated sum over phonon modes and intermediate states. Due to this complexity, these sums are extremely difficult to compute; however, it is just this complexity which permits a very simple phenomenological theory to be used. There are extremely large numbers of ways in which p phonons can be emitted and the sums over phonon modes and intermediate states are essentially a statistical average of matrix elements. In the phenomenological approach, it is assumed that the ratio of the p -th and $(p - 1)$ -th processes will be given by a coupling constant characteristic of the matrix in which the ion is embedded but not dependent on the rare-earth electronic states. For a given lattice at low temperature the spontaneous relaxation rate is given by

$$W(0) = Be^{\alpha\Delta E} \quad (13)$$

where B and α are characteristic of the host (α is negative). Thus, the graph of the spontaneous rate vs. energy gap will be a straight line when this approach is valid. Figure 3 presents an example of exponential behaviour of decay rate on the energy gap between the emitting level and the next lower level to which the energy decays. Experimental data show that the approach is very good for a large variety of hosts. In this way, all multiphonon rates can be inferred from a few measured rates.

The dominant emission process is the one which requires the least number of phonons to be emitted. The minimum number of phonons required for a transition between states separated by an energy gap ΔE is given by

$$p = \frac{\Delta E}{\hbar\omega_{\max}} \quad (14)$$

where $\hbar\omega_{\max}$ is the maximum energy of optical phonons. With increased temperature, stimulated emission of phonons by thermal phonons increases the relaxation rate W according to

$$W(T) = W(O) (1 + \bar{n} (\hbar\omega_{\max}))^P \quad (15)$$

where \bar{n} is the average occupation number of phonons of energy $\hbar\omega_{\max}$.

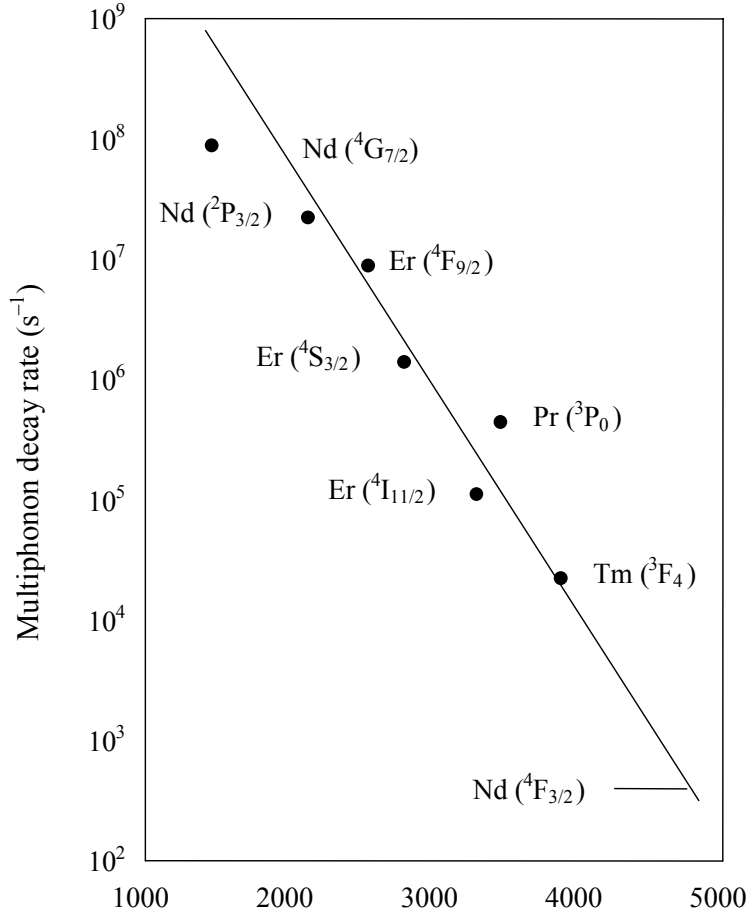


Fig. 3. An example of multiphonon decay for trivalent RE in a silicate glass

The non-radiative relaxation in the rare earth ions is related to their excited states population and is governed by the energy difference between the emitting level and the next lower level, separated by the number of phonons of the host [3, 4].

The presence of water or solvent molecules in the co-ordination sphere of the RE is often responsible for quenching of the luminescence via multiphonon relaxation. Mac-

rocyclic ligands such as cryptates shield the lanthanide ion from the solvent preventing the quenching effect. Luminescent properties of co-ordination compounds are widely used in chemical, biological and technological applications [5, 6].

In contrast to the spectra arising from $f \rightarrow f$ transitions, in all the trivalent rare earth ions having oscillator strength of $\sim 10^{-6}$, trivalent Ce^{3+} ion forms an exception as its spectrum arises from $f \rightarrow d$ transition.

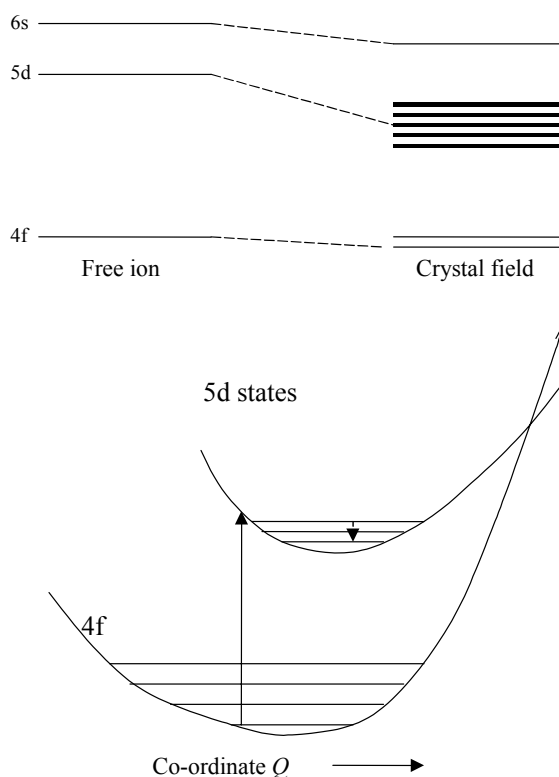


Fig. 4. Electronic levels (upper) and configurational diagram (lower) of Ce^{3+}

Neutral cerium atom has a $1s^2 2s^2 p^6 3s^2 p^6 d^{10} 4s^2 p^6 d^{10} f^2 5s^2 p^6 6s^2$ electronic configuration. In liquids and solids, Ce ions can occur in a trivalent or a tetravalent state, i.e. by losing its two $6s$ electrons and one or both of its $4f$ electrons. The trivalent state with a single $4f$ electrons is optically active; the resulting electronic energy level solids structure is shown in Fig. 4. When cerium enters a liquid or a solid, the expansion of the electron shells decreases the electrostatic interaction between the electrons resulting in a reduction of the energy of the excited states from their free ion values. This nephelauxetic shift increases with the degree of covalency of the cerium–anion bond. The spin-orbit interaction splits the $2f$ ground into two J states separated by $\sim 2200 \text{ cm}^{-1}$. The $(2J + 1)$ -fold degeneracy of these states is reduced by the ligand

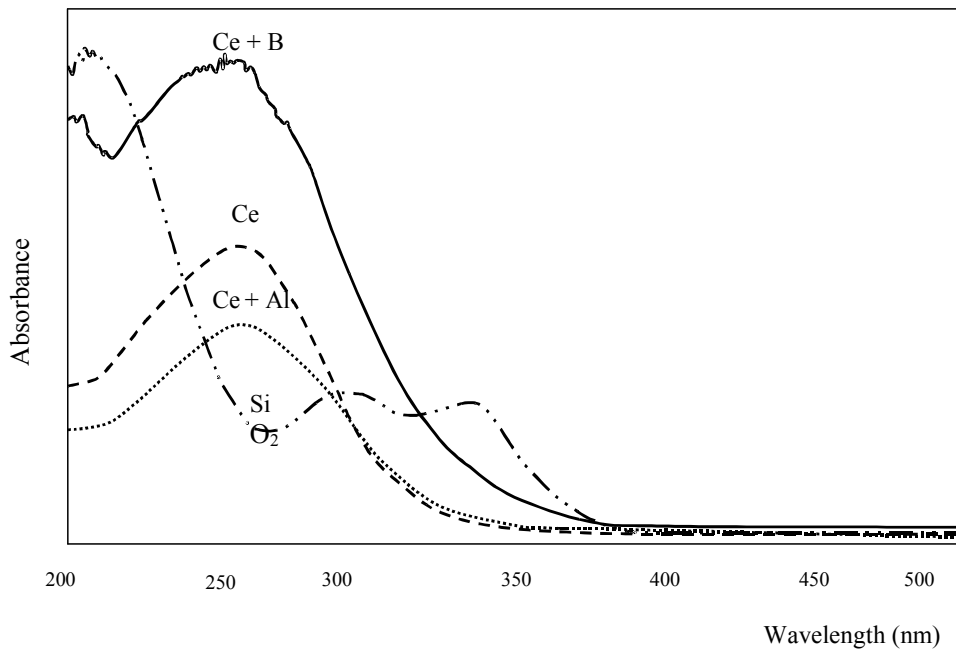


Fig. 5. Absorption spectrum of Ce³⁺ in silica glass prepared by the sol-gel method, the glasses with addition of Al³⁺ and B₂O₃ are also indicated in the figure

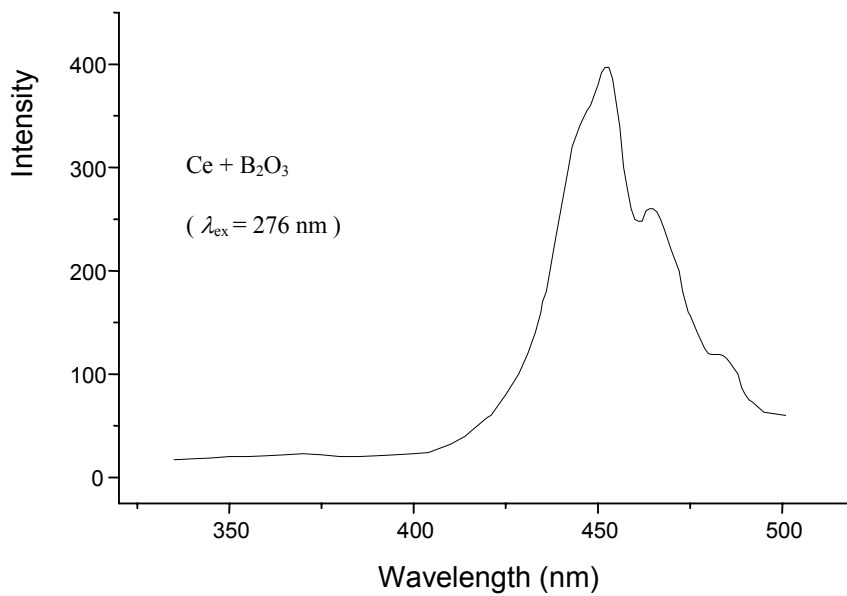


Fig. 6. Luminescent spectrum of Ce³⁺ in sol-gel silica glass with addition of B₂O₃

field. Because the 4f electron is shielded from the ligand field by the closed 5s and 5p electron shells, the overall splitting of the 2F_j states is small, typically only a few hundred cm^{-1} . When the 4f electron is excited to the outer 5d state, however, it is subjected to the effect of the ligands. Depending upon the site symmetry, the degeneracy of the 5d state is partially or completely removed. The overall splitting of the 5d manifold is typically of the order of 5000–10 000 cm^{-1} .

Electric-dipole transitions between the 4f ground state and the 5d excited state of Ce^{3+} are parity allowed and have large oscillator strengths. Contrary to a long-lived emission of many 4f j levels of several lanthanides in glasses and crystals, corresponding to very low (10^{-6}) oscillator strengths Ce^{3+} is the only trivalent lanthanide which in the UV spectrum (Fig. 5) region shows high oscillator strength (0.01–0.1). Figure 6 shows an emission spectrum of Ce^{3+} in glass obtained by the sol-gel method [7].

3. Complexes of rare earths in sol-gel glasses

As described above, electronic transitions in trivalent rare earth ions within the f shell are forbidden by the Laporte rule and the luminescence which is dependent on the absorption of photons to the electronic levels of the same configuration is therefore weak. In addition, there is the possibility of multiphonon relaxation assisted by water or solvent vibration.

Therefore, much effort has been devoted to the study of complexes which contain ligands that have high absorbance in the UV followed by efficient energy transfer to excited f states of RE. The required structure of such complex are for instance 3,3'-biisoquinoline-2,2' dioxide (biq O₂) and biq O₂-cryptate protects also from quenching the RE ions from water vibration [8, 10].

The dominant characteristics which determines the luminescence quantum yield of these complexes are the energy gap law corresponding to the difference in energy between the excited emitting state and the highest state of the ground ^{2s+1}L term, the location and influence of ligand metal charge transfer (LMCT) states, and the competition with non-radiative decay processes. Inter- and intramolecular dynamics also affect the luminescence properties of lanthanide(III) complexes [8]. These are severely reduced in solid samples, and, more recently, in experiments in which the luminescent species have been incorporated into transparent sol-gel [8, 10].

In order to increase inertness and minimize solvent interaction, one can use a system consisting of Eu(III) ions encapsulated not only in cryptand formed by 3,3'-biisoquinoline-2,2'-dioxide and diaza-18-crown-6 groups, but also the cryptate can be entrapped in rigid and porous silica matrix. The matrix can be prepared by the sol-gel process, i.e. two reactions with tetraalkoxysilane or other precursors.

The non-radiative relaxation processes in the rare earth ions are related to their excited state population and are governed by the energy difference between the emitting level and the next lower level, separated by the number of phonons of the host [3, 4].

Silica xerogel doped with [Eu-cryptand]³⁺ was prepared by the sol-gel method from a hydrolyzed tetramethoxysilane solution containing [Eu-cryptand](CF₃SO₃)₂Br. UV-visible optical absorption spectra, fluorescence excitation and emission spectra, fluorescence lifetime as well as luminescence quantum yield were measured. Experiments were carried out in aqueous solutions and in rigid silica xerogels at room temperature. It is shown that the excitation is centred at the ligand, but the metal ion takes part in the emission process. In other words, the antenna effect was observed in the Eu(III) cryptate in the solution and xerogel. The cryptate entrapped in the xerogel showed higher emission efficiency and longer lifetime than in solution [10].

Recently, several studies have been performed on trivalent rare-earth ions doped in SiO₂ gel matrixes via the sol-gel process [11, 12]. Inorganic rare-earth salt chloride or nitrate were used. Only a weak emission can be observed from rare-earth ions doped in SiO₂ prepared at moderate temperature due to non-radiative relaxation originated from the interaction with the hydroxyl ions of water residue [11, 12]. It has been shown that organic complex of rare earth doped in SiO₂ gel had better fluorescence properties with respect to comparable inorganic salts [9, 10]. The implication of this finding is that rare-earth organic complexes doped in sol-gel hosts are good candidates for phosphors, active waveguides, optical sensors and markers of biological molecules [13].

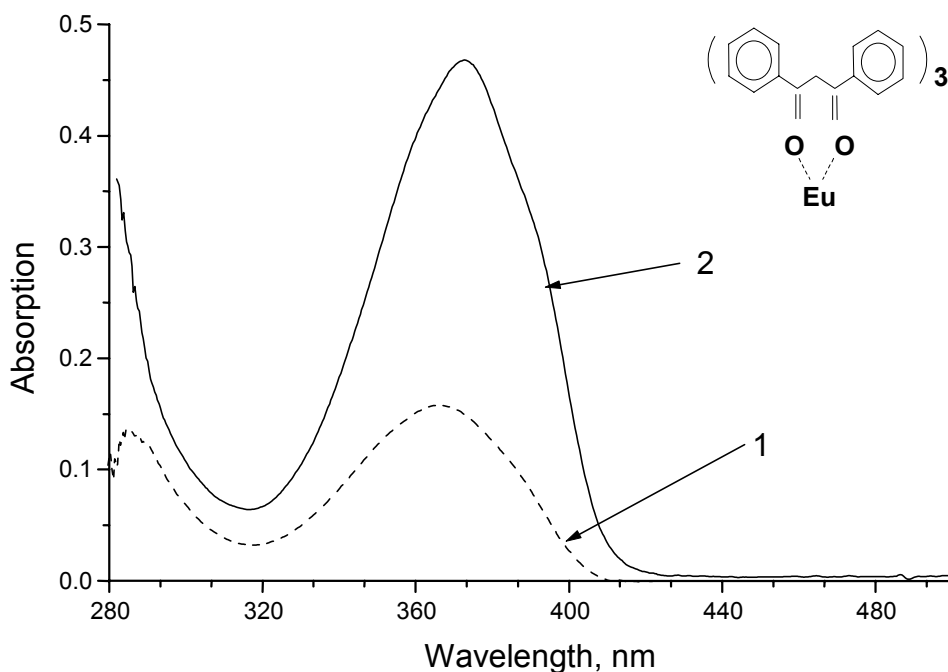


Fig. 7. Absorption spectrum of Eu(DMB)₃ complex in zirconia glass and zirconia glymo films

Zirconia glasses have some advantages over silica glasses because of their high stability and low phonon energies [14]; they were found to be excellent materials for incorporation of CdS nanoparticles [15].

Preparation of zirconia and zirconia ormosils and their physical properties have been described in details in [14].

Incorporation of RE ions into zirconia matrix allowed us to obtain better luminescence than in silica matrix [12, 15], however, this luminescence could be greatly increased when Eu^{3+} was incorporated into complexes such as dibenzoylmethane $\text{Eu}(\text{DBM})_3$ or into 3,3'-biisoquinoline-2,2'-dioxide cryptate [13].

The complex $\text{Eu}(\text{DBM})_3$ was prepared by Prof. M. Pietraszkiewicz and incorporated into films of zirconia and zirconia glymo in our laboratory. Figure 7 presents the absorption spectra and in Fig. 8 the emission spectra of the complexes are shown. When normalized to the absorption an increase of factor of five is observed in Eu^{3+} luminescence in the glymo films as compared with zirconia glass. For preparation of cryptate in zirconia films the following procedure was used [13].

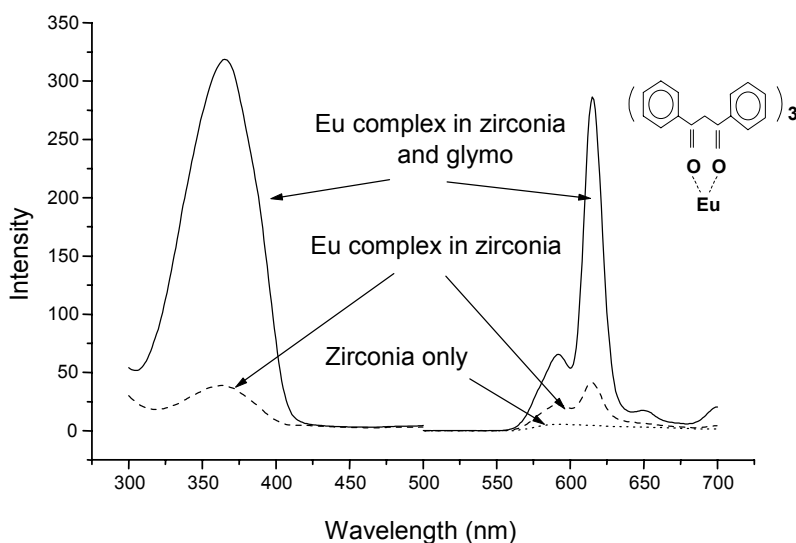


Fig. 8. Excitation and emission spectra of $\text{Eu}(\text{DBM})_3$ complex in zirconia and zirconia glymo films

Two zirconia-doped films were prepared: one with $\text{Eu}(\text{III})$ cryptate, and a hybrid material obtained by cross-condensation of zirconia tetrapropoxide and 3-glycidopropyltrimethoxysilane (abbreviated as *glymo*). The hybrid matrix incorporating silica and organic part was expected to bring two advantages: to bind water via oxirane ring opening, and to provide organic hydrophobic environment advantageous to repel the remaining water molecules from the proximity of the $\text{Eu}(\text{III})$ cryptate. The expectation was to enhance the luminescence performance. The Eu^{3+} ions were also prepared in zirconia film for comparison.

Absorption spectra of pure zirconia film and film doped with Eu_2O_3 as well as cryptate in glymo film are presented in Fig. 9. These films were transparent in the range of 350–700 nm, the zirconia-doped with Eu_2O_3 showed a broad and weak band around 350 nm. The samples with Eu cryptate show an intense band at 269 nm belonging to the charge transfer of Eu cryptate complex. It should be noted that the charge transfer of Eu oxide is positioned in the same spectral range, however, its intensity is negligible compared with the complex prepared with the same concentration of Eu.

Both Eu cryptate in zirconia and in zirconia-glymo contain a band with a maximum at 350 nm characteristic of the heterocyclic ligand absorbance. The intensity in both cases is the same within the experimental error. Therefore, there is no evident influence of glymo on electronic spectra of the cryptate unlike in $\text{Eu}(\text{DBM})_3$ complex.

In Figure 10, the excitation and emission spectra of the complex in zirconia-glymo (upper) and zirconia thin films (lower) excited at 350 nm and 269 nm is presented. The emission spectra consist of several bands at 590 nm (${}^5\text{D}_0 \rightarrow {}^7\text{F}_1$), 617 nm (${}^5\text{D}_0 \rightarrow {}^7\text{F}_2$) (the most intense), 647 nm (${}^5\text{D}_0 \rightarrow {}^7\text{F}_3$) and 684 nm (${}^5\text{D}_0 \rightarrow {}^7\text{F}_4$).

The incorporation of the cryptate complexes into zirconia films results in dramatic increase of the emission intensity as well as in the increase of the absorption intensity of Eu. The former results from the shielding of OH vibrations responsible for the non-radiative relaxation and lowering of the symmetry site in which Eu is situated. The most dramatic effect must arise from energy transfer from the organic ligand to the Eu^{3+} as depicted in Fig. 11.

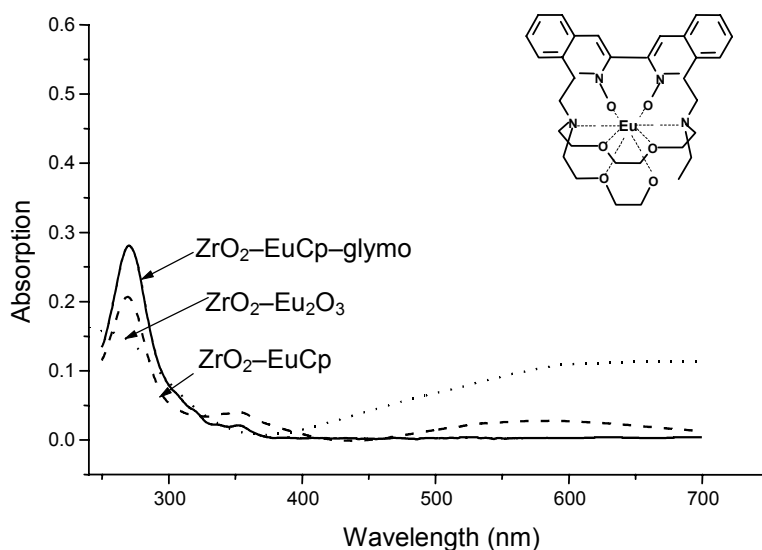


Fig. 9. Absorption spectrum of Eu^{3+} in zirconia films compared to absorption of europium cryptate in zirconia and glymo

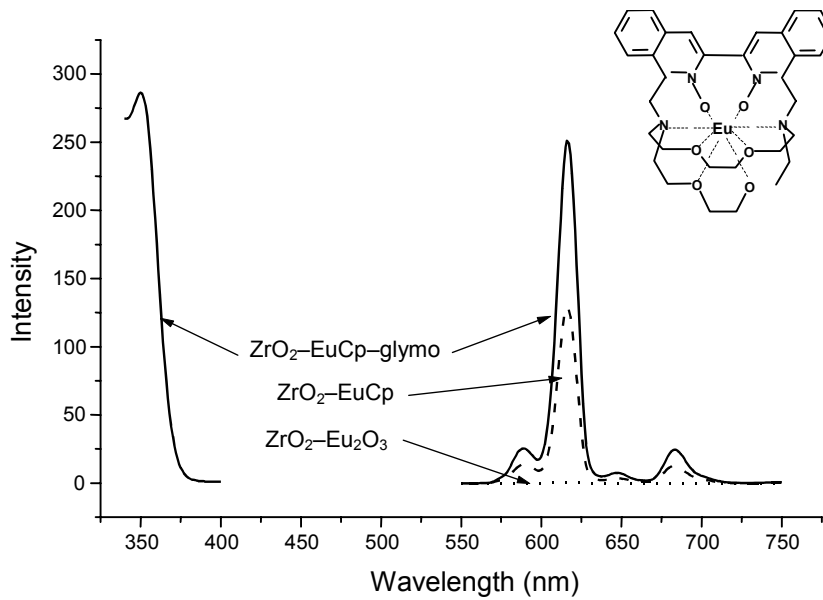


Fig. 10. Emission spectrum of Eu in ZrO_2 cryptate complex of Eu^{3+} in zirconia and the same complex in glymo

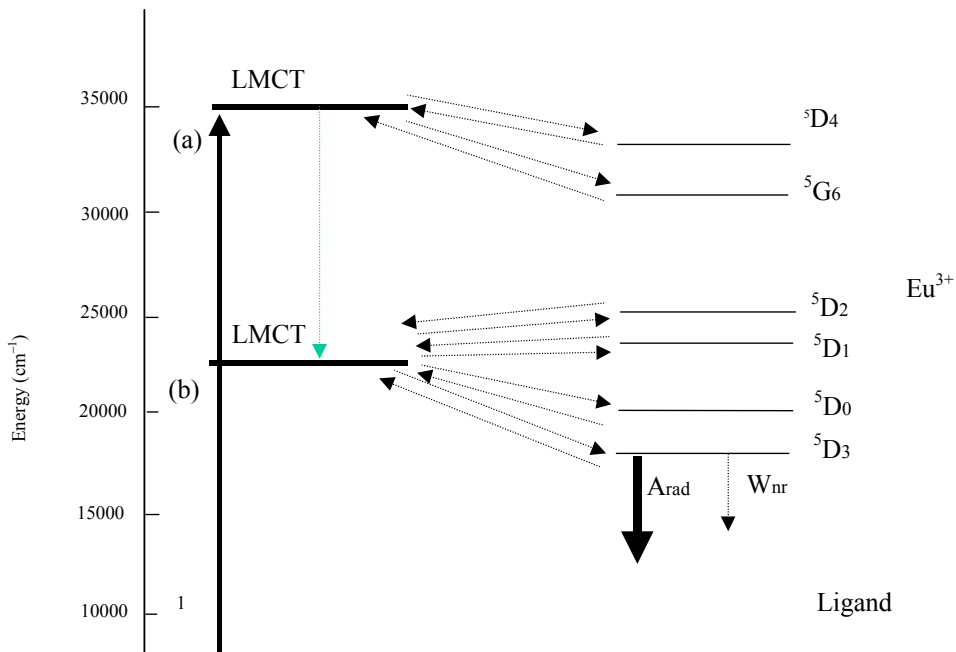


Fig. 11. Diagram of the most probable states in the energy transfer process of the Eu cryptate in sol-gel glass. The LMCT state close to the triplet (a) and the singlet (b) states of the ligand are also presented. Solid and dashed arrows describe radiative and non-radiative process, respectively

The phenomena of increase of transition probabilities are reflected by higher absorption of the complex. The energy-transfer rates between the ligands and the lanthanide ion were calculated recently in a complex of $\text{Eu}(\text{bpy}\cdot\text{bpy}\cdot\text{bpy})^{3+}$ [9].

The model took into account the molecular structure of the complex and the ligand and the location of ligand with respect to metal states. The energy transfer rate between the ligand and the lanthanide ion were obtained with the model that includes the multipolar and exchange coulombs interaction. The very elegant treatment presented there can be used in future for a general case of energy transfer between the cryptate ligand and the lanthanide ion as shown in Fig. 11.

Acknowledgement

The author is very grateful to Professor Marek Pietraszkiewicz for the very fruitful co-operation and discussions on cryptate complexes.

References

- [1] JØRGENSEN C.K., REISFELD R., *Chemistry and spectroscopy of rare earths*, [in:] *Topics in Current Chemistry*, 100 (1982), 147.
- [2] REISFELD R., *Inorg. Chim. Acta.*, 95 (1984), 69.
- [3] REISFELD R., JØRGENSEN C.K., *Excited state phenomena in vitreous materials*, [in:] K.A. Gschneidner, L. Eyring (Eds.), *Handbook on the Physics and Chemistry of Rare Earths*, 9, chapt. 58, North-Holland, Amsterdam (1987), 1.
- [4] REISFELD R., *Luminescence and nonradiative processes in porous glasses*, [in:] *Proceedings of Advanced Study Institute on Advances in Nonradiative Processes in Solids*, B. Di Bartolo and Xuesheng Chen (Eds.), Plenum, NATO ASI Series B Physics, 249 (1991), 397.
- [5] BÜNZLI J.-C.G., CHOPPIN G.R., *Lanthanide Probes in Life, Chemical and Earth Sciences: Theory and Practice*, Elsevier, 1989.
- [6] SABBATINI N., GUARDIGLI M., LEHN J.-M., *Co-ord. Chem. Rev.*, 123 (1993), 201.
- [7] REISFELD R., MINTI H., PATRA A., GANGULI D., GAFT M., *Spectrochimica Acta Part A.*, 54 (1998), 2143.
- [8] LONGO R. et.al., *Chemical Physics Letters*, 328 (2000), 67.
- [9] GAWRYSZEWSKA P.P., PIETRASZKIEWICZ M., RIEHL J.P., LEGENDZIEWICZ J., *J. Alloys and Compounds*, 300–301 (2000) 283.
- [10] CZARNOBAJ K. et al., *Spectroscopica Acta*, 54 (1998) 2183.
- [11] REISFELD R., *Structure and Bonding*, 85 (1996), 215 and references therein.
- [12] REISFELD R., ZELNER M., PATRA A., *J. of Alloys and Comp.*, 300 (2000), 147.
- [13] SARAI DAROV T., REISFELD R., PIETRASZKIEWICZ M., *Chem. Phys. Letters*, 330 (2000), 515.
- [14] SOREK Y., ZEVIN M., REISFELD R., HURVITS T., RUSCHIN S., *Chem. Mater.*, 9 (1997), 670.
- [15] ZELNER M., MINTI H., REISFELD R., COHEN H. TENNE R., *Chem. Mater.*, 9 (1997), 2541.

Received 16 June 2001
Revised 19 December 2001

Preparation and properties of colloidal nanosize silica dioxide for polishing of monocrystalline silicon wafers*

V.E. GAISHUN¹, O.I. TULENKOVA¹, I.M. MELNICHENKO¹, S.A. BARYSHNIN¹,
Y.A. POTAPENOK¹, A.P. XLEBOKAZOV¹, W. STREK²

¹AMRL, F. Skorina Gomel State University, 104 Sovetskaya St.,
Gomel, 246699, Belarus, vgaishun@gsu.unibel.by

²Institute of Low Temperature and Structure Research, Polish Academy of Sciences,
2 Okólna St., 50-950 Wrocław, Poland

Colloidal silica can be used for final general metallographic polishing. It is used to polish silicon single crystals for electronic applications and, subsequently, polycrystalline silicon for solar cells, gallium arsenide, indium phosphide, titanium, gadolinium, gallium garnet and sapphire. The silica dioxide is dispersed in water with alkaline compound added to obtain the desired pH.

Key words: *colloidal silica, metallographic polishing, silicon*

1. Introduction

Colloidal silica [1–3] can be used to polish most metals, alloys, minerals, ceramics and composites. It can also be used after one or two diamond polishing steps or after using alumina slurry. Colloidal silica, also referred to as a sol, contains very fine particles (1–300 nm in diameter) that remain in suspension over a long period of time (several years). In colloidal silica, the particles are amorphous rather than crystalline, and they have a negative electrical charge. The particles are nearly insoluble in the dispersing medium (distilled water). pH is the main factor influencing the stability of colloidal silica and, in addition, pH is the electrochemical factor, which plays a significant role in polishing semiconducting material slices.

The aim of the present work is to prepare colloidal nanosize silica dioxide used for final polishing of silicon wafers and to investigate their physicochemical properties.

*The paper presented at the International Conference on Sol-Gel Materials, SGM 2001, Rokosowo, Poland.

2. Experimental

Following chemical agents were used for synthesis of colloidal silica [3]: powder of silica dioxide or silica gel, potassium hydroxide (KOH) and distilled water. The preparation technique of colloidal silica sol consists of the following stages: mixing initial components, centrifuging the mixture obtained and control of parameters. Stable sol is centrifuged in order to remove large particles of silica dioxide and technological impurities, which can have negative effect on the process of polishing the silicon wafers. Centrifuge of the OC-6M type was used for purification at 2000–2500 rpms during a 15 minute time interval. Control of pH of the synthesized sols was carried out in the laboratory by pH-meter – millivoltmeter pH-121. Areometers were used to determine the density of colloidal silica. Rotary viscosimeter (PEOTECH RV 2.1) was used to determine the viscosity of suspension. Observation of the shapes of the silica particles was conducted by examining the samples with scanning electron microscopy (SEM, JSM-50 A (JEOL, Japan)).

3. Results and discussion

Amorphous silica particles in the colloidal silica dispersions are in closed spherical shape. Figure 1 shows a SEM view of amorphous silica particles in sol. The differences in particle sizes, as it is visible in Fig. 1, are 300 nm and less.

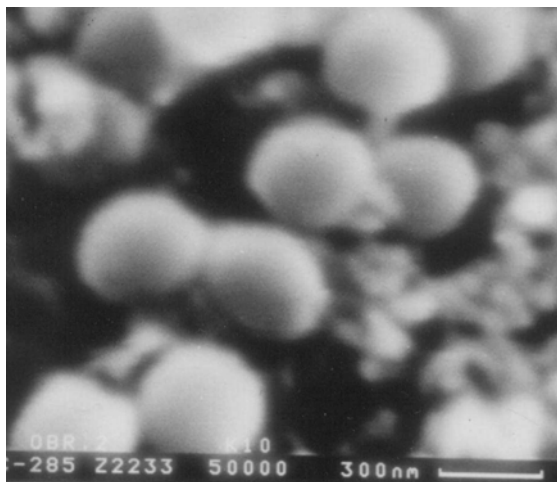


Fig. 1. SEM picture of colloidal silica dioxide

The hydroxide of potassium and silica particles were added to water, so that the pH of the synthesized colloidal silica was at least 10.5–11.0. Dependence of the colloidal silica dioxide sedimentation stability on pH is described in [4] and is shown in Fig. 2.

The colloidal silica dioxide flocculates between pH 4 and pH 8, approximately at pH = 6. In our case, the particles of silica sols did not flocculate. Negative charge accumulated on the surface of the colloidal silica particles in the basic conditions and the particles were repulsed from each other.

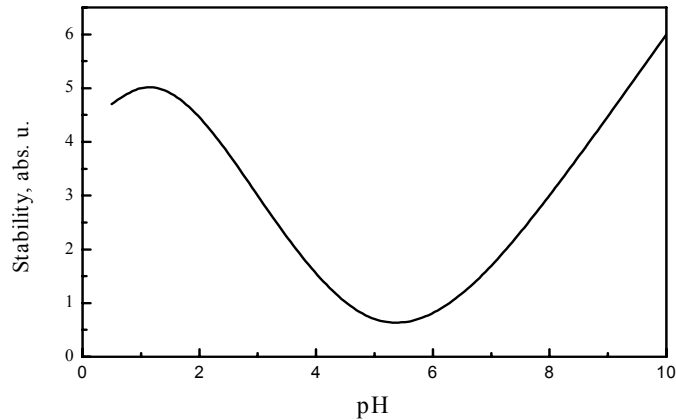


Fig. 2. Effect of pH on sedimentation stability of colloidal silica

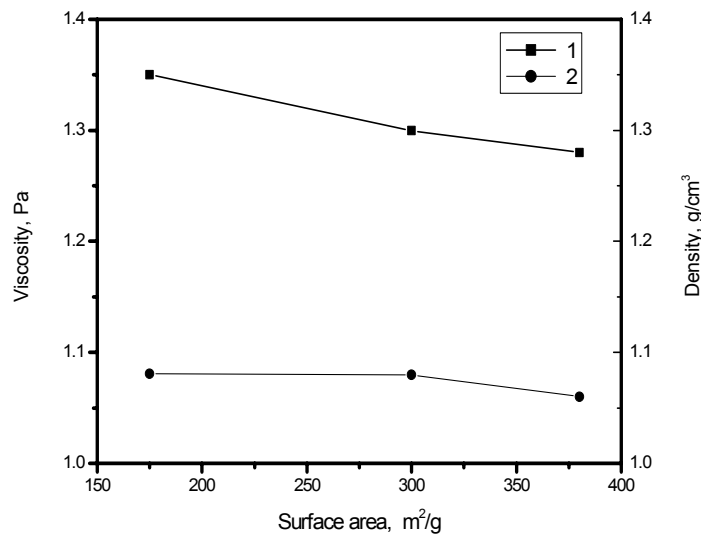


Fig. 3. Relation of viscosity and density of colloidal silica sol to specific surface area of particles silica dioxide: 1 – viscosity of silica sols, 2 – density of colloidal silica

Even though the maximum sedimentation stability is reached at basic values of pH, the stability begins to decrease when the pH level exceeds 11. Temperature also influences the sedimentation stability of colloidal silica dioxide. The colloidal silica

dioxide congeals at the temperature below 6 °C. If the suspension is frozen, it becomes less dense in the upper layer of a vessel and more dense at the bottom. The dependence of the viscosity of the suspensions obtained on the specific surface of the particles is shown in Fig. 3.

Density and viscosity of the colloidal silica dioxide particles decrease with the increase of the specific surface of the SiO₂ particles. Thus, the viscosity of synthesized suspensions increases with reduction of the specific surface of the silica dioxide particles and the increase in their size. It has been established that centrifugation of the identical quantity of silica oxide dispersed in water (a suspension with higher specific surface of the particles) leads to precipitation of the large part of the silica dioxide.

4. Conclusion

Amorphous silica particles in the colloidal silica dispersions are nearly spherical in shape. The density and viscosity of the colloidal silica dioxide obtained decreases with the increasing specific surface of SiO₂ particles. The hydroxide of potassium is added to colloidal silica, so that pH of the synthesized sols is at least 10.5–11.0.

The synthesized colloidal nanosize silica dioxide can be used for final polishing of silicon wafers.

References

- [1] PAYNE C.C., U.S. Patent 4, 169,337, *Process for Polishing Semi-Conductor Materials*, October 2, 1979.
- [2] YANCEY P.G., U.S. Patent 4, 242, 842, *Precision Polishing Suspension and Method for Making Same*, January 6, 1981.
- [3] PAYNE C.C., U.S. Patent 4, 558, 421, *Aqueous Silica Compositions for Polishing Silicon Wafers, Silica Gel or Sol and Piperazine Compound*, May 13, 1986.
- [4] ILER R.K., *The chemistry of silica*, Moscow, "Mir", p. II, 1982, p. 135.

Received 16 June 2001
Revised 19 December 2001

Humidity dependencies of porous sol-gel and silica glass linear sizes*

S.A. GEVELUYK¹, I.K. DOYCHO¹, L.P. PROKOPOVICH¹,
E. RYSIAKIEWICZ-PASEK², E.D. SAFRONSKY¹

¹Odessa National Mechnikov University, Dvoryanska St. 2, 65026 Odessa, Ukraine

²Institute of Physics, Wrocław University of Technology,
Wybrzeże Wyspiańskiego 27, 50-370 Wrocław, Poland

Measurements of the porous sol-gel and porous silica glass linear size dependencies on humidity of the surrounding atmosphere were performed using the interferometric techniques. The secondary silica gel existing in the voids of silica porous glasses is absent in the sol-gel glasses. The pore size distributions have two peaks for the sol-gel glass while there are several peaks with decreasing amplitudes in the silica porous glass. The differences in the linear sizes moisture sensitivity are explained by the structure of both types of porous materials. The capillary effects prevail in the last ones. The revealed peculiarities of sol-gel glasses make it possible to develop threshold humidity sensors of a new type.

Key words: *porous glasses, adsorption, desorption, humidity sensor*

1. Introduction

Porous sol-gel glasses are promising materials for a broad spectrum of possible applications in electronics, sensor techniques, pharmacology, prosthetic appliances, etc. The structure and chemical composition of porous sol-gel glasses are close to silica porous glasses [1]. This allows us to investigate them by the techniques developed for silica porous glasses [1–4]. One of these techniques is the carbon treatment. It is based on thermal annealing (450–600 °C) of the porous material with carbon preliminary impregnated into the pores [1, 3]. Reduction of silicon occurs inside the voids due to different chemical activity of both elements and silicon clusters are created in the silica porous glass. These clusters make their contribution to luminescence. The position of spectral maximum is related to the average size of the clusters. These sizes depend,

*The paper presented at the International Conference on Sol-Gel Materials, SGM 2001, Rokosowo, Poland.

first of all, on the sizes of voids in the starting material. Thus, a certain correlation exists between the pore-size distribution and the photoluminescence spectra. Comparison of photoluminescence spectra for silica porous glasses and sol-gel glasses shows that they are practically indistinguishable before carbon treatment [1]. At the same time the positions of light emission peaks differ after this treatment. In the present work, the ambience humidity dependencies of the linear size relative change are compared for porous silica glasses and porous sol-gel glasses.

2. Experimental section

Porous silica glasses were obtained from two-phase alkali borosilicate glasses by alkali borate phase chemical etching. The corresponding technique is discussed in references [5–7]. Porous sol-gel glasses were obtained as described previously [1] from tetraethoxysilane water solution with the ratio of 1 to 4 molar percent. Hydrochloric acid (HCl) with concentration approximately in the range from 30 up to 70% was used as a catalyst in this process. The mixture was stirred at room temperature for about an hour and then was polymerized in polyethylene containers for 100 hours. The obtained samples were dried up in a chamber where the temperature was slowly increased to 600 °C. Both types of the investigated glasses had initial sizes of $10 \times 15 \times 0.5$ mm³.

The humidity dependence of the linear sizes was investigated using the set up based on the Michelson interferometer. One of the interferometer shoulder mirrors was in direct contact with the sample placed in a special gas chamber. The mixture of dry and wet air passed through it. Using the special regulated gas valve system, the humidity of the atmosphere in the chamber could be changed in the range from 10 to 90%. In order to maintain high accuracy of the measurements, the minimal possible rate of gas flow was maintained and the temperature was kept constant. Each subsequent change of humidity was made after complete stabilization of the sample parameters. These parameters were controlled by the position of the fringe pattern movement with respect to the photodiode slot. The 632.8 nm He-Ne laser was used as a light source. The accuracy of 0.001% was achieved in the interferometric measurements of the standard samples with the length of 15 mm. The pore size distribution spectra were obtained by the capacitance method using water vapour absorption-desorption [8, 9].

3. Results and discussion

Figure 1 shows pore size distribution spectra for both porous sol-gel and porous silica glasses. It is necessary to mention that both spectra have similar shape but the distribution is rather mono-disperse (only two fractions) in the first spectrum, while in the second one, case there is a set of peaks with fading amplitude. The number of

pores with larger sizes increases. The amount of fractions depends on the properties of the initial glass and on the etching conditions. In the range of pore radii from 0 up to 60 nm four fractions are clearly seen in Fig. 1. However, there were only two peaks in the samples studied in our previous paper [4]. Nevertheless, the void sizes corresponding to these fractions were always larger than in the case of sol-gel glasses.

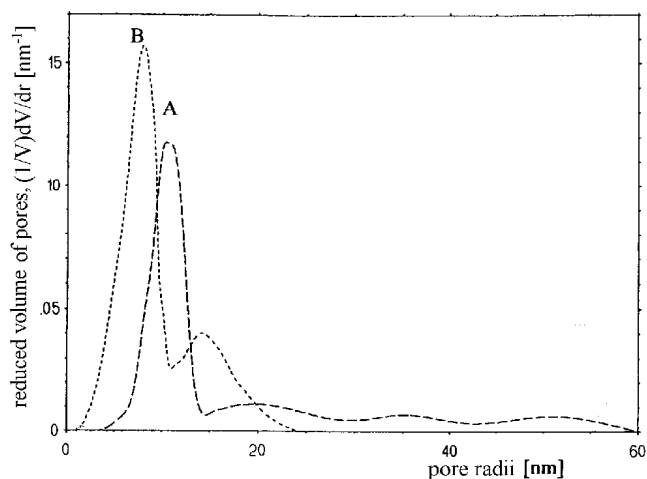


Fig. 1. Size distribution of pores for the silica porous glass (A) and the sol-gel glasses (B)

Microporosity (the average pore size about 2 nm [10]) and almost complete absence of chemical pollution are typical of sol-gel glasses. This is due to the mechanism of their fabrication [11]. The silica porous glasses chosen for comparison with sol-gel specimens were also microporous and the residual silica gel, which was located on the internal pore surface, was almost completely removed by additional chemical treatment in KOH. It is known [6] that certain dissolution of the main framework of silica glass happens as a result of such treatment besides of the secondary silica gel removal. The average pore radius has increased after corresponding over-etch of the pore walls. We want to stress that the traces of secondary silica gel remain after the chemical treatment (as shown in Ref. [4]). Manufacturing of porous glass by the sol-gel technologies gives an opportunity to adjust the pore size and simultaneously excludes the availability of such formation. This explains, in our opinion, different dependencies of linear sizes on humidity for both materials, as shown in Figs. 2 and 3.

The monotonous character of the humidity dependence of the linear sizes for porous silica glass (presented in Fig. 2) in the whole humidity range corresponds to the dominance of the stretching forces connected to swelling of the residual silica gel over the capillary forces of compression. In the case of sol-gel glasses, the character of specified dependencies is essentially different (Fig. 3). Absence of pronounced changes in the specimen size due to in the humidity range from 10% up to 70% suggests that there is no appreciable modification of the pore surface in this range. An abrupt compression of the sample (reaching maximum at 80% humidity) can be ex-

plained by the formation of water menisci in the necks of pores with minimum sizes. When humidity is further increased, small voids are filled with water and the moisture begins to be condensed on walls of the pores with greater sizes. It results in almost complete disappearance of the capillary forces (the menisci in these pores is not formed yet) and the size of the sample returns to its initial value. In the case of larger values of humidity the water menisci are created in the fraction of voids with large dimensions (fraction of the diameter 15–17 nm in Fig. 1). The decrease of the sample length in this case is much smaller. This is due to, first, the large radius of the meniscus and, second, the smaller number of corresponding pores. After all the pores are filled with water, the sample length again returns to its initial value.

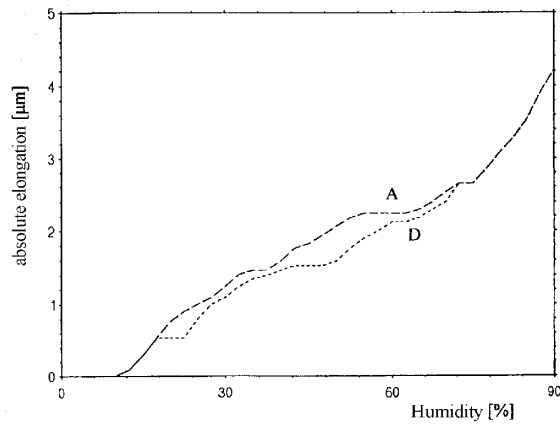


Fig. 2. Dependence of the linear sizes of porous glass during adsorption (A) and desorption (D) on humidity

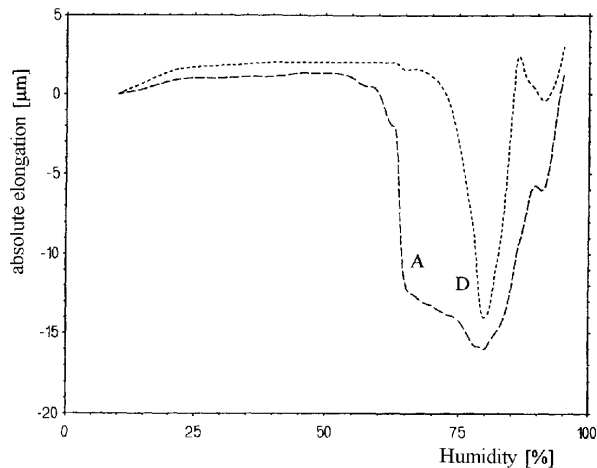


Fig. 3. Dependence of the linear sizes of porous sol-gel glass during adsorption (A) and desorption (D) on humidity

Let us also note that the humidity dependence of the linear size change is more pronounced for the sol-gel glasses in comparison with the similar dependence for the silica porous glasses. We argue that this fact is due to the influence of capillary compression forces only, while no substance similar to the secondary silica gel exists inside the sol-gel glass. No etching was employed in the fabrication process of these glasses and pore formation is the consequence of the glomerular macromolecule structure.

We want to emphasize that the ranges of practical insensitivity to environment humidity for porous sol-gel glasses depend on the pore size distribution. Insensitivity range is wide enough (in Fig. 3 it is about 70%). Adjustment of the specified distribution is possible during the fabrication of porous sol-gel glasses [11]. Thus, it appears possible to create threshold humidity sensors that switch at given humidity and may be used, for example, at the agricultural enterprises and in food industry.

4. Conclusion

Comparison of humidity dependencies of the linear sizes for silica porous glasses and sol-gel glasses has shown that in the latter case the dependence is more pronounced. At the same time there are wide enough areas of insensitivity to humidity. The specified distinctions can be explained by different mechanism of pore formation in both materials. This results in the trade off between residual silica gel swelling (stretching forces) and capillary effects (compressive forces). Besides it, a lot of dangling bonds are created during etching at the internal surface of silica porous glasses that further act as absorption centers for water. The pore surface in sol-gel glasses is more chemically steady. It is possible to regulate the sensitivity threshold in sol-gel glasses and thus to fabricate sensors that switch at given humidity.

References

- [1] SAVIN D.P., GEVELYUK S.A., ROIZIN YA.O. et al., *Applied Physics Letters*, 72 (1998), 3005.
- [2] ROIZIN YA.O., ALEXEEV-POPOV A.V., GEVELYUK S.A. et al., *J. Phys. Chem. Glasses*, 11 (1996), 68.
- [3] GEVELYUK S.A., DOYCHO I.K., KOVALENKO M.P. ET AL., *Optica Applicata*, 30 (2000), 635.
- [4] GEVELYUK S.A., DOYCHO I.K., RYSIAKIEWICZ-PASEK E. et al., *J. Porous Materials*, 7 (2000), 467.
- [5] JANOWSKI F., HEYER W., *Porose Glaser*, VEB Deutscher Verlag fur Grundstoffindustrie, Leipzig 1981.
- [6] MAZURIN O.V., ROSKOVA G.P., AVJER'JANOV V.I. et al., *Bi-phase Glasses: Structure, Properties and Application* (in Russian), Nauka, Leningrad 1991, p. 276.
- [7] RYSIAKIEWICZ-PASEK E., ŁUKASZEWSKI P., BOGDAŃSKA J., *Optica Applicata*, 30 (2000), 173.
- [8] SAFRONSKY E.D., ROIZIN YA.O., RYSIAKIEWICZ-PASEK E., *Optical Materials*, 5 (1996), 217.
- [9] GREG S.J., SING K.S., *Adsorption, Surface Area and Porosity*, Academic Press, London 1982.
- [10] SODOLSKI H., KOZŁOWSKI M., *Polish Ceramic Bulletin*, 19 (1998), 73.
- [11] BRINKER C.J., SCHERER G.W., *Sol-Gel Science: The Physics and Chemistry of Sol-Gel Processing*, Academic Press, San Diego 1990.

Received 16 June 2001
Revised 17 December 2001

Incorporation of copper and its oxides and chalcogenides into silica sol-gel materials *

V.S. GURIN¹, A.A. ALEXEENKO², V.B. PRAKAPENKA³,
D.L. KOVALENKO⁴, K.V. YUMASHEV⁵, P.V. PROKOSHIN⁵

¹Physico-Chemical Research Institute, Belarusian State University, Leningradskaja str., 14, Minsk, Belarus, gurin@bsu.by, gurinvs@lycos.com

²Gomel State Technical University, October Ave. 48, Gomel, 246746, Belarus
Alexeenko@gsu.unibel.by

³CARS, University of Chicago, Argonne National Lab., APS, 9700 S. Cass Ave, Argonne, IL 60439, USA, prakapenka@cars.uchicago.edu

⁴Advanced Materials Research Laboratory, Gomel State University, Gomel, Belarus

⁵International Laser Centre, BSPA, Minsk, Belarus

Recent results concerning fabrication and optical features of the sol-gel materials are reviewed. The nanoparticles of copper, copper oxides, sulfides and selenides have been produced by means of the modified silica-based sol-gel technique within two types of materials: amorphous silica films and monolithic glasses. Features of the optical absorption are discussed in dependence on the chemical composition. Optical properties are varied with element composition of the compounds, size of particles, their concentration, etc. The quantum confinement and partial surface chemical modification of the nanoparticles are considered as possible reasons for appearance of optical features of the copper multivalent compounds.

Key words: *sol-gel films, glasses, nanoparticles, copper, copper oxide, copper sulfide, copper selenide*

1. Introduction

Glassy materials doped with transition metal ions, nanoparticles and clusters of different chemical composition including oxides, sulfides and selenides have been found to be of great scientific and practical interest [1, 2]. Optical materials fabricated from doped glasses and films are widely used in optics and optoelectronics as selective filters, passive laser elements, optoelectronic switches, etc. Silica matrices provide stable samples for study of novel physical phenomena associated with low-dimensional em-

*The paper presented at the International Conference on Sol-Gel Materials, SGM 2001, Rokosowo, Poland.

bedded objects (excitation and relaxation of rare earth ions [3] and quantum-confined semiconductors [4], surface plasmon resonance in metals [5], light-induced transformations in nanoparticles [6], etc.).

Historically, the main method of doped glass fabrication consisted of melting components (oxides, fluorides or another glass-forming base) with the addition of dopants which underwent some chemical transformation resulting in final products responsible for their optical properties. Also, there is a number of preparation methods for glassy films that can be distinguished by the starting phase state of components – direct evaporation-deposition, chemical vapour deposition or reactive sputtering with participation of gaseous reactions and deposition from liquid solutions with dipping or spin-coating. The last method is similar to the familiar sol-gel technique [7–9], the main idea of which is the realization of complete sequence “sol → gel → solid” selecting chemical composition of precursors allowing these phase transformations. Organic derivatives of silicon, titanium and other polyvalent elements favour well this idea due to easy hydrolysis and polycondensation processes to form oxide structures. Doping in this case can be done at different stages. The sol-gel technique is successfully applicable also to fabrication of monolithic glasses. However, detailed methods of doping can be slightly different as compared with those for the films.

In this paper, we consider from one viewpoint the two types of sol-gel derived materials: thin films and monolithic glasses. The preparation technique was developed specially for doping with copper compounds dispersed as nanoparticles within the stiff silica matrix. The known advantages of the sol-gel-based methods are the lower temperature of final heat treatment (comparing with fused technique), flexibility in composition and intermediate chemical treatments favour the complex composition of the materials. Similar materials with transition metal compounds cannot be prepared with conventional molten glass technology. Liquid state of the precursor sols provides the best condition for homogeneity, and subsequent gaseous phase reactions retain also this aspect. At the same time new effects appear for some sample compositions, (as surface segregation [10]) that can also be used for preparation of special materials.

2. Samples preparation and characterization

The first fabrication step of *bulk monoliths* (Fig. 1) is conventional for the sol-gel technique and consists of preparation of precursor sol by mixing alcohol-aqueous solution of tetraethoxysilane (TEOS) at the molar ratio $\text{TEOS}/\text{H}_2\text{O} = 1/8$. Different acid catalysts – HCl , HNO_3 , H_2SO_4 (with molar ratio $\text{acid}/\text{TEOS} = 1/50$) were studied to promote hydrolysis of TEOS. Aerosil (SiO_2 powder with the grain size on the order of 20 nm and surface area 150–400 m^2/g) was added to sol before gelation to avoid strong volume contraction under drying. A part of agglomerated aerosol was separated

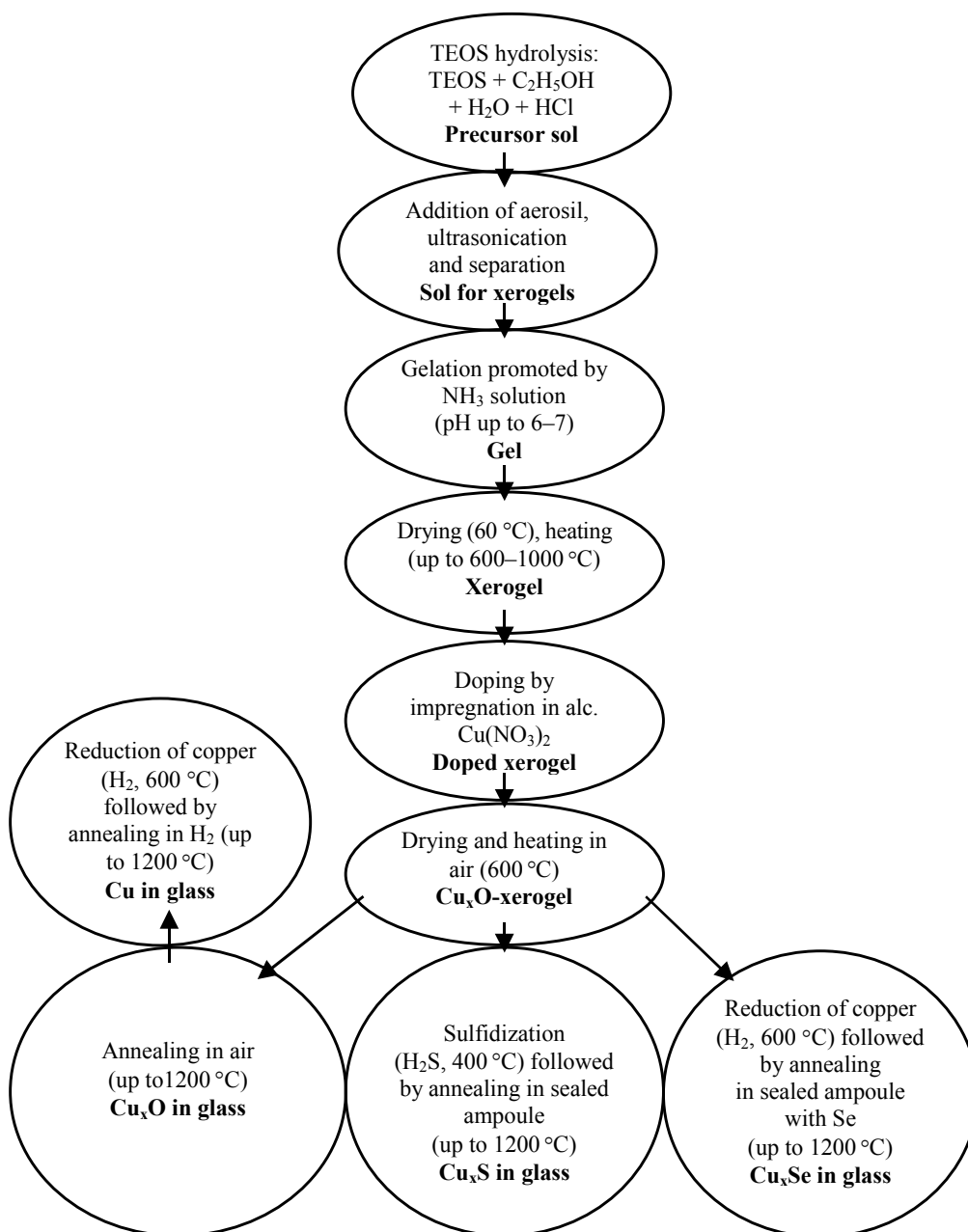


Fig. 1. Fabrication scheme of the silica sol-gel glasses

by centrifugation. Such sols had density of 1.05 g/cm^3 and could be stored at $3\text{--}5^\circ\text{C}$ without spontaneous gelation for 15–20 days. The gelation occurred when pH was increased up to 6–7 with addition of ammonia solution. In order to fabricate mono-

lithic glasses of definite shape, the sols were poured into polystyrene containers, and gelation proceeded for 24 h. The gels were dried at 60 °C and heat-treated up to 600–1000 °C for 2 h to remove sorbed water and organic remnants of TEOS. The temperature regime influences the properties of xerogels (porosity, amount of remnant hydroxyl groups, etc.) and was used as one of the experimentally controllable factors influencing final materials features. Such products, as *xerogels* resulted in finally annealed pure silica glassy monoliths heated treatment up to 1200 °C in the air. The doping was carried out via two routes: (1) mixing of metal salts ($\text{Cu}(\text{NO}_3)_2$) with precursor sols, (2) impregnation of porous xerogels (before the high-temperature annealing step) in alcoholic $\text{Cu}(\text{NO}_3)_2$ solutions for 8 h.

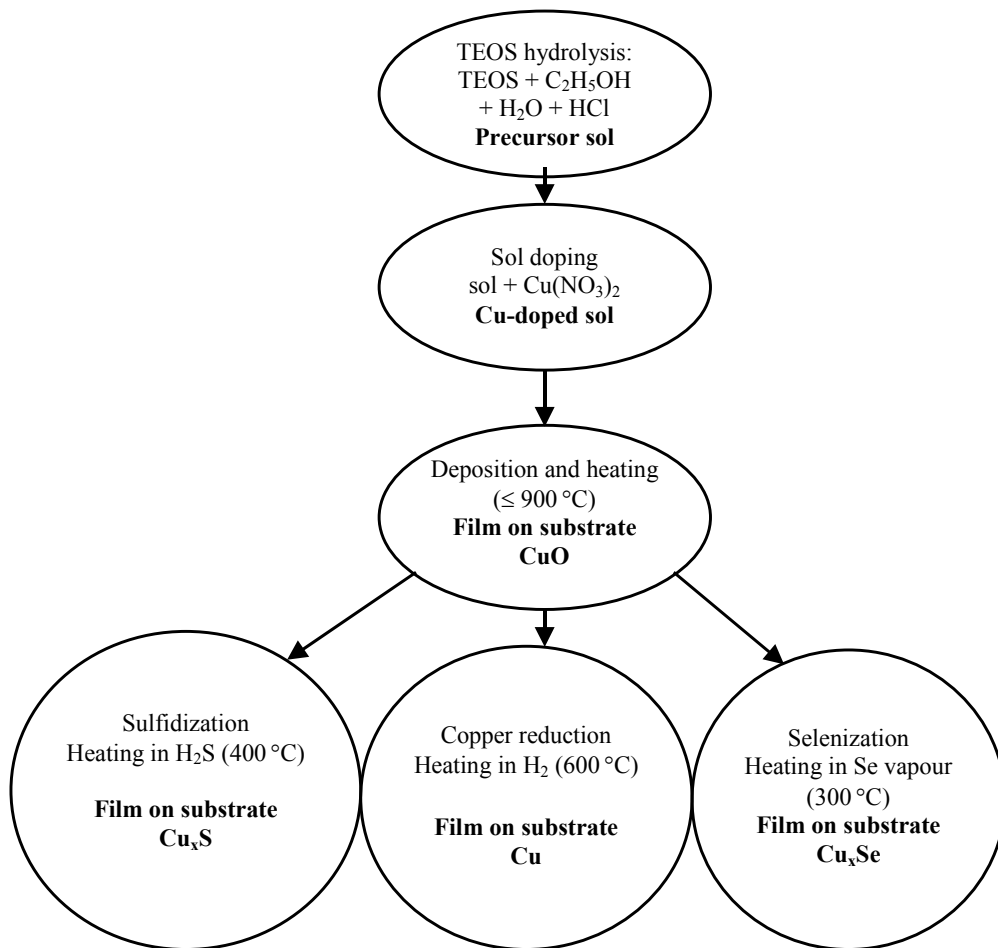


Fig. 2. Fabrication scheme of the silica sol-gel films

Subsequent chemical transformations of copper compounds introduced by doping were performed via different routes leading to formation of nanoparticles of metal, oxide, sulfide or selenide (Fig. 1): (1) heating and annealing of the doped xerogels (~ 1200 °C) in H_2 , (2) heating and annealing of the xerogels (~ 1200 °C) in the air, (3) heating in the air followed by H_2S (400 °C) and annealing in a closed quartz ampoule up to 1200 °C, (4) heating in H_2 (600 °C) followed by annealing in Se vapour in a closed quartz ampoule up to 1200 °C. This final annealing step resulted in production of transparent glassy samples (*monoliths*) of high optical quality and good mechanical strength.

The fabrication of doped silica *films* (Fig. 2) proceeded with the simpler sequence without the high-temperature annealing. The homogeneous sol-gel films were formed by spin-coating process on polished silica substrates. The doped sols were prepared by dissolving copper nitrate in sols yielding partially hydrolysed copper nitrate, $Cu_2NO_3(OH)_3$, characterized directly by XRD analysis [11]. The following four different types of processing for the films were developed: (1) heating in hydrogen (600 °C, 1 h) resulted in reduction of copper up to the metallic state, (2) heating in the air up to 900 °C (this temperature retained amorphous character of the silica matrix) to produce the films doped with copper oxide, (3) heating in the air (900 °C) with subsequent treatment in H_2S atmosphere (400 °C, 1 h) to obtain copper sulfide nanoparticles embedded into the silica matrix, (4) similar heating in the air (900 °C) and subsequent processing in H_2 (600 °C, 1 h) followed by heating in selenium vapour (300 °C, 1 h). The last step resulted in formation of copper selenide nanoparticles dispersed in silica matrix. The thickness of films was in the range of 300–1000 nm and controlled by amount of spin-coated sols deposited on substrates under constant rotation speed (2000–5000 min^{-1}).

The above-described different preparation sequences were designed to form nanoparticles including a series of copper compounds (Cu_xO , Cu_xS , and Cu_xSe) or metallic copper. However, production of a broader range of other compounds is also possible. The chemical composition of the above series of compounds with the variable stoichiometry both in the case of films and monolithic glasses has been established using several methods: XRD (mainly for films) [11–13], XPS (also for films [13] and some glasses with higher concentration of dopants), RBS (both for films and glasses) [14, 15]. Transmission electron microscopy (TEM) studies have revealed that the materials are nanoparticles (in the range of 10–100 nm) embedded into amorphous glassy matrix [14]. The size of nanoparticles depends on the concentration of the dopants and particulars of the heat treatment of xerogels. Nanoparticles in the monoliths have usually relatively low concentrations (from 10^{12} – 10^{13} cm^{-3}), and the aggregation degree of them is not large, so in the most cases they may be considered as separate ones surrounded by glassy matrix rather than in contact with other particles. The concentration of particles in the films was 2–3 orders of magnitude larger (due to the more relative amounts of dopants), possessing the sizes similar to those observed for the monolithic glasses.

3. Optical properties

Optical absorption spectra of the sol-gel silica films and glasses doped with different copper compounds are summarized in Fig. 3. In spite of their similar general chemical composition, their optical properties reveal remarkable differences. The optical properties depend on particulars of the preparation, the particles concentrations and features of the matrices.

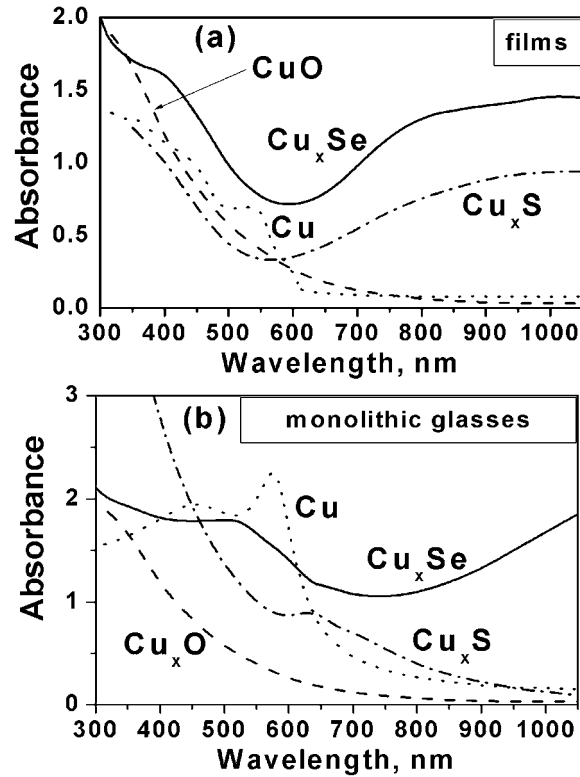


Fig. 3. Absorption spectra of the sol-gel silica films (a) and glasses (b) containing nanoparticles of different copper compounds indicated by their chemical formulas

The spectra of Cu_xO-doped films are similar to those of monolithic glasses and show the sloping monotonous spectrum with a very weakly developed shoulder in the short-wavelength range ($\lambda < 350$ nm). Such spectra are characteristic of indirect-gap semiconductors and are consistent with properties of CuO or Cu₂O. Size effects are virtually absent. According to the XRD data [11], in such films the chemical form of CuO is dominating. Recent photoluminescence results [16] suggest that Cu⁺ ions in Cu₂O nanoparticles occur in glasses. This difference in composition of films and

glasses can be caused by differences in concentration of the dopants (much higher for films than monoliths) and higher maximum temperature of heating during the preparation (900 and 1200 °C, respectively). The higher temperature, evidently, can lead to decomposition of Cu(II) oxide ($4\text{CuO} \rightarrow 2\text{Cu}_2\text{O} + \text{O}_2$).

A reductive heat treatment in hydrogen is known to lead to easy transformation of copper oxides to metallic copper ($\text{Cu}_x\text{O} + \text{H}_2 \rightarrow x\text{Cu} + \text{H}_2\text{O}$). However, the size and concentration of particles affecting the optical response can be different for films and glasses due to variations in matrix properties and initial chemical compositions. Usually, absorption features of small copper particles are described well (at least, in the first approximation) using the Mie theory explaining maxima in absorption spectra as a combination of a λ -dependent dielectric function ($\varepsilon_2(\lambda, R) \sim R^{-2}$) occurring in the total expression $\varepsilon = \varepsilon_1 + i\varepsilon_2$ [17] and medium dielectric constant ε_0 . The typical spectra of copper nanoparticles possess main maxima in the range of 500–600 nm (properly, the plasmon resonance from the Mie theory) and additional features originate from the complicated $\varepsilon(\lambda)$ dependence on the band structure of metallic copper. The more pronounced maxima observed for copper nanoparticles in glasses, as compared to the films, as well as a small (several tens of nanometers) blue shift of the band position can be the consequence of a more homogeneous size distribution of the particles in the glasses with much lower concentrations and particle–particle interactions.

It should be emphasized that we have shown only some selected representative spectra of the copper nanoparticles: they vary with changing properties of the xerogels and dopant concentrations retaining similar general principal appearance with the plasmon resonance maximum in the range of 500–700 nm. This feature can be used for designing of cut-off filters. Production of copper chalcogenides (sulfides and selenides) nanoparticles embedded in the sol-gel films and glasses is the principal purpose of the preparative part of this work; oxides and metallic particles appear mainly as intermediate steps of the reaction sequence. Chalcogenides of different metals are the subject of studies of the size effects through observation of certain non-trivial optical features [18]. Copper sulfide particles have been produced within fused glasses [19, 20], and ultrathin nanostructured films have been fabricated by means of the Langmuir–Blodgett technique [21, 22]. The sol-gel technology allows studies of both copper sulfide and selenide within matrices of similar composition. The typical absorption spectra of films with the chalcogenides (Fig. 3a) reveal the two principal features: (i) the fundamental absorption band and (ii) the intense and rather broad (in particular with the λ -dependence presentation) absorption peak in the near IR range. They both are composition-dependent. However, their positions may be associated to the corresponding ranges of E_g (both direct and indirect): 1.2–2.2 eV [23] including the possible blue shift. This shift is observable only for copper compounds and has been interpreted recently by us [24–26] as midband levels due to the partial change of the copper valence state (accompanied also by partial or surface oxidation of nanoparticles).

In the case of monolithic glasses, the behaviour of sulfide and selenide nanoparticles is different (Fig. 3b), and the IR-band is observable only in the selenide case. It can be assumed that the main reason of this difference is variation of stoichiometry of nanoparticles. The composition of Cu_xS nanoparticles is close to CuS , however Cu_xSe is a very variable compound retaining the similar features of the absorption spectra. The monolithic glasses with Cu_xS were not analysed directly in order to establish for the chemical composition, however, the spectrum is consistent with that given in [19, 20] for Cu_2S nanoparticles. Thus, as well as in the case of oxide nanoparticles, the conditions of preparation of monolithic glasses favour the lowest valence state of copper, Cu(I) . Copper selenides are produced with a substantial excess of selenium (partial Se pressure of about 1 atm sufficient due to the small size of samples in ampoules). To control composition of the selenides, we used porosity of xerogels with the same overall selenium amount. In the case of sulfides there was no possibility to control the sulfur amount because of the higher volatility of sulfur, instead, copper sulfide (CuS , dominantly) was pre-produced within porous xerogels prior to the annealing step without providing any additional source of sulfur. Under these conditions CuS decomposes during subsequent heat treatment up to $1200\text{ }^\circ\text{C}$. Cu_xSe phases are formed according to the Cu-Se phase diagram [27, 28].

4. Conclusions

Two types of nanostructured sol-gel derived optical materials: silica thin films on solid substrates and monolithic silica glasses containing copper, copper oxide and chalcogenide nanoparticles have been developed. Absorption spectra reveal various features of nanoparticles of Cu , Cu_xO , Cu_xS , and Cu_xSe . The exact chemical composition of those nanoparticles depends on the type of material, details of the preparation procedure and can be controlled within certain experimental limits.

Acknowledgements

The authors express their thanks to Drs. K.N. Kasparov, E.A. Tyavlovskaya, L.V. Sudnik, E.N. Poddenezhnyi, A.A. Boiko and Prof. I.M.Melnichenko for fruitful discussion and encouragement. The work was partially supported by the Ministry of Education of Belarus and the Fundamental Research Foundation of Belarus.

References

- [1] GAPONENKO S.V., *Optical properties of semiconductor nanocrystal*, Cambridge Univ. Press, Cambridge, 1998.
- [2] BEECROFT L. L., OBER Ch. K., *Chem. Mater.*, 9 (1997), 1302.
- [3] OOMEN E.W.J.L., VAN DONGEN A.M.A., *J. Non-Cryst. Solids*, 111 (1989), 205.
- [4] YOFFE A.D., *Adv. Phys.*, 42 (1993) 173, 50 (2001), 1.

- [5] BIGOT J.-Y., HALTE V., MERLE J.-C., DAUNOIS A., Chem. Phys. 251 (2000), 181.
- [6] GONELLA F., MATTEI G., MAZZOLDI P., CATTARUZZA E., ARNOLD G.W., BATTAGLIN G., CALVELLI P., POLLONI R., BERTONCELLO R., HAGLUND jr. R.F., Appl. Phys. Lett. 69 (1996), 3101.
- [7] HENCH L.L., WEST J.K., Chem. Rev., 90 (1990), 33.
- [8] ULRICH D.R., J. Non-Cryst. Solids 100 (1988), 174.
- [9] KLEIN L.C., *Processing of Nanostructured Sol-Gel Materials*, [in:] *Nanomaterials: Synthesis, Properties And Applications*, A.S. Edelstein and R.C. Cammarata (Eds.), Inst. of Phys. Publ., Bristol and Philadelphia, 1996, p. 147–164.
- [10] PROKOPENKO V.B., GURIN V.S., ALEXEENKO A.A., KULLKAUSKAS V.S., KOVALENKO D.L., J. Phys. D 33 (2000), 3152.
- [11] GURIN V.S., PROKOPENKO V.B., MELNICHENKO I.M., PODDENEZHNY E.N., ALEXEENKO A.A., YUMASHEV K.V., J. of Non-Cryst. Solids, 232–234 (1998), 162.
- [12] GURIN V.S., PROKOPENKO V.B., ALEXEENKO A.A., MELNICHENKO I.M., MIKHAILOV V.P., YUMASHEV K.V., MALYAREVICH A.M., *Functional Materials (Kharkov)*, 6 (1999), 464.
- [13] GURIN V.S., PROKOPENKO V.B., ALEXEENKO A.A., KOVALENKO D.L., MELNICHENKO I.M., J. of Inclusion Phenom. & Molecular Recogn., 35 (1999), 291.
- [14] GURIN V.S., PROKOPENKO V.B., ALEXEENKO A.A., SHIXIN WANG, YUMASHEV K.V., PROKOSHIN P.V., *Int. J. Inorg. Mater.* 3 (2001), 493.
- [15] GURIN V.S., PROKOPENKO V.B., ALEXEENKO A.A., FRANTSKEVICH A.V., *J. Mater. Chem.*, 11 (2001), 149.
- [16] ALEXEENKO A.A., GURIN V.S., PROKOPENKO V.B., YUMASHEV K.V., PROKOSHIN P.V., KOVALENKO D.L., 5th Int. International Conference on *Excited States of Transition Elements*, 6–11 June 2001, Wrocław, Łądek Zdrój, Poland, P01, to be published.
- [17] BOHREN C.F., HUFFMAN D.R., *Absorption And Scattering of Light by Small Particles*, Wiley, New York, 1983.
- [18] WOGGON U., *Optical Properties of Semiconductor Quantum Dots*, Springer, Berlin, 1996.
- [19] KLIMOV V.I., BOLIVAR P.H., KURZ H., KARAVANSKII V., *Superlatt. and Microstruct.*, 20 (1996), 394.
- [20] KLIMOV V.I., KARAVANSKII V.A., *Phys. Rev.*, B54 (1996), 8087.
- [21] WERKMAN P.J., WIERINGA R.H., SCHOUTEN A.J., *Thin Solid Films*, 323 (1998), 251.
- [22] LELOUP J., RUAUDEL-TEIXIER A., BARRAUD A., ROULET H., DUFOR G., *Appl. Surf. Sci.*, 68 (1993), 231.
- [23] CHOPRA K.L., DAS S.R., *Thin Film Solar Cells*, Plenum Press, New York, 1983.
- [24] ARTEMYEV M.V., GURIN V.S., YUMASHEV K.V., PROKOSHIN P.V., MALJAREVICH A.M., *J. Appl. Phys.*, 80 (1996), 7028.
- [25] YUMASHEV K.V., PROKOSHIN P.V., MALYAREVICH A.M., POSNOV N.N., MIKHAILOV V.P., GURIN V.S., ARTEMYEV M.V., *Appl. Phys.*, B64 (1997), 73, B65 (1997), 545.
- [26] YUMASHEV K.V., POSNOV N.N., DENISOV I.A., PROKOSHIN P.V., MIKHAILOV V.P., GURIN V.S., PROKOPENKO V.B., ALEXEENKO A.A., *J. Opt. Soc. Am.*, B14 (2000), 572.
- [27] VUCIC Z., MILAT O., HORVATIC V., OGORELEC Z., *Phys. Rev.*, B24 (1981), 5398.
- [28] MURRAY R.M., HEYDING R.D., *Canad. J. Chem.*, 53 (1975), 878, 54 (1976), 841.

Received 16 June 2001
Revised 22 December 2001

Preparation, spectroscopy and morphology of Nd:YAG nanostructures*

D. HRENIAK¹, W. STREK¹, P. MAZUR²

¹Institute of Low Temperature and Structure Research, Polish Academy of Sciences,
2 Okólna St., 50-950 Wrocław, Poland

²Chemistry Department, Opole University, Opole, Poland

The neodymium-doped yttrium aluminum garnet (Nd:YAG) nanocrystalline powders were prepared by sol-gel method. The synthesis of semitransparent polycrystalline ceramics is described. Their structure and morphology were studied by means of XRD and TEM methods. It was found that with increasing thermal heating the sizes of Nd:YAG grains increase. Optical properties of Nd³⁺:YAG nanocrystalline powders and ceramics are reported. The evident influence of the grain size on the luminescence of Nd³⁺ ions has been observed.

Key words: YAG, nanocrystalline ceramics, Nd³⁺ emission

1. Introduction

Since discovery of the stimulated optical radiation in Nd³⁺:YAG [1] this crystal found the most common application in quantum electronics. In recent years, the rare-earth ions-doped yttrium-aluminum garnet (YAG) single crystals have been the most widely used solid-state laser materials [2]. In the practical application as luminescence activator Nd³⁺ plays a more important role than do Ho³⁺, Tm³⁺ and Er³⁺ ions. The Ce³⁺, Tb³⁺ and Eu³⁺-doped YAG particles are also the subject of intense studies in view of their stability at the conditions of high irradiance as efficient host material of full-color phosphors [3, 4]. Crystal structure of Y₃Al₅O₁₂ is of characteristic cubic symmetry with lattice parameter $a = 12.004 \text{ \AA}$. The first attempts to construct the solid-state laser based on polycrystalline ceramics have been reported by de With et al. [5], Mudler et al. [6] and Sekita et al. [7]. The first reports on Nd³⁺-doped transparent ceramics fabricated by hydroxide co-precipitation process, solid-state reaction among oxides

*The paper presented at the International Conference on Sol-Gel Materials, SGM 2001, Rokosowo, Poland.

powders and vacuum sintering, adequate for optical applications and able to emit a laser beam were notified by Greskovich et al. [8], Vrolijk et al. [9] and Ikesue et al. [10–12]. This technique generally requires heat treatment at high temperatures above 1600 °C and in a special case of mechanical mixing [13]. The ceramics were composed of the grains of few tens microns. The highly transparent crystalline ceramics obtained by isostatically pressed method [8, 12] were characterized by excellent optical properties sufficient for laser operation. In recent years, there have been reported new low-temperature synthesis methods of fabrication of nanosized YAG crystallites by different wet chemical processes, i.e., a nitrate process [14], homogeneous precipitation [15–17] and alkoxide-acetate process [18]. In the case of homogeneous precipitation and alkoxide method (sol-gel method) there was reported a direct crystallization at YAG below 1000 °C [14]. In this work, we present the results of preparation and characterization of Nd³⁺-doped Y₃Al₅O₁₂ obtained by a modified sol-gel technology similar to that developed by Vaqueiro and Lopez-Quintela [15].

2. Experimental

Stoichiometric amounts of yttrium chloride (99.99%), aluminum nitrates (99%) were dissolved in aqueous citric acid solution to give a molar ratio appropriately of 3:5:16. Neodymium chloride (99.99%) was added in the precursor solution to give a Y:Nd atomic ratio of 100:5 and ultrasonically stirred for 2h at about 80 °C. The obtained solution was gelled at 80 °C for several hours and dried at 110 °C during the period of 3 days. Samples of the crushed gel were heat-treated at different temperatures in the air in an electric oven. In order to form crystalline Nd:YAG powders, the obtained gels were heated at 800 °C (sample A) and 1000 °C (sample B) for 16 h. Then, ceramic disks were fabricated from the sample A which was pressed at about 200 MPa in the air and in vacuum and sintered at 750 °C (samples C and D, respectively) and at 1400 °C (sample E) in the air for 16 h.

The microstructure of samples prepared was evaluated by transmission spectroscopy (TEM – Philips CM20 SuperTwin Microscopy operating at 200 kV and providing 0.25 nm resolution) and X-ray diffraction (XRD – Stoe Powder Sensitive Detector; filtered CuK α_1 radiation). Absorption spectra were measured at room temperature with a Cary 5 spectrophotometer. Emission spectra were measured at room temperature using Jobin-Yvon TRW 1000 spectrophotometer and a photomultiplier (Hamamatsu R406). All recorded spectra were corrected according to its characteristics. Emission lifetimes were measured by means of Tektronics TDS 380 oscilloscope. As excitation source we used the 532 nm line of doubled Nd:YAG laser.

3. Results and discussion

All the samples studied were light-blue. The structural analysis of samples as a function of the heating temperature is shown in Fig. 1. A lack of broad peaks indicates the high crystallization and ordering state of crystallites. Sharp peaks in the all recorded XRD patterns could be ascribed to cubic $Y_3Al_5O_{12}$ [19] and are the narrowest for the sample E (the largest crystallites). The average sizes of nanocrystallites were determined from the broadening of diffraction lines of X-ray patterns according to Scherrer's formula [20] and were estimated to be 25 nm for the samples A, C, D, and 98 nm and above 150 nm for the samples B and E, respectively. The evaluated values are confirmed also with transmission electron micrograph (TEM) presented below.

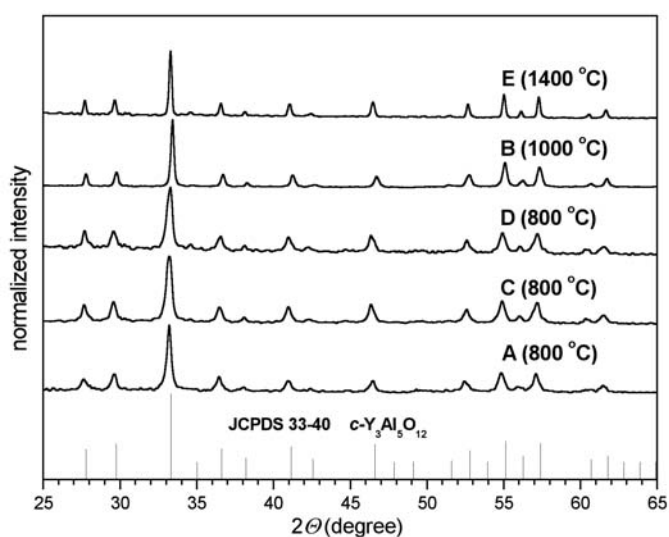


Fig. 1. XRD patterns of Nd:YAG heated at different temperatures:
 A – powder 800 °C, B – powder 1000 °C, C – pellet 750 °C,
 D – pellet 750 °C and E – pellet 1400 °C

The microstructures of Nd:YAG nanocrystallites are shown in Fig. 2. In TEM images of powders (Fig. 2a) dispersed grains of $Y_3Al_5O_{12}:Nd^{3+}$ (sample A) and the aggregates composed of this grains (Fig. 2b) for powder heat-treated at the higher temperature (sample B) are visible. The TEM images of powdered pellets (samples C and E, respectively, Figs. 2c, d) indicated that with increasing temperature of thermal treatment the size of grains increased by gradual aggregation and bonding of the smaller grains. One can note an increase of crystallite size with heating temperature from about 25 nm for sample A to 138 nm for sample E. These results are in agreement to the XRD data.

The absorption spectra of Nd:YAG nanocrystallites were recorded at room temperature. A comparison of the absorption spectra for the specimen pressed in air (sample C) and in vacuum (sample D) is shown in Fig. 3. The respective absorption transitions were determined and marked in the figure. One can note that for the same concentration of Nd^{3+} ions (1%) we have observed more distinct absorption bands for sample D compared to the sample C. High background in the blue region of spectra follows from rather poor low transparency of both samples.

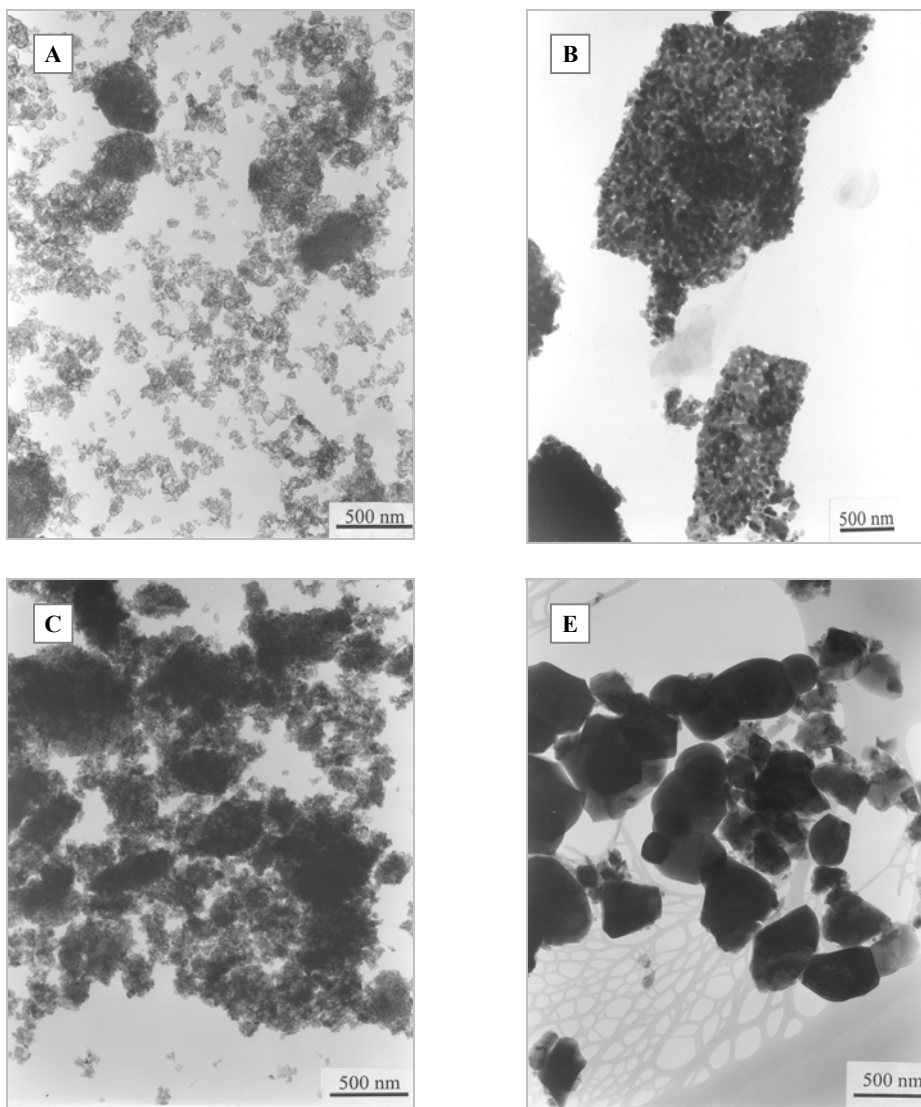


Fig. 2. TEM images of Nd:YAG nanocrystallites: A – powder 800 °C, B – powder 1000 °C
C – pellet 750 °C pressed in air and E – pellet 1400 °C

The emission spectra of Nd³⁺:YAG nanocrystallites measured at room temperature are shown in Fig. 4a. The spectra consist of two characteristic bands attributed to the $^4F_{3/2} \rightarrow ^4I_{9/2}$ (810–910 nm) and $^4F_{3/2} \rightarrow ^4I_{11/2}$ (1040–1070 nm) transitions. The positions of all emission lines are almost identical to those reported for Nd:YAG crystal.

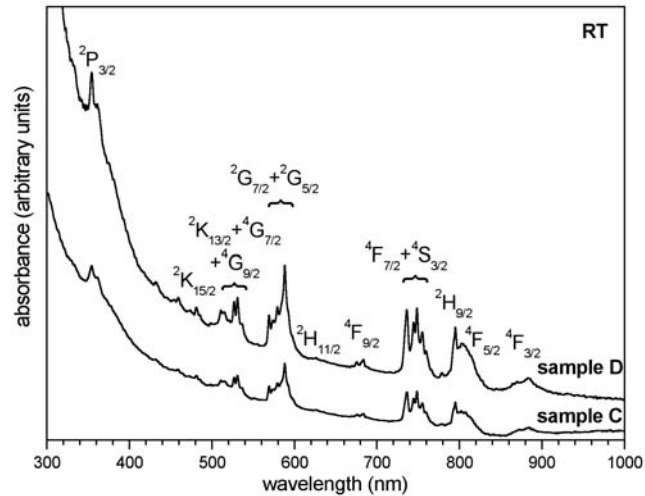


Fig. 3. Absorption spectra of Nd:YAG nanocrystalline ceramics obtained at two different temperatures of thermal treatment – the sample C (pellet 750 °C pressed at air), and the sample D (pellet 750 °C pressed in vacuum)

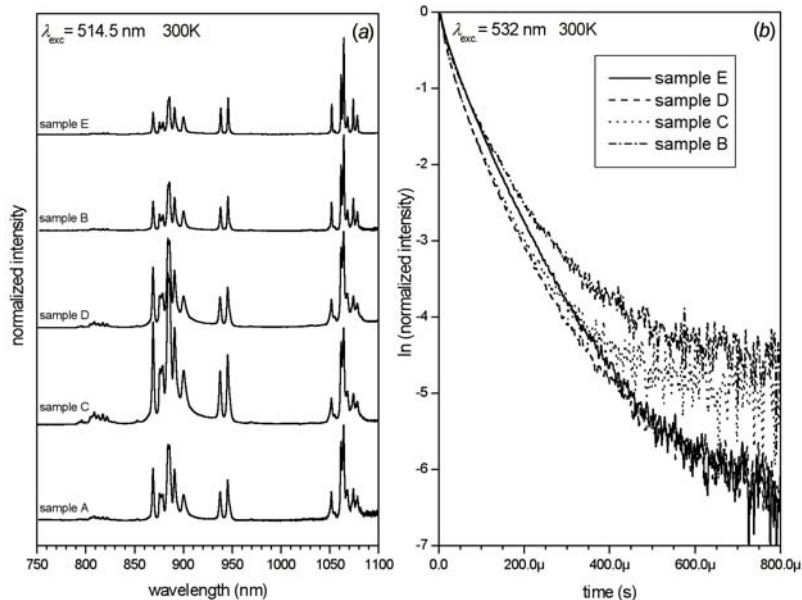


Fig. 4. Emission spectra of Nd:YAG nanocrystalline ceramics prepared at different temperatures of thermal treatment (a) and decay curves of Nd:YAG nanocrystallites emission at 884 nm measured at 300K after 532 nm pulse excitation (b)

It is interesting to note that in the range of 800–830 nm there was observed the band attributed to the ${}^4F_{3/2} \rightarrow {}^4I_{9/2}$ transition. It is extremely intense for the samples heated at lower temperature for which the crystallites sizes are the smallest. It was the strongest for the pellet pressed in air. With increasing crystallite sizes this band became much weaker (see B and E). Moreover, it is interesting to note that with increasing sintering temperature the intensity of the laser transition ${}^4F_{3/2} \rightarrow {}^4I_{11/2}$ increases compared to the second ${}^4F_{3/2} \rightarrow {}^4I_{9/2}$ band. This increase is most probably due to the increase of the nanocrystallite size. However, its nature needs further investigations. A comparison of the emission bands of the two pellets, the first pressed in air (C) and the second pressed in vacuum (D) points to strong enhancement of the ${}^4F_{3/2} \rightarrow {}^4I_{9/2}$ band intensity compared to the ${}^4F_{3/2} \rightarrow {}^4I_{11/2}$ band.

Table. The decay times observed after excitation by 532 nm line of a pulse line Nd:YAG laser measured at 300 K (decay times were approximated to the shortest and the longest component of each decay curve)

Sample	Size of grains/nm	$\tau_{\text{short}}/\mu\text{s}$	$\tau_{\text{long}}/\mu\text{s}$
C	25	20	120
D	25	20	137
B	98	20	152
E	138	30	128

We measured the dependence of the lifetimes of band attributed to the ${}^4F_{3/2} \rightarrow {}^4I_{9/2}$ transition on the size of Nd:YAG grains. The examples of emission decays measured at 884 nm are shown in Fig. 4b. The observed decay curves are distinctively non-exponential and are typical of heavily Nd-doped samples [22]. Such non-exponential curves could be approximated by many decays. Therefore, it is more reliable to find the shortest and the longest component. In our opinion, the first component is due to the concentration quenching of Nd^{3+} ions, and second to the isolated Nd^{3+} ion. Both the decay time components were evaluated from the decay profiles and are shown in the table. One can note that only the longest component evaluated for the sample B increases compared to the samples C and D to be 101 μs , 138 μs and 152 μs , respectively. We can explain this effect by removing OH groups from the closest surrounding of Nd^{3+} ions. The longest component of decay time estimated for the sample E is shorten more than those for the samples D and B. In our opinion, this fact is due to the aggregation process associated with grain increase.

4. Conclusions

The purpose of present paper was to report the modified synthesis of Nd:YAG nanocrystallites obtained by sol-gel method. Their morphology was investigated by XRD and TEM methods. It was found that with increasing temperature of thermal

treatment the size of Nd:YAG grains increased. The semitransparent ceramics composed from the Nd:YAG grains were prepared. Their absorption and emission properties were investigated. It was found that with increasing temperature of thermal treatment the intensity of ${}^4F_{3/2} \rightarrow {}^4I_{11/2}$ transition increased compared as to the ${}^4F_{3/2} \rightarrow {}^4I_{9/2}$ band. It was shown that the decay time of the luminescence was dependent on the size of the crystallites grains. Moreover, we have observed the emission originating from the ${}^4F_{5/2}$ state in small-size grains.

Acknowledgement

The authors thank Ms. L. Krajczyk for the TEM measurements. The studies were partially supported from the Polish Committee for Scientific Research (KBN) under Grant No. 4 T08A 046 22.

References

- [1] GEUSIC J.E., MARCOS H.M., VAN UITERT L.G., Appl. Phys. Lett., 4 (1964), 182.
- [2] KAMINSKII A.A., *Crystalline Lasers: Physical Processes and Operating Schemes*, CRC Press, Inc. Boca Raton, 1996, Chap. 1 .
- [3] KAHNG D., Appl. Phys. Lett., 13 (1968), 210.
- [4] DEPP S.W., HOWARD W.E., Sci. Am. 267 (3), (1993), 90.
- [5] DE WITH G., VAN DIJK H.J.A., Mater. Res. Bull. 19 (10), (1984), 1669.
- [6] MUDLER C.A., DE WITH G., Solid State Ionics 16 (1985), 81.
- [7] SEKITA M., HANEDA H., YANAGITANI T., SHIRASAKI S., J. Appl. Phys. 67 (1), (1990), 453.
- [8] GRESKOVICH C., CHERNOCH J. P., J. Appl. Phys. 44 (1973), 4599.
- [9] VROLIJK G. V., WILLEMS M.M, METSELAAR R., J. Am. Ceram. Soc. 6 (1995), 47.
- [10] IKESUE A., KAMATA K., YOSHIDA K., J. Am. Ceram. Soc. 78 (1), (1995). 225.
- [11] IKESUE A., KINOSHITA T., KAMATA K., YOSHIDA K., J. Am. Ceram. Soc. 78 (4), (1995), 1033.
- [12] IKESUE A., FURUSATO I., KAMATA K., J. Am. Ceram. Soc. 78 (9), (1995), 2545.
- [13] KEITH M. L., ROY R., Am. Mineral. 39 (1954), 1.
- [14] IIDA Y., TOWATA A., TSUGOSHI T., FUROKAWA M., Vibrational Spectroscopy 19 (1999), 399.
- [15] VAQUEIRO P., LOPEZ-QUINTELA M.A., J. Mater. Chem. 8 (1), (1998), 161.
- [16] SHOJI I., KURIMURA S., SATO Y., TAIRA T., IKESUE A., YOSHIDA K., Appl. Phys. Lett. 77 (2000), 939.
- [17] LU J., PRABHU M., XU J., UEDA K., YAGI H., YANAGITANI T., KAMINSKII A., Appl. Phys. Lett. 77 (2000), 3707.
- [18] GOWDA G., J. Mater. Sci. Lett. 5 (1986), 1025.
- [19] JCPDS 33–40.
- [20] KLUG P., ALEXANDER L. E., *X-ray Diffraction Procedure*, Wiley, New York 1954, Chap. 9 .
- [21] KUSHIDA T., MARCOS H.M., GEUSIC J.E., Phys. Rev. 167 (2), (1968), 289.
- [22] DANIELMAYER H.G., BLATTE M., BALMER P., Appl. Phys. 1 (1973), 269.

Received 25 January 2002

Revised 19 April 2002

Eu³⁺ - and Er³⁺ -doped SiO₂-TiO₂ sol-gel films for active planar waveguides*

L.Q. MINH¹, N.T. HUONG¹, C. BARTHOU², P. BENALLOUL², W. STREK³, T.K. ANH^{1,**}

¹Institute of Materials Science, NCST of Vietnam, Hoang Quoc Viet Road,
Hanoi, Vietnam, leminh@ims.ncst.ac.vn

²Laboratoire d'Optique des Solides UMR 7601, Université Pierre et Marie Curie,
4 Place Jussieu, 75252 Paris Cedex 05, France

³Institute of Low Temperature and Structure Research, Polish Academy of Sciences,
2 Okólna St., 50-950 Wrocław, Poland

Sol-gel films of SiO₂-TiO₂-doped with Eu³⁺ or Er³⁺ ions were prepared by spin coating with a variety of molar concentration ratios of tetraethoxysilane (TEOS) and titanium isopropoxide (TPOT). The ratios of SiO₂-TiO₂ were 90/10, 85/15, 80/20, 75/25 and the concentrations of Eu and Er ions varied from 10⁻³ to 5·10⁻² mol %. Silica-titania films annealed from 150 up to 900 °C decreased their thickness from 300 to 150 nm and increased the refractive index from 1.49 to 1.62. The multilayer (6–8 layers) silica-titania thin films with thickness of about 1.2–1.6 μm have been developed in order to make highly doped with Eu³⁺ or Er³⁺ planar waveguides on silicon substrates. Luminescence spectra, lifetimes as well as FTIR and micro-Raman spectra have been measured. The influence of active ion concentrations and annealing temperature on the luminescence properties and the structure of thin films were investigated.

Key words: *sol-gel method, Eu, Er, thin films*

1. Introduction

In recent years, great interest has been attracted by the development of integrated optics, which is the technology of integrating various optical devices and components for the generation, focusing, splitting, combining, isolation, polarization, coupling, switching, modulating and detection of light, all on a single substrate. The sol-gel process offers a versatile method for depositing amorphous films, based on the hydrolysis and polycondensation of precursors such as metal alkoxides.

*The paper presented at the International Conference on Sol-Gel Materials, SGM 2001, Rokosowo, Poland.

**Corresponding author. Institute of Materials Sciences, NCNST of Vietnam, Hoang Quoc Viet Road, Hanoi, Tel: 7564333/1153 Fax: 84-4-7562039, E-mail: kimanh@ims.ncst.ac.vn.

Trivalent rare earth ions such as Eu^{3+} - or Er^{3+} -doped into $\text{SiO}_2\text{-TiO}_2$ matrices are interesting and promising materials for active planar waveguides due to their advantages such as low temperature of processing, high homogeneity and possibility of producing materials with controlled refractive indexes. Optical amplification is also an important application (e.g. at the wavelength of 1.55 μm in channel waveguides doped with Er^{3+} and 980 nm pumps) which involves matrices inside in which concentrations of OH groups should remain extremely low. High refractive index variations between the guide and the cladding are necessary to induce maximum confinement and thus to increase doping efficiency. This field was, until recently, limited to pure inorganic materials or semiconductors. Hybrid materials, because of their versatility, fit both requirements [1].

These new optical materials are $\text{SiO}_2\text{-TiO}_2$ thin films containing rare earth ions prepared by the sol-gel technique [2]. The influence of titanium concentration on the refractive index and optical properties of $\text{SiO}_2\text{-TiO}_2$ thin films were presented previously [3]. The fabrication of nanoparticles by the sol-gel process opens up interesting possibilities for designing new devices for optical imaging and telecommunication applications. The compactness and performance of integrated lasers and amplifiers are mainly linked to the rare earth doping level. $\text{SiO}_2\text{-TiO}_2$ system offers the possibility of producing materials with controlled refractive indexes varying from 1.46 (of pure silica) to 2.2 (pure amorphous TiO_2). $\text{SiO}_2\text{-TiO}_2$ thin films doped with rare earth and dyes are intensely investigated as planar waveguides because of their homogeneity and the possibility of tuning the refractive indexes and the wavelength [3]. Sol-gel chemistry, combined with the spin-coating technique, is a good method for production of rare earth-doped planar waveguides [4].

In this paper, we present preparation and optical properties of sol-gel derived $\text{SiO}_2\text{-TiO}_2\text{:Eu}$ as well as $\text{SiO}_2\text{-TiO}_2\text{:Er}$ thin films.

2. Experimental

Preparation of the sol-gel thin films involves two main starting precursors: tetraethylorthosilicate ($\text{Si}(\text{OC}_2\text{H}_5)_4$, TEOS, 98%, Merck) and tetraisopropylorthotitanate ($\text{Ti}(\text{OC}_3\text{H}_7)_4$, TPOT, 97%, Fluka). Spin-on-glass method on Si substrates was employed to produce films. The film preparation was performed in a clean room of the class 100. Because TEOS and TPOT have very different hydrolysis rates, TEOS was first pre-hydrolyzed before adding TPOT in order to obtain clear solutions (hydrolyzates). The velocities of spin coating were 1000, 2000 or 3000 c/min. Molar ratios of TEOS-TPOT were 90/10, 85/15, 80/20 and 75/25. Eu and Er were doped by addition of $\text{Eu}(\text{CH}_3\text{COOH})_3/(\text{TEOS}+\text{TPOT})$ and $\text{Er}(\text{CH}_3\text{COOH})_3/(\text{TEOS}+\text{TPOT})$ with different concentrations varying from $5 \cdot 10^{-2}$ to $4 \cdot 10^{-3}$ mol/dm³. The films were fabricated on single-crystal silicon wafers (111) using a photoresist spinner. These films were spun at 1500–2500 rpm for 30 sec after deposition, then annealed at 50 °C for 48 hrs

and then sintered at temperatures between 150 °C and 900 °C for different times in a clean room of class 100.

The thickness and refractive indexes were measured using a spectroellipsometer. The thermogravimetric analysis (DTG or TGA) and vibrational spectroscopic (FTIR and micro-Raman) methods were performed in order to investigate the chemical reactions and structural transition during the thermal treatment process. The DSC and TG spectra were measured using Shimadzu DSC-50 (Japan). IR spectra were recorded using Shimadzu 5000 with a FTIR adapter. The samples were checked by means of X-ray diffractometer D 5000 (Siemens).

The photoluminescence spectra were studied on a monochromator Jobin Yvon HR 460, and a multichannel CCD detector from Instruments SA (model Spectraview 2D). This set-up has resolution of 0.2 nm/point with a slit 0.02 mm in the visible range. Triax 320 was used for infrared measurements. The luminescent spectra were also measured using a Spex 1250M monochromator with a high-resolution grating. Hg-Xe lamp (500 W, Oriel), nitrogen, argon, and Ti-sapphire lasers were used as excitation sources for the different wavelengths. The decay profiles were analyzed by a PM Hamamatsu R928 and Nicolet 490 scope with a time constant of the order of 7 ns.

3. Results and discussion

The refractive index of the sol-gel silica-titania thin films changes from 1.49 to 1.60 depending on the Ti concentration. Refractive indexes and thickness of 90SiO₂-10TiO₂, 85SiO₂-15TiO₂ and 80SiO₂-20TiO₂ thin films obtained at different annealing temperatures are presented in the table. The results of heating of the (100 - x)SiO₂-xTiO₂ films in the temperature range from 150 °C to 1000 °C indicate that while film thickness decreases (up to 800 °C), their index increases reaching constant values after heating at 800 °C for 10–25 min.

Table. Thickness (*d*) and refractive index (*n*) of (100 - x)SiO₂-xTiO₂ thin films at different annealing temperatures (*T*)

90SiO ₂ -10TiO ₂			85SiO ₂ -15TiO ₂			80SiO ₂ -20TiO ₂		
<i>T</i> /°C	<i>D</i> /nm	<i>n</i>	<i>T</i> /°C	<i>D</i> /nm	<i>n</i>	<i>T</i> /°C	<i>D</i> /nm	<i>n</i>
150	209.90	1.49	150	184.12	1.50	150	192.14	1.53
300	201.70	1.50	300	167.36	1.53	300	155.96	1.57
500	184.50	1.50	500	152.47	1.54	500	152.01	1.57
700	157.26	1.51	700	131.65	1.56	700	142.16	1.58
800	159.95	1.52	800	124.68	1.56	800	129.12	1.60
900	135.05	1.53	900	123.07	1.56	900	126.96	1.60

Some reaction parameters such as molar ratios of (TEOS + TPOT) to H₂O, pH, refluxing temperature and reaction times were investigated during preparation of the

solutions in order to minimize the final content of residual hydroxyl groups and the phase separation between silica and titania. Furthermore, the use of acetylaceton (ACT) as an inhibitor for hydrolysis reaction of TPOT has already been shown to be of great value in improving the sol-gel processing. The stability of the initial sol-gel solution of the two metal alkoxides of silicon and titania enables preparation of homogeneous mixtures.

The FTIR spectra of 80SiO₂/20TiO₂ thin films obtained at different temperatures have been already presented [4]. In the spectra of films sintered at <750 °C the O–H stretching feature is observed near 3450 cm⁻¹, where both H₂O (~3350 cm⁻¹), SiOH (~3680 cm⁻¹) components are present. The Si–O–Si vibrational modes ascribed to the transverse optical rocking, symmetric stretching and asymmetric stretching are observed at ~460 cm⁻¹, 800 cm⁻¹ and 1085 cm⁻¹. An intense shoulder is also observed at about 1250 cm⁻¹. It is related to the longitudinal optical component of the high-frequency vibration of SiO₂. All spectra exhibit a band centred near 920–940 cm⁻¹. On the other hand, in the micro-Raman spectra of the TiO₂ films (heated at 800 °C) several stretching vibrations of Si–OH and Si–O–Ti⁴⁺ linkages with characteristic bands at 633, 510, 388, 130 cm⁻¹ are present. The vibrations are similar to those observed for the anatase modification. When the molar ratio (*x*) of the (100 – *x*) SiO₂–*x*TiO₂ film was raised, the bands (at 1600 and 1340 cm⁻¹) characteristic of the Si–O–Si bonds could be observed.

In short, three kinds of physicochemical processes may occur when temperature is increased during thermal densification of gel films. First, residual water and residual organic groups are released, emptying the pores in the films. Second, the porous skeleton collapses, causing film shrinkage accompanied by structural relaxation, which can be described by the viscous sintering kinetic theory. Finally, crystallisation or phase separation may occur at high enough temperatures, depending on the chemical composition and dynamic conditions. According to the FTIR spectra, the C–H vibration were not found near 3000 cm⁻¹ even before sintering, showing that most organics were immediately removed during spinning, before thermal densification occurred.

The film shrinkage continues up to 900 °C. Densification at 1000 °C does not lead to continuous shrinkage due to oxidation of the silicon substrate. The refractive index also reaches a constant value, corresponding to each temperature. In addition, the results of TGA and DTG analyses of the gel films show that in the temperature range from 600 °C to 1000 °C the weight loss is negligible. This can be used to optimize annealing conditions in order to relax residual stresses of the SiO₂–TiO₂ gel films.

The sol-gel thin films SiO₂–TiO₂:Eu at different annealing temperatures demonstrate characteristic ⁵D₀–⁷F_J transitions of Eu³⁺ in luminescent spectra. The spectra recorded at two different annealing temperatures (500 °C and 700 °C) are shown in Fig. 1. The luminescence decay profiles of the thin film SiO₂–TiO₂[75/25]:Eu (1·10⁻² mol/dm³) annealed at 400 °C during 15 min are shown in Fig. 2.

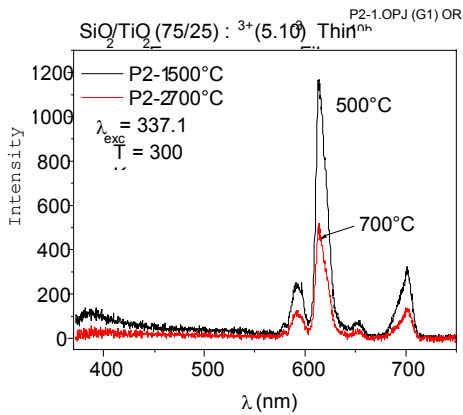


Fig. 1. The luminescence spectra of SiO₂-TiO₂: Eu (5·10⁻² mol/dm³)

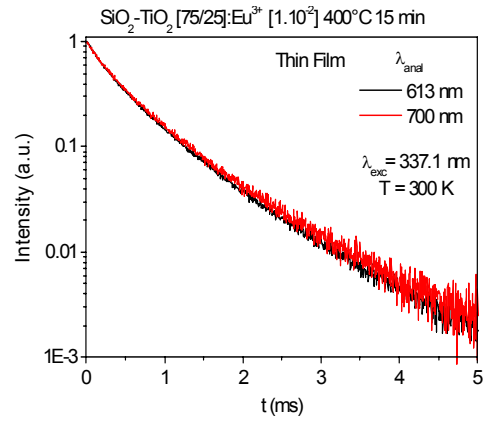


Fig. 2. The emission decay profiles of the thin film SiO₂-TiO₂: Eu (1·10⁻² mol/dm³), 400 °C

The luminescence spectra of SiO₂-TiO₂:Er samples were measured with an argon laser as an excitation source. For the emission spectra in the visible range, an interference filter (490 nm) was used to select the wavelength of excitation $\lambda_{exc} = 488$ nm or 514.5 nm. For the emission spectra in the near IR range, all the lines of the argon laser were used (no filter).

We have measured the $^4I_{13/2}$ - $^4I_{15/2}$ transition of Er³⁺ in the infrared region. The thermal processing decreased the presence of OH and transformed the structure of TiO₂ from anatase into rutile. The luminescence spectrum of the SiO₂-TiO₂:Er 10⁻² mol/dm³ annealed at 1000 °C using an argon laser as an excitation source is shown in Fig. 3a. A similar spectrum was observed using a sapphire laser (Fig. 3b).

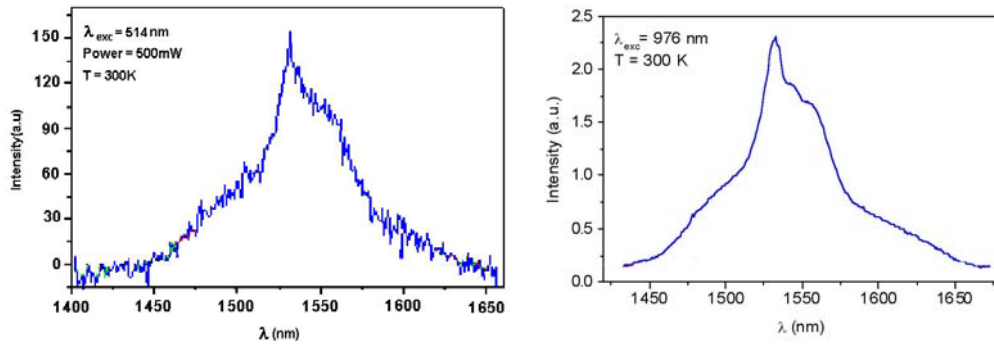


Fig. 3. Luminescence spectrum of: a) SiO₂-TiO₂:1% Er with 514 nm excitation, b) SiO₂-TiO₂: 1% Er with 830 nm excitation

4. Conclusions

The sol-gel derived SiO₂-TiO₂ thin films doped with Eu³⁺ and Er³⁺ were prepared. Their optical properties were studied as a function of active ion concentration and different annealing temperatures. The characteristic emission transitions of Eu³⁺ and Er³⁺ ions were observed. The refractive index of SiO₂-TiO₂ thin films can be tailored in a wide range by controlling the relative quantity of the starting precursors. Thin films of (100 -x)SiO₂-xTiO₂ doped with Eu³⁺ and Er³⁺ ions were spin coated on Si substrates. The effect of thermal treatment was investigated by means of vibrational spectroscopic measurements. We have found that the film thickness decreases whereas the refractive index increases continuously with increasing temperature of annealing. The experimental results demonstrate that for consecutive spin coating depositions each spun layer should be annealed at 750 °C to release residual stresses. The luminescence measurements indicate that the SiO₂-TiO₂ films doped with Eu³⁺ and Er³⁺ are promising materials for planar waveguides [5, 6].

Acknowledgement

We would like to thank Prof. Nguyen Van Hieu, Hanoi, Prof. C. Sanchez, Paris, Prof. C. Laubschat, Dresden, and Prof. K. Maruszewski, Wrocław for their help in performing these studies. Our work was financially supported by the project Franco-Vietnamese, the Institute of Materials Science, NCNST of Vietnam, the International Training for Materials Science, and the DAAD of Germany.

References

- [1] CHANCHEZ C., LEBEAU B., MRS Bulletin, May 2001, 377.
- [2] Barbier D., Orignac X., Du X.M., Almeida R.M., J.of Sol-Gel Science and Technology, 8 (1997), 1013.
- [3] HUONG T.T., ANH T.K., KHUYEN H.T., MINH L.Q., BARTHOU C., *Trends in Materials and Technology*, Proc. of the Third International Workshop on Materials Science IWOMS'99, Hanoi, 2-4 November 1999, 669.
- [4] ANH T.K., MINH L.Q., HUONG T.T., VU N., HUONG N.T., BARTHOU C., *Physics and Engineering in Evolution*, D.T. Cat, V.T. Son and A. Pucci (Eds.), 2000, 166.
- [5] ORIGNAC X., BARBIER D., DU X.M. ALMEIDA R.M., Appl. Phys. Lett., 69 (1996), 895.
- [6] Vu N., Anh T.K., Toan N.N., Hieu N.V., Barthou C. Minh L.Q., *Trends in Materials and Technology*, Proc. of the Third International Workshop on Materials Science IWOMS'99, Hanoi 2-4 November 1999, 645.

Received 16 June 2001
Revised 17 December 2001

Role of fluorine ions in the formation of silica gel structure and gel glass*

E.N. PODDENEZHNY¹, A.A. BOIKA², B.V. PLUSCH¹,
M.N. KAPSHAI¹, I.P. KRAVCHENKO¹, I.M. MELNICHENKO¹

¹Gomel State University, 104 Sovetskaya St. 246699 Gomel, Belarus

²Gomel State Technical University, 48 October av., 246746 Gomel, Belarus

Fluorine containing silica gels can be used as precursors of anhydrous glasses for fibre optics. The silica gels were prepared by the sol-gel process including the following stages: hydrolysis of tetraethylorthosilicate (TEOS) in a four-component system $\text{Si}(\text{OC}_2\text{H}_5)_4\text{-C}_2\text{H}_5\text{OH-H}_2\text{O-HCl}$, addition of fumed silica (aerosil) into the sol, sono-activation, centrifugal separation, neutralization by the ammonia solution, gelation, washing the gels in distilled water, drying and fluorination of the xerogels by the procedure of heating in the freon/oxygen atmosphere or impregnation in F-containing solutions. Fluorinated gels were consolidated into transparent silica glass in the atmospheres of air or helium gas at temperatures of 1200–1300 °C. SEM and AFM analysis and BET surface area investigations were used for characterization of the xerogels and glasses morphology. The optical properties of pure and fluorine-containing silica glasses were studied by VIS-and IR-spectroscopes.

1. Introduction

Fluorine has recently become a popular dopant for lowering of the refractive index of pure silica glasses for optical fibres [1]. Also, the F-doped, graded-index (GI) fibres with low OH content may be proper candidates for operation at 0.85 and 1.3 μm , since they display basically low losses at 1.3 μm , what differs them from other fibres-including boron oxide [2]. Utilization of the sol-gel process for synthesis of fluorine-doped silica glass is preferable because of its low sintering temperature and high efficiency [3]. Incorporation of fluorine into a xerogel reduces bubble formation upon consolidation by sintering and eliminates glass bloating during fibre drawing at high temperatures (2000–2200 °C). The fluorine doping is a very complicated process [3]. As shown for the gas phase doping, F content depends on the specific surface area of the starting dry gels and the conditions of the treatment. The defluorination by liberation of SiF_4 at high temperatures results in lowering of the dopant content in silica glasses and forming of the refractive index gradient in silica-glass rod-like pre-forms. The method of the liquid-phase doping by addition of the fluorinated silicon alkoxide ($\text{Si}(\text{OC}_2\text{H}_5)_3\text{F}$) into the sol solutions results in rising of the F content in the silica glasses [1].

The method of the liquid-phase doping by using F-containing compounds (NH_4F) was previously described [4]. However, maximum values of the fluorine contents were limited

*The paper presented at the International Conference on Sol-Gel Materials, SGM 2001, Rokosowo, Poland.

to 0.2% (by weight). The mechanism of the F-doping into gel pre-forms by using NH_4F as a fluorine source and structural behaviour of the dopant ions in the silica gels and glasses has been also described [5]. Silica xerogels made by a modified sol-gel process were used for the liquid phase F-doping with organic solutions of NH_4F and HF [6].

This paper describes the fabrication technique yielding fluorine-doped silica gels and glasses in the modified sol-gel process and the effect of F ions on structural properties and morphology of the xerogels. Optical properties of sintered pure and fluorinated silica glasses are also discussed.

2. Experimental

The F-doped xerogels and glasses were prepared by the sol-gel process [6] with the doping technique. The flowchart of the modified sol-gel process is shown in Fig. 1 and it displays the following stages: the TEOS hydrolysis in the system $\text{Si}(\text{OC}_2\text{H}_5)_4\text{-C}_2\text{H}_5\text{OH-H}_2\text{O-HCl}$ with mole ratio 1:2:16:0.01 by vigorous mixing in fluoroplastic reactor in the air, addition of fumed silica with a specific surface $200\text{ cm}^2/\text{g}$ (aerosil T30, Wacker-Chemie GmbH, Germany) into the sol as a tiller, ultrasonic dispersion with vigorous stirring and centrifugal separation from agglomerates and dust particles. Then, the sol-colloidal system was neutralized (up to $\text{pH} = 6.5$) with the help of an ammonia solution and cast into fluoroplastic moulds to yield solid gels shaped as disks and rods. The wet gels were formed during 20–30 min in sealed containers; then the containers were opened and the gels were washed with distilled water.

The resulting gels were dried slowly at 30–60 °C for 7–14 days in the air. The drying step should not induce cracking or warping of large gels. This was ensured by employing special containers: thorough and unidimensional removal of solvents and water was provided (no mechanical stresses were accumulated). After drying the xerogels were doped with fluorine by the gas-phase or liquid-phase dopings. The mixture of freon ($\text{C}_2\text{Cl}_3\text{F}_3$)/oxygen was used for the gas-phase doping. Dried xerogels were placed in pure silica glass tubes in a horizontal furnace and the temperature was increased up to 1000 °C with the rate of 250°/h. The mixture of freon/oxygen gases was flowed into the tube at room temperature with the rate of 0.2 dm^3/min . During heating in oxygen the organic compounds were burned out at about 500 °C and fluorine was incorporated

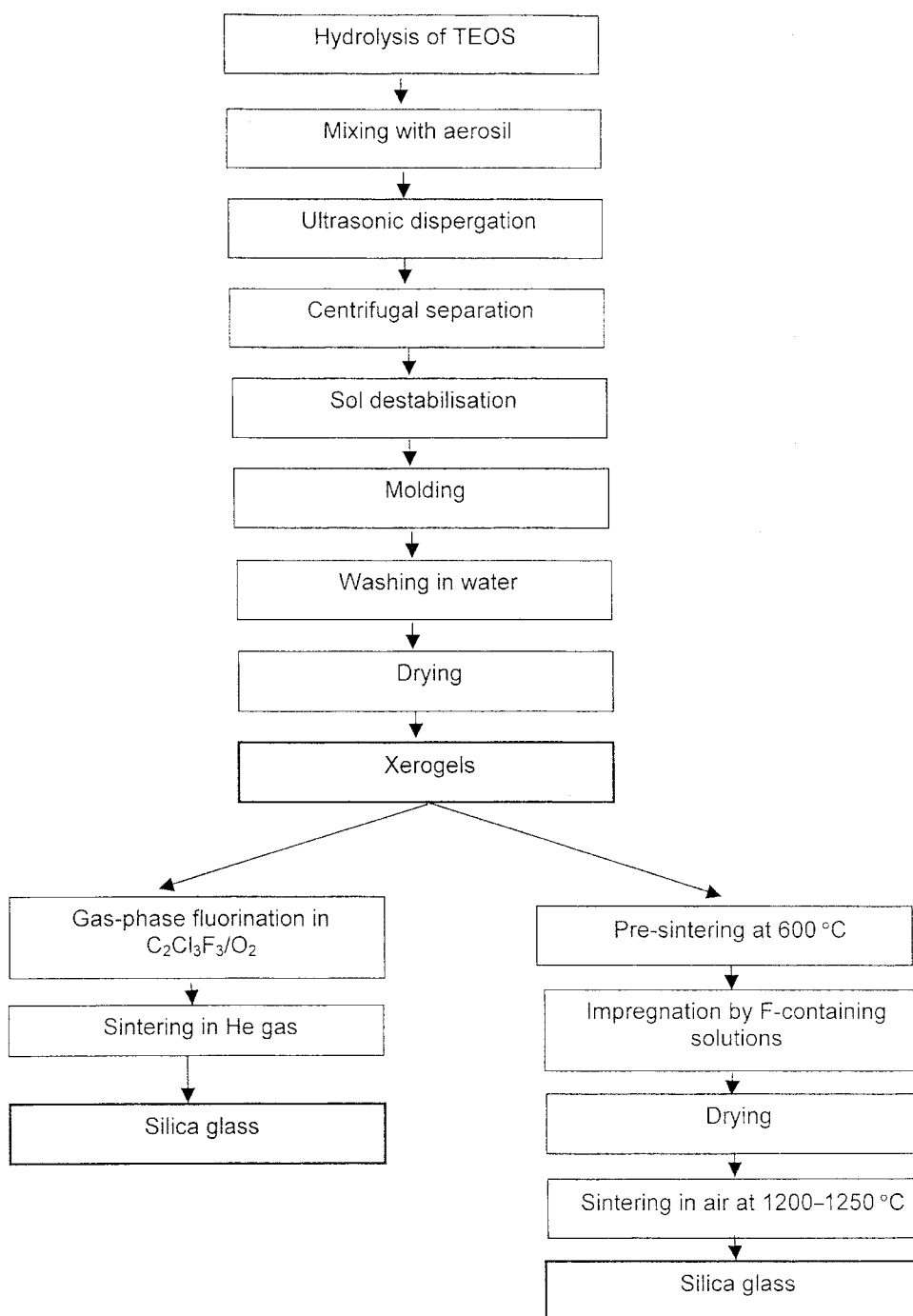


Fig. 1. Scheme of the silica gel glass preparation

into the porous gel structure, replacing the OH groups. The modified liquid-phase doping procedure does not require high temperatures for the fluorination and the process of introducing OF the F ions into xerogels takes place at the room temperature. The pre-sintered xerogels (600 °C, in the air) were impregnated in organic solutions containing the F ions. Such organic solvents as acetone, ethanol and isopropanol were employed due to their low surface tension.

F-containing water solutions used for the gels impregnation resulted in cracking the monolithic gels into fragments. The impregnation of the disk samples in the F-containing solutions was performed in vacuum (5–10 Torr). The modified gels were dried at 30–60 °C for 10–14 h. The consolidation into the transparent silica glasses was carried out at 1200–1300 °C in the air atmosphere. Using F-containing organic solutions for the doping allows us to obtain transparent silica glasses without cracks or warping. The specific surface areas and related pore volumes of the drying gels (xerogels) were measured by the BET method using argon adsorption at the liquid nitrogen temperature. The pore size distribution was calculated from the benzol adsorption-desorption isotherms [7].

Samples of the xerogels dried at 60 °C have been heated in the air from room temperature up to several final temperatures varying from 60 °C to 1200 °C (60 °C; 600 °C; 800 °C; 1000 °C; 1100 °C; 1200 °C). The samples were exposed for 2 h to each temperature.

The SEM and AFM analyses were used for characterization of the xerogels and sintered glasses morphology during the course of the samples heating. Optical absorption spectra were measured using the glass samples 2–4 mm thick by means of a spectrophotometer SPECORD IR-75 (in the IR-region) and BECKMAN-5270 in the visible and UV-regions.

The hydroxyl content in dense glass samples has been calculated from the IR absorption spectra using the relationship [8]:

$$[\text{OH}] \text{ [ppm]} = \frac{1000}{t} \log \frac{T_a}{T_b}$$

where: t – sample thickness (mm), T_a – transmission at 2.6 μm , T_b – transmission at 2.72 μm .

The refractive index (RI) of the fluorinated glass was measured using spatial filtering technique employing pure silica glasses as a standard. The RI -profiles in rods, prepared by the method of gas-phase doping, were measured using special equipment (P102 York Technology Ltd.). The effective fluorine and chlorine concentrations in silica gel glass were measured by the method of micro-X-ray diffraction spectral analysis (MXRSA) (CAMEBAX, France).

3. Results and discussion

3.1. Porosity and morphology of gels

The porosity parameters and specific surface area (S) for the xerogel and glass samples heated at a temperature range 60–1200 °C in air are given in the table.

Table. Porosity parameters and specific surface area (S) for the xerogel and glass samples

Sample	Temperature of treatment/°C	$S/(m^2/g)$	Pore volume/(cm^3/g)	Maximum d_{pore}/nm	Remarks
1	60	226	0.528	2.5, 13.0	bimodal
2	600	224	0.718	2.5, 6.0, 12.0	trimodal
2F*	600	197	0.254	3.0, 5.0, 25.0	
3	800	250	0.825	2.5, 6.0, 20.0	
4	1000	233	0.605	3.0, 6.0, 23.0	
5	1100	6.2	0.013	3.0, 5.0, 23.0	
6	1200	0.0	0.0	nonporous	silica glass

*The sample fluorinated at 600 °C by the liquid-phase doping technique.

From the consideration of the table we can state that pore volume increases until heating up to 800 °C and when the temperature rises up to 1100 °C the process of pore collapse is began, resulting in 1.6% of porosity. At the temperature of 1200 °C the pores are eliminated and the density becomes equivalent to fused silica.

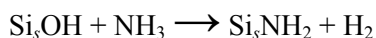
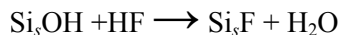
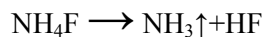
There is a little change in the pore distribution of the hybrid silica gels until heating to the interval 800–1100 °C. Densification primarily is due to only the number of pore decreasing.

During heating of xerogels up to 600 °C the densification process of silicate skeleton takes place, the liquid is removed from the interconnected pore network, the organics are burned and NH_4Cl is sublimated. The pore volume increases as a result of the surface area and pore size rising.

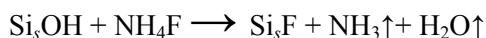
Polycondensation reactions continue to occur within the xerogel network and removing of intermicellous liquids increases the surface area (up to 800 °C). Then the removal of hydrogen-bonded water ($Si-OH...H_2O$) and surface silanol (Si_s-OH) groups (partially) from the pore network results in chemically stable and mechanically durable xerogels [9].

The pore distribution for undoped (1) and liquid-phase fluorinated (2) silica xerogels fired at 600 °C are shown in Fig. 2. It is seen that soaking of silica xerogels in the solution of F-containing chemicals (NH_4F + acetone) followed by heating at 600 °C in air, results in the loss of specific surface area and increasing of a pore size. The pore-size distribution of fluorinated gels also has a trimodal character: the network contains micropores (3.0 nm), mezo- and macropores (5.0–25.0 nm). The pore size

can be large by chemical attack of silica network with fluorine ions in solution and also in vapour phase until heating and dissociation of ammonium fluoride [10]:



or directly:



The fluorinated gels have been densified in air in the temperature as low as 1150–1180 °C.

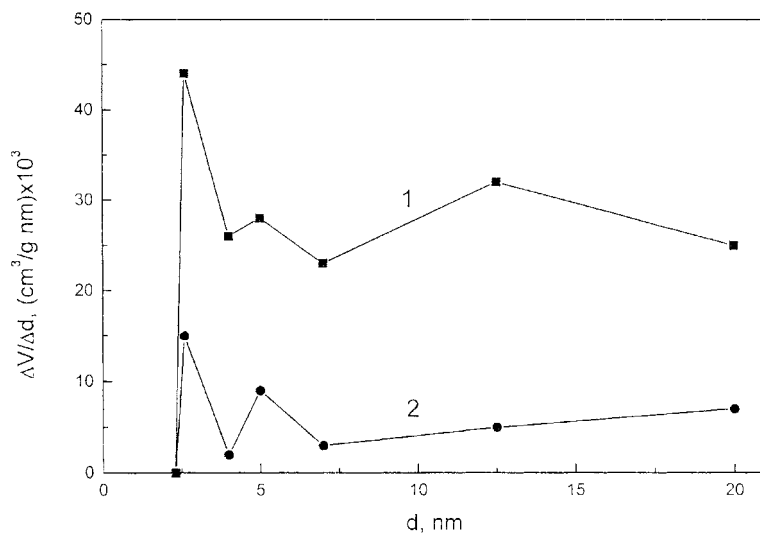


Fig. 2. Pore size distributions in undoped (1) and fluorinated (2) silica xerogels fired at 600 °C

Figure 3 shows SEM fracture surfaces of xerogel samples, heated at 60 °C (A); 600 °C (B) and 100 °C. The photos A and B display that the xerogel structure is formed from globular-chain units. The pore network contains the pores of transition character. The structure of sample 5 (the table) has a globular topology with a small volume of macropores (pre-glass). The authors [11] suggest that the formation the layered structure in hybrid gels may be possible and results from the polymerization of alkoxide-derived fractal particles in hybrid sol-gel systems.

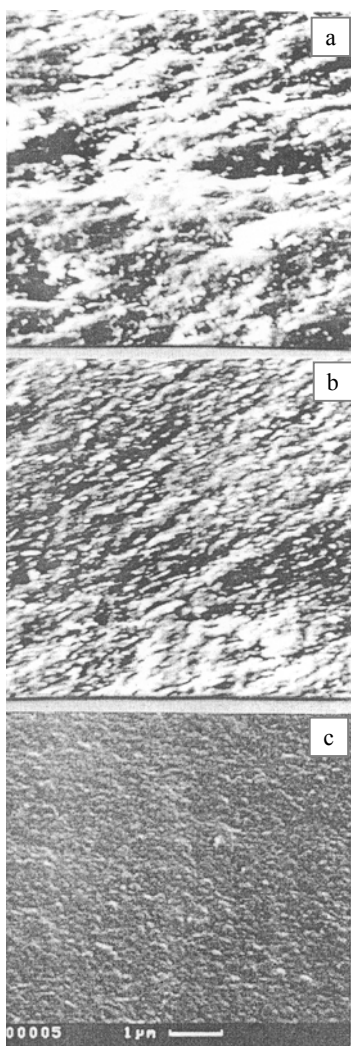


Fig. 3. SEM photos showing the fracture surfaces of xerogels heated at 60 °C (a), 600 °C (b) and 1100 °C (c)

Sample 6 (sintered silica gel glass) after chemical etching in 40% HF (Fig. 4) shows the globular structure, formed from units having the dimensions of about 100 nm probably from the reorganization of globular-chain agglomerates.

The Atomic Force Microscopy (AFM) analysis at 600 °C-heated samples shows that the structure of fired xerogels has a rigid character with the units dimensions of about 10–20 nm and corresponds with SEM morphology.

The fracture surface of the fluorinated silica gel glass, sintered in helium gas after the process of vapour-phase doping (from the mixture freon/oxygen) has been observed using an AFM microscope. A homogeneous structure formed from units sized of about 5–10 nm can be seen. The roughness and the globule dimensions of fluorinated gel-glass structure are decreased and the transparency of F-containing glass rises, compared with the undoped gel glass.

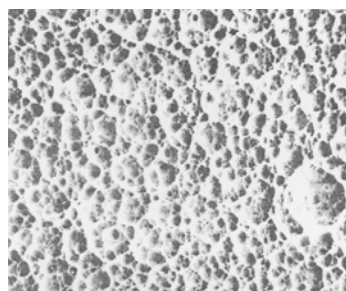


Fig. 4. SEM photo of etching surface of silica gel glass (40% HF, 30 min), magnitude $\times 500$

3.2. Optical characteristics of undoped and fluorinated silica gel glasses

A major problem in producing silica gel-glass optics is removal of surface hydroxyl groups and hydrogen-bonded pore water, which gives rise to atomic vibration energy absorption in almost the entire range from ultraviolet to infrared radiation (160–4500 nm) and decreases the optical applications of silica gel monoliths [9].

Some fluorine-containing compounds (HF, NH_4F , NH_4HF_2 , CF_2C_2 , $\text{C}_2\text{F}_3\text{Cl}_3$ etc.) can react with surface hydroxyl groups and gel silica network at elevated temperature, replacing OH ions and forming the fluorine-containing volatile substances (SiF_4 , SiF_3).

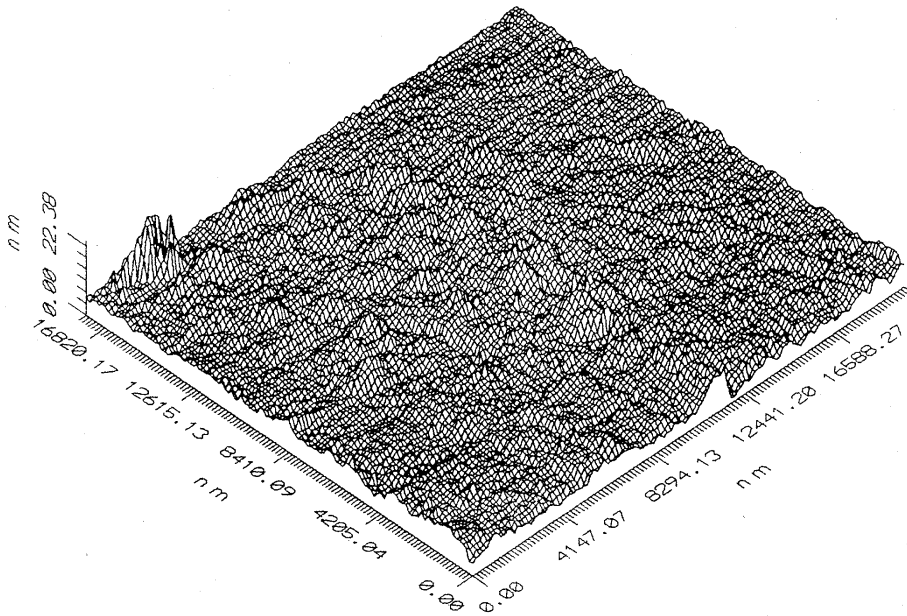


Fig. 5. AFM topography of silica gel (600 °C) fracture surface

The IR spectrum of gel glass samples is shown in Fig. 7. The sample thickness was 4.0 ± 0.1 mm. The undoped silica gel glass, prepared by the vitrification at the temperature of 1200 °C in air without any special dehydroxylation contains the hydroxyls between 2000 to 2500 ppm (curve 1).

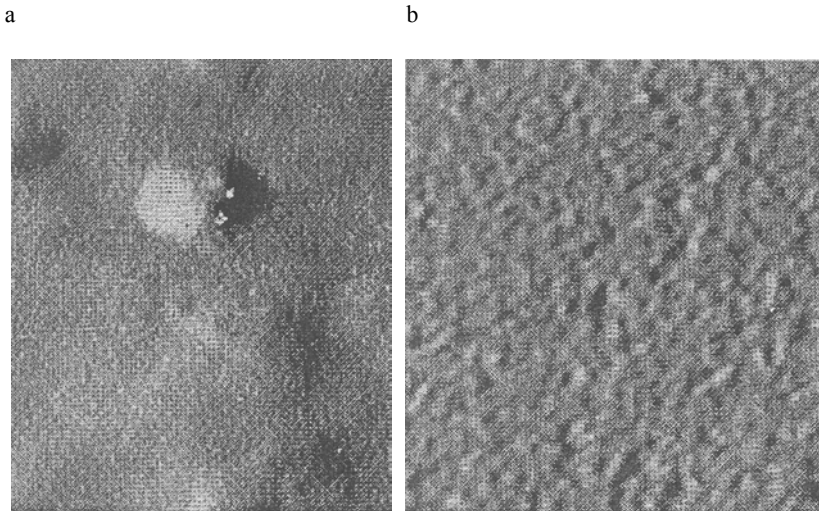
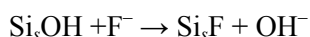


Fig. 6. AFM micrographs of fluorinated silica gel glass.
Scale images: a) $10 \times 10 \mu\text{m}$, b) $1.7 \times 1.7 \mu\text{m}$

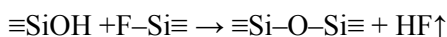
By liquid-phase doping procedure it is probably not possible to eliminate completely the OH groups from the silica porous network surface and a significant part of hydroxyl ions remains in the volume of glass after consolidation. The k_λ for samples 2 and 3 (Fig. 7) corresponds to the residual OH⁻ content of 30–80 ppm.

The process of gas-phase fluorine doping reduces hydroxyl level in the dense silica glass to below 3–5 ppm (curve 4 in Fig. 7). The contents of fluorine determined by the MXRSA for sample 4 is 0.4–0.45% by weight. Such glasses have about 90% transmission at 3671 cm⁻¹ (hydroxyl group absorption) region. The gas-phase doped sample contains also the chlorine contamination of 0.17% by weight.

At the temperature higher than 600 °C the F-containing compounds (obtained in the process of thermo-destruction of freon/oxygen mixture) attack the gel network and the reaction of OH⁻ groups substitution takes place:



During the densification process in the He gas atmosphere (1000–1300 °C) both hydroxyl and fluorine ions remain in the adjacent sites on the surface of the pore structure and the condensation reaction takes place with the elimination of HF [5]:



The F-containing substances volatilized during the process of xerogel consolidation in helium gas can result in forcing the gradient of refractive index in glass body.

The refractive index of the sintered in air silica glass measured $n_D^{\text{air}} = 1.4570$ and was decreased by sintering in helium gas after the fluorination in freon/oxygen atmosphere ($n_D^{\text{F}} = 1.4532$). A special technique of double gas fluorination was employed for the preparation of silica glass with minimum refraction index value $n_D^{2\text{F}} = 1.4507$ and the hydroxyl level to below 1 ppm.

By the method of gas-phase fluorination the rod pre-forms for optical fibre drawing were prepared. Typical size of the glass rods was 22 mm in diameter and 130 mm long. A pre-form has a gradient refractive index profile owing to fluorine removing from the external layers of porous rod during the consolidation process in helium. The refractive index difference Δn between external and internal parts of pre-form equals 0.00042.

4. Conclusions

Silica glasses doped with fluorine were prepared by the sol-gel method using gas-phase and liquid-phase doping.

The process of gas-phase fluorination with using of freon/oxygen mixture results in preparing of silica gel glass with the concentration of OH⁻ groups of 1–5 ppm. Liquid-phase doping procedure is probably not able to eliminate the hydroxyls completely and the residual OH content is 30–80 ppm.

The study of morphology and porosity parameters by the SEM, AFM and BET methods has shown the effect of fluorine ions on pore structure and specific surface area of xerogels. Fluorinated gels are of low pore volume and decreased specific surface area. Effective fluorine concentrations are between 0.2 and 0.45% by weight.

The refractive index n_D of the air-sintered silica gel glass is 1.4570 and for the fluorinated samples it decreased to $n_D^{2F} = 1.4507$.

By the method of gas-phase fluorination the rod pre-forms for optical fibre drawing were prepared with typical size of 22 mm in diameter and 130 mm long. A pre-form has a gradient refractive index profile because of partially fluorine removing and the difference consists $\Delta n = 0.00042$.

References

- [1] SHIBATA S., KITAGAWA T., HORIGUSHI M., *Fabrication of fluorine-doped silica glasses by the sol-gel method*, J. Non-Cryst. Sol. 100 (1988), 269.
- [2] SANADA K., SHAMOTO T., INADA K., *Radiation resistance characteristics of graded index fibre with a core of Ge-F-doped or B and F-codoped SiO₂ glass*, J. Non-Cryst. Sol., 189 (1995), 283.
- [3] SHIBATA S., *Sol-gel-derived silica pre-forms for optical fibres*, J. Non-Cryst. Sol., 178 (1994), 272.
- [4] ZHONGCHENG W., RENJIE T., QING S., MEIE C., *Synthesis the F-doped silica tubes using the sol-gel process*, Proc. of XVII Int. Congress on Glass, V.4 (1995), 544–547, Beijing, China.
- [5] SIJIAN G., ZHENAN G., *Structural behaviors of fluorine in silica gels and glasses*, Proc. of XVI Int. Congress on Glass, V.7 (1992), 39–44, Madrid, Spain.
- [6] BOIKO A.A., Poddenezhny E.N., MELNICHENKO I.M., PLUSCH B.V., *Liquid-phase doping of xerogels by fluorine with aim of silica glass dehydration*, Materials, Technologies, Tools, NI (1998), 77.
- [7] BOIKO A.A., Poddenezhny E.N., MELNICHENKO I.M., BAGLAY A.K., OSTROVSKI L.K., *The physical-chemical study of gels forming in the process of doped sol-gel silica glass preparation*, Proceedings of Bielorrussian Academy of Sciences, Series of Chemical Sciences, No. 4 (1994), 1 01.
- [8] POPE E.J.A., MACKENZIE J.D., *Nd-doped silica glass. 1. Structural evolution in the sol-gel state*, J. Non-Cryst. Sol. 106 (1988), 236.

Received 16 June 2001
Revised 17 December 2001

Enzyme electrodes constructed on the basis of oxygen electrode with oxidases immobilised by sol-gel technique*

MAŁGORZATA PRZYBYT, BEATA BIAŁKOWSKA

Technical University of Łódź, Department of Food Chemistry and Biotechnology,
Institute of General Food Chemistry, Stefanowskiego 4/10, 90-924 Łódź, Poland,
mprzybyt@snack.p.lodz.pl

The results of immobilisation of enzymes in silica gel on oxygen electrode are reported. As the model, enzyme glucose oxidase was used. The influence of the composition of the casting solution (gel precursor, pH of the enzyme solution, sol to buffer ratio) on the electrode response was investigated. Also, the addition of γ -aminopropyltriethoxysilane to the casting solution was checked. The best electrode with stable signal was obtained, when the formed gel was not very rigid (buffer, pH 6 or 7 and high buffer to sol ratio). For the optimal composition of the casting solution, some properties of the glucose electrode were investigated (stability, pH profile and influence of temperature). The method of sol-gel entrapment was also used to obtain the electrodes sensitive for disaccharides by co-immobilisation of invertase, lactase and maltase with glucose oxidase. In addition, preliminary results for other oxidases immobilised by this method are presented.

Key words: *enzyme electrode, glucose electrode, polyphenol biosensor, sol-gel technique, enzyme immobilisation*

1. Introduction

The method of sol-gel entrapment of biomolecules is a very promising technique of immobilisation for biosensors construction, because of its simplicity, low temperature of the process, large amount and low leakage of entrapped material. Since 1990, when Braun et al. [1] reported for the first time entrapment of proteins in silica gel, the sol-gel process has become an attractive way of immobilisation of biological material in biosensor construction and has been reviewed few times [2–4].

*The paper presented at the International Conference on Sol-Gel Materials, SGM 2001, Rokosowo, Poland.

Sol-gel technique provides a simple method to obtain glass materials by hydrolysis (acidic or basic) and condensation of metal alkoxides. Typically, the gels are obtained from tetramethoxysilane [5] or tetraethoxysilane [6–8]. After hydrolysis (typically acid catalysed) the gel is obtained by changing the pH. Other precursors and gels are also used like alumina [9] or vanadia [10]. For the purpose of the immobilisation of biomolecules, the conditions of precursor hydrolysis and condensation like pH and organic solvent content have to be controlled to avoid denaturation of proteins. When the sol-gel technique is used to construct the optical biosensors, the conditions of the process must allow obtaining transparent gels. The properties of silica gels can be modified by hydrolysis and condensation of organosilicon derivatives like 3-aminopropyltriethoxysilane, 3-glycidoxypropyltrimethoxysilane, 2-(3,4-epoxycyclohexyl)-ethyltrimethoxysilane [11, 12] or others. The resulting gel has better structure, porosity and regular distribution of immobilised biomaterial as compared with conventional one [12]. The use of organosilicon derivatives allows also incorporating ionogenic or redox-active groups into the gel structure [3]. Very promising composite materials for biosensor construction can be obtained by mixing silica sol with redox polymers [13], colloidal gold or graphite powder [3]. Such composites have good electrical properties [3] and can be used for screen-printing approach [14].

The sol-gel technique has been applied in construction of biosensors of different types: conductometric [5], amperometric [6, 8–14], spectrophotometric [6, 8] and fluorometric [7]. A simple enzyme electrode can be obtained by immobilisation of oxidase on the surface of oxygen electrode. The oxygen concentration depletion is proportional to the concentration of oxidase substrate. Local changes of oxygen concentration caused by enzymatic reaction are measured by oxygen electrode. Only once sol-gel process was used by Tatsu et al. to immobilise glucose oxidase on the tip of Clark oxygen electrode and the resulting biosensor was used in flow injection analyser [15].

In this work, the preliminary results of immobilisation of selected enzymes in silica gel obtained by sol-gel process on an oxygen electrode are reported. The aim of this work was to optimise the conditions of immobilisation of the model enzyme (glucose oxidase) in silica hydro gel on the oxygen electrode, to evaluate some of the properties of the obtained glucose electrode and to check the applicability of the sol-gel process to immobilisation of other enzymes.

2. Experimental

2.1. Reagents

As gel precursors tetramethoxysilane (TMOS) (99+%, Aldrich Chemie GmbH, Germany) or tetraethoxysilane (TEOS) (99+%, Aldrich Chemie GmbH, Germany) were used. To some gels 3-aminopropyltriethoxysilane (APTES) (Merck, Germany) was added. As the model enzyme glucose oxidase (GOD) from *Aspergillus niger* (solution, 5370 U/ml, Serva) was used. Other enzymes used in experiments were: catalase

from bovine liver (solution, 155 000 U/ml, Serva), invertase from bakers yeast (solid, 500 U/mg, Sigma), β -galactosidase (lactase) from *Escherichia coli* (solid, 388 U/mg, Sigma), β -galactosidase (lactase) from *Aspergillus oryzae* (solid, 3.8 U/mg, Sigma), α -glucosidase (maltase) from bakers yeast (solid, 3.5 U/mg, Sigma), β -glucosidase from almonds (solid, 6.6 U/mg, Sigma), mutarotase from porcine kidney (suspension, 25000 U/ml, Sigma), ascorbate oxidase from cucurbita species (solid, 146 U/mg, Sigma), phenolase from potato (solid, 570 U/mg, Sigma), laccase from *Rhus vernicifera* (solid, 180 U/mg, Sigma), tyrosinase from mushroom (solid, 3 000 U/mg, Sigma), alcohol oxidase from *Candida boidinii* (solid, 0.4 U/mg, Sigma), galactose oxidase from *Dactylium dendroides* (solid, 16 U/mg, Sigma), choline oxidase from *Alcaligenes* species (solid, 14 U/mg, Sigma), cholinesterase, butyryl (pseudocholinesterase) from horse serum (solid, 8.7 U/mg, Sigma). The enzymes were used with no further purification; if solid they were dissolved in 0.05 M phosphate buffer, pH 6. All other reagents were of analytical grade. Double-distilled water was used throughout. At pH 5.5 and lower 0.05 M acetate buffers were used, for higher pH 0.05 M phosphate ones were used.

2.2. Apparatus

The measurements of dissolved oxygen were done using galvanic silver-zinc oxygen electrode CTN-920.S (MES-EKO, Wrocław, Poland). This electrode consists of silver cathode and zinc anode and is covered by Teflon® membrane. The operating principle of this electrode is the same as the Clark one [16]. The electrode was connected with microcomputer oxygen meter CO-551 (Elmetron, Zabrze, Poland). The oxygen meter measures the current caused by reduction of oxygen on silver cathode after diffusion through the membrane. The results of measurements are expressed as the percentage of oxygen concentration in saturated solution from air at given conditions (pressure and temperature).

The temperature was maintained by the thermostat U1 (MLW, Medingen, Germany). The constant stirring rate of the solution was maintained by magnetic stirrer BMM 21 (DHN Wigo, Piastów, Poland).

2.3. Immobilisation of the enzymes and electrode preparation

The stock solutions of sol were prepared as follows: SOL I – 4.5 ml TEOS, 1.4 ml H₂O and 0.1 ml 0.1 M HCl [6]; SOL II – 5 ml of TMOS, 1.0 ml H₂O and 0.05 ml 0.1 M HCl [5] were stirred vigorously at room temperature until the transparent homogeneous solution was obtained (SOL I – 3 h, SOL II – 15 min) and stored in refrigerator. SOL I was stable for 1 week, SOL II – for 6 weeks.

The casting solution was prepared by mixing 200 μ l of the sol solution with enzyme solution and buffer of pH ranging from 5 to 9 (the total volume of enzyme and buffer ranging from 200 to 800 μ l). 20 μ l of this mixture was dropped immediately

after mixing on the surface of oxygen electrode covered with nylon mesh. The mesh was fixed on the electrode by rubber O-ring and was used as a mechanical holder of gel layer [15] because of the poor adhesion to the Teflon® membrane of oxygen electrode. To some casting solutions APTES was added to check if the introduction of amine groups would change the properties of the resulting enzyme electrode. The compositions of casting solutions and gelation times are given in Table 1. The reported gelation time is the time from mixing sol with buffer containing dissolved enzyme to the moment at which bulk gelation occurs. When the gel was formed, the resulted enzyme electrode was dipped in 100 ml of phosphate buffer, pH 7, at 25 °C.

Table 1. Dependence of gelling time on composition

Sol	pH of the buffer	Sol:buffer ratio	Volume of added APTES	Gelling time/min	
TMOS	5	1: 1	none	3	
	6			4	
	7			1	
	8			0.5	
	9			0.25	
	5	1: 4	none	70	
	6			30	
	7			1.5	
	8			8	
	9			7	
	6	1: 1	2.5 µl	> 0.1	
	TEOS	5	1: 1	none	9
		6			17
		7			4
8		1.5			
9		1			
7		1: 1.5	none	2.5	
		1: 2		3	
		1: 3		3	
5		1: 4	none	30	
6				40	
7				4	
8				1.5	
9				2	
6		1: 1	2.5 µl	1	
	5 µl		0.5		
	10 µl		0.5		
	20 µl		0.5		
7	1: 1	5 µl	0.5		

2.4. Measurement procedure

The measurement procedure was similar to that reported earlier [17]. The response of the electrode was measured using oxygen meter and expressed as per cent of oxygen concentration at saturation from air [18].

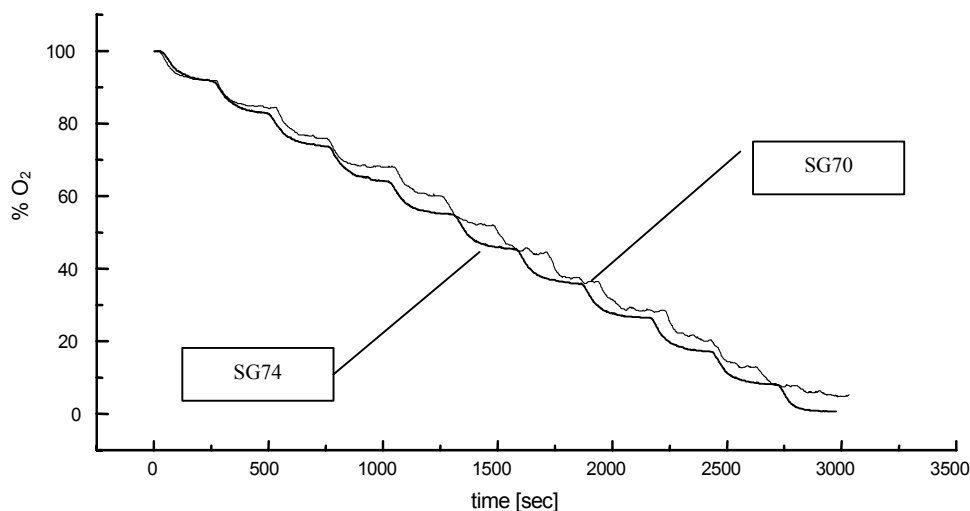


Fig. 1. Examples of response of glucose electrodes: SG70 – 200 μl ZOL I + 180 μl buffer, pH 7 + 20 μl GOD, SG74 – 200 μl ZOL I + 750 μl buffer, pH 7 + 50 μl GOD

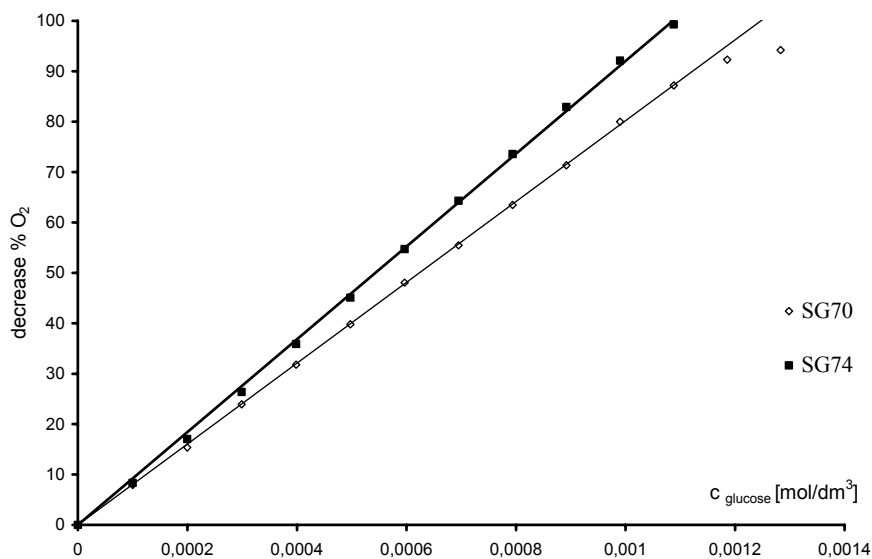


Fig. 2. Examples of the calibration curves of glucose electrode: SG70 – 200 μl ZOL I + 180 μl buffer, pH 7 + 20 μl GOD, SG74 – 200 μl ZOL I + 750 μl buffer, pH 7 + 50 μl GOD

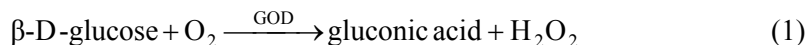
The measurements were done in phosphate buffer, pH 7, at 25 °C in stirred solution (stirring rate 500 rpm). When the electrode response become stable, 0.1 ml of 0.1 M substrate solution (if not stated otherwise) was added.

The solutions of saccharides in water (glucose, galactose, lactose, maltose, saccharose, cellobiose) were made one day before use to allow the mutarotation. All other substrate solutions were made freshly every day. Subsequent addition of substrate was made when the response was time independent. A typical response of glucose electrode is given in Fig. 1. As the result, the calibration curves were obtained (the dependence of decrease of O₂ percentage against concentration of substrate) and the slopes of their linear part (sensitivity) were calculated [19]. The examples of calibration curve are given in Fig. 2.

3. Results

3.1. Glucose electrode

As a model enzyme glucose oxidase was used because of its high activity, selectivity, stability and very well known properties. This enzyme catalyses the reaction:



The depletion of oxygen concentration is thus the measure of glucose concentration.

In preliminary investigations, the response of glucose electrode and its sensitivity was measured for gels prepared from different precursors, with different pH of the buffer and different sol to buffer ratio. For some compositions of the casting solution, also the influence of APTES addition was tested. The details of tested compositions are given in Table 1. The casting solutions with gelation times longer than 30 min and shorter than 0.25 min cannot be used to prepare the glucose electrode because of technical problems. For very long gelation times the sol, when dropped onto the tip of the electrode, was drying before the gel was formed and the resulting layer was cracking. For very short times, it is impossible to take the desired volume from the casting solution and drop it on the electrode because the gel is formed in the pipette. When TMOS was used as a precursor, some precipitation of silica could be observed for sol to buffer ratio 1:4 before gelation, when sol and buffer were mixed together. The less pH of the buffer, the more silica was precipitated.

For some tested compositions of the casting solution the response of the electrode is not stable but varies about some value (“noisy” response) – for example the line SG70 in Fig. 1. The electrodes with noisy response are not suitable to measure the glucose content in solution. Probably, such unstable response is caused by the poor adhesion of gel layer to Teflon® membrane. The adhesion could be improved by addi-

tion of surfactant to the casting solution [20]. Thus, to some casting solutions, surfactant Triton X-100 was added but no improvement of the electrode response was observed.

The typical calibration curves for glucose were linear with some deviations from linearity for higher concentrations of glucose (Fig. 2) caused by the lack of oxygen in diffusion layer near the electrode surface. The reciprocal plots (not shown) of the data indicate that the response of electrode is controlled by diffusion of substrates to electrode surface [21]. In Table 2, analytical properties of glucose electrodes are summarised.

Table 2. Analytical parameters of glucose electrodes with stable response

Sol	Buffer pH	Sol:buffer ratio	Volume of added APTES	Linear range /mol/dm ³	Sensitivity /% of O ₂ /(mol·dm ⁻³)	<i>r</i>
TMOS	7	1: 4	none	0–0.0011	79220	0.999
	8			0–0.0007	64520	0.997
	9			0–0.0009	102960	0.999
TEOS	5	1: 1	none	0–0.0008	88330	0.998
	6			0–0.0011	86190	0.999
	7	1: 1.5 1: 2 1: 3	none	0–0.001	95080	0.999
				0–0.001	86020	0.997
				0–0.001	87000	0.999
	5	1: 4	none	0–0.001	92760	0.999
	6			0–0.001	90880	0.999
	7			0–0.001	92260	0.999
	8			0–0.0009	99840	0.999
	9			0–0.001	100110	0.999
6	1: 1	2.5 µl 5 µl	0–0.0009	103500	0.997	
			0–0.001	86440	0.999	

A typical response time of the electrodes (time interval from addition of substrate until the signal become stable) varies from 3 to 5 min with some tendency to be lower for higher water content in gel.

The results of investigations of the influence of the composition of the casting solution on gelling time and glucose electrode response indicate that TEOS is better gel precursor than TMOS, because for the latter the response of the electrodes is noisy and there are some problems with gel formation (precipitation of silica for high buffer to sol ratio). For TEOS better electrodes with higher sensitivity are obtained with high buffer to sol ratio (Table 2, Fig. 3) especially for basic pH. A lower response of electrodes with low sol to buffer ratio is probably caused by greater diffusional resistance of the gel, which is denser in this case [21]. The addition of APTES caused the shortening of the gelation time but does not improve the properties of the electrodes. In

contrary, when the high amount of APTES is added, the response of the electrode becomes unstable.

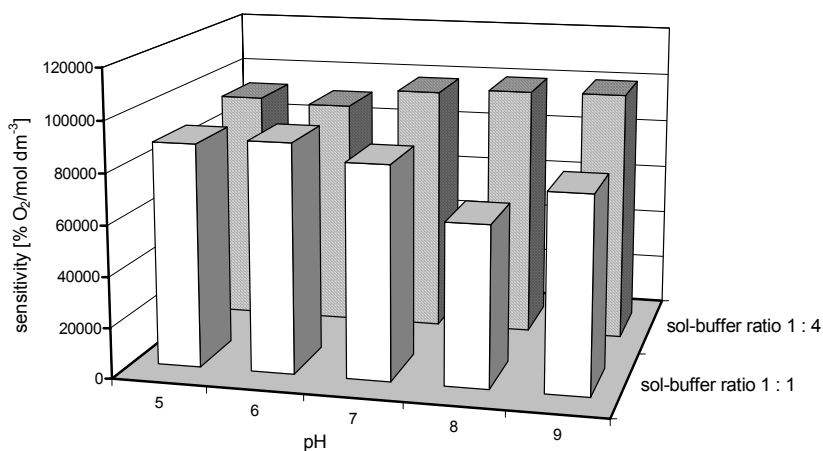


Fig. 3. The glucose electrode sensitivity for different compositions of casting solution (sol precursor TEOS)

For further experiments with glucose oxidase the gels of following composition were chosen: SG60 – buffer pH 6, sol to buffer ratio 1:1, SG61 – buffer pH 6, sol to buffer ratio 1:1 + 5 μ l APTES added, SG74 buffer pH 7, sol to buffer ratio 1:4. For these gels, the dependence of electrode response on pH (Fig. 4) and temperature (Fig. 5) was investigated. For all gels tested, the response of the electrode shows the maximum at pH = 7, with sharp loss of the sensitivity for greater values. Similar results were obtained by other authors [23]. With increasing temperature the measured signal of the electrode (decrease of oxygen concentration) is growing up to about 35 °C; for the temperatures higher than 30 °C, the calibration curves become non-linear and because of that the maximum response is obtained for different temperatures for low and high glucose concentration (Fig. 5). The glucose oxidase is known as a very stable enzyme [24], but the results obtained indicate that in silica environment its stability is poor. Also, the stability of the electrodes was tested. For this purpose, they were stored for 10 days in 50 ml of buffer, pH 7, in refrigerator (4 °C). After this storage, the response of electrodes decreases (for SG60 only 7.7% of the initial sensitivity) and unstable. Similar results for GOD immobilised in silica gel were obtained by other authors [23]. In storage buffer, the traces of GOD activity could be found. The results indicate that there is leakage of enzyme from the gel. Also the gel by itself is not stable and some cracking could be observed.

Glucose oxidase was co-immobilised with catalase to broaden the calibration range of the electrode. The upper limit of glucose concentration that can be assayed by glucose electrode is limited by the solubility of oxygen in solution. By addition of

catalase the upper limit could be extended twice, because half of the consumed oxygen (Eq. (1)) is in a half recovered in reaction:

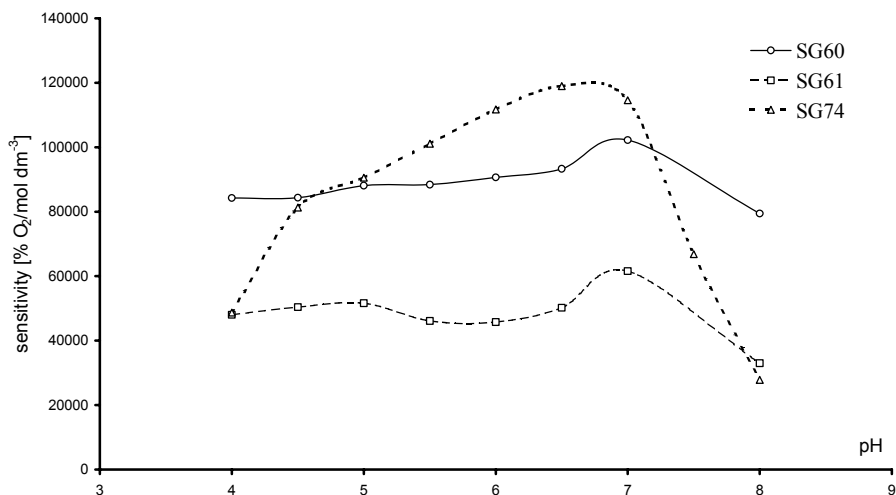
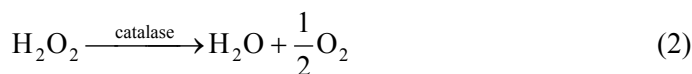


Fig. 4. The dependence of glucose electrode sensitivity on pH (description of legend key in text)

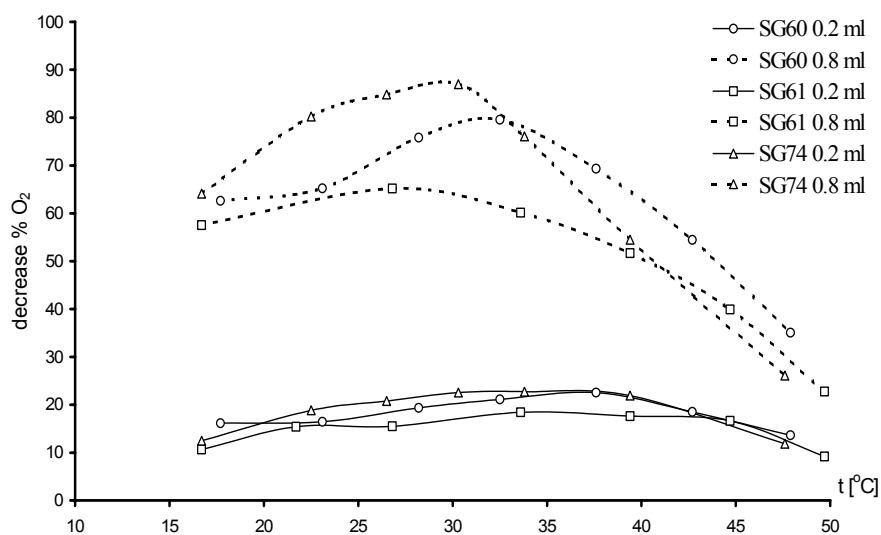


Fig. 5. The dependence of glucose electrode response on temperature for 0.2 ml and 0.8 ml of added 0.1 M glucose solution (description of legend key in text)

To casting solutions SG60 and SG74 catalase was added and the ratio of activities, catalase to GOD was 14.4:1. As the result, the linear parts of the calibration curves were extended to 0.0017 mol/dm^3 for SG60 and 0.0013 mol/dm^3 for SG74. The sensitivity decreased by the factor of 0.5 for SG60 and 0.6 for SG74.

3.2. Electrodes for disaccharides

By co-immobilisation of GOD with suitable hydrolases (and mutarotase optionally) the electrodes sensitive for disaccharides (maltose, lactose, saccharose and cellobiose) could be obtained. The hydrolase hydrolysis disaccharide to glucose and other monosaccharide in reactions:

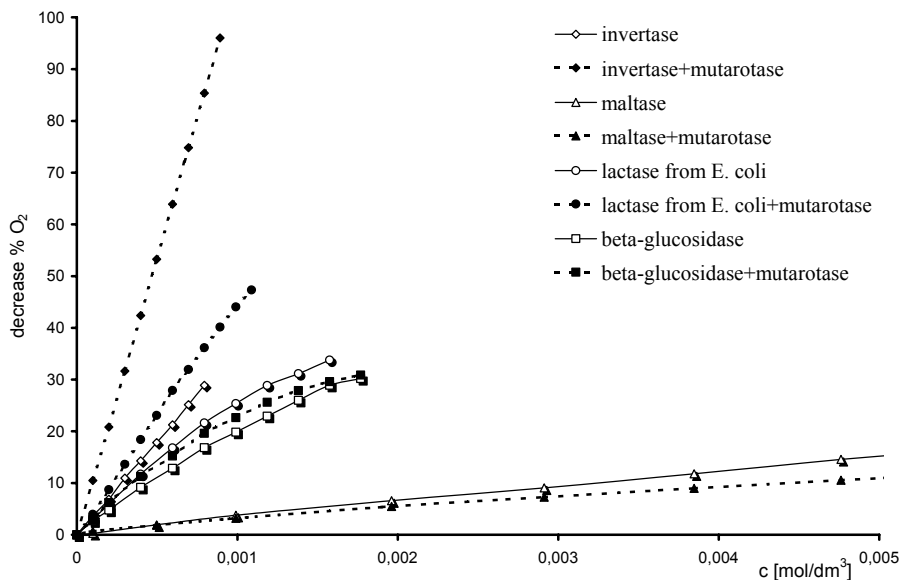
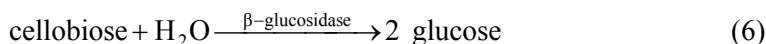
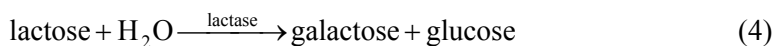
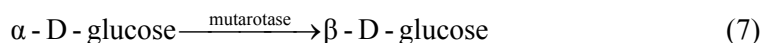


Fig. 6. Examples of calibration curves for disaccharides with casting solution composition SG74 (details about added activities of enzymes in Table 3) at pH 7

Glucose produced in reactions (3)–(6) is then consumed by GOD. Because GOD oxidases only β -D-glucose and during hydrolysis of some disaccharides (e.g., saccha-

rose, maltose) α -D-glucose is produced, mutarotase is added [18]. Mutarotase increases the rate of reaction of mutarotation of glucose:



and thus, the response of the electrode for disaccharide is increasing.

For hydrolases (not for all) only casting solutions SG60 and SG74 were tested (not for all enzymes, Table 3), because the addition of APTES (SG61) does not change the properties of electrode significantly. Typically, the slopes of the calibration curves were less for sol to buffer ratio 1:1 or in the case of maltase, there was no response. The reason is that the gel is denser and denaturation of the enzymes during the gelling process occurs by high concentration of ethanol, which is produced during hydrolysis of TEOS. Some results (calibration curves) for different disaccharides are presented in Fig. 6 and some analytical parameters are collected in Table 3.

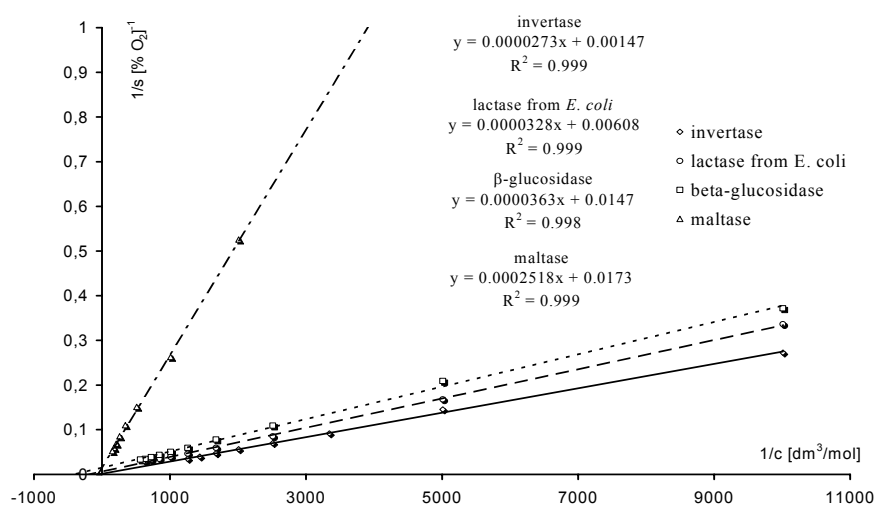


Fig. 7. The double reciprocal plots for electrodes with disaccharide hydrolases without added mutarotase (data from Fig. 6)

Except of maltase, the improvement of the electrode response by addition of mutarotase could be seen especially for invertase and lactase from *Escherichia coli*. For lactase from *Aspergillus oryzae* this effect was not observed but for this enzyme the calibration was made at pH very different from its optimum pH, which is 4.5 and due to that its activity was low. Also, some results reported for electrodes with β -galactosidase applied in flow injection analysis indicate that the addition of mutarotase did not improve the characteristics of the electrode [25]. The calibration curves for disaccharides are not linear. The double reciprocal plot of the data (Fig. 7) indicates that the electrode response is controlled by the kinetics of the enzymatic reaction [21]. From

these plots, the apparent Michaelis constants for enzymes could be calculated using Lineweaver–Burk equation [22]. They are 18.6, 5.39, 2.47 and 16.6 mM for invertase, lactase from *Escherichia coli*, β -glucosidase and maltase, respectively.

Table 3. Analytical parameters of electrodes for disaccharides at pH 7

Composition	Enzyme *	Activity/U**	Substrate	Sensitivity /% of O ₂ /mol·dm ⁻³	Linear range /mol/dm ³	r
SG60	invertase	50	saccharose	50346	0–0.0005	0.999
	invertase + mutarotase	50 + 12.5		61676	0–0.001	0.999
SG74	invertase	50		36074	0–0.0008	0.999
	invertase + mutarotase	50 + 12.5		107308	0–0.0009	0.999
SG60	maltase	4	maltose	no response		
	maltase + mutarotase	4 + 12.5				
SG74	maltase	4		3017	0–0.007	0.998
	maltase + mutarotase	4 + 12.5		2369	0–0.005	0.987
SG74	lactase from <i>E. coli</i>	13.5	lactose ***	27907	0–0.0008	0.999
	lactase from <i>E. coli</i> + mutarotase	13.5 + 1.5		45381	0–0.001	0.999
SG74	lactase from <i>A. Oryzae</i>	1.9	lactose ***	22836	0–0.0008	0.999
	lactase from <i>A. Oryzae</i> + mutarotase	1.9 + 12.5		21981	0–0.0008	0.999
SG74	β -glucosidase	2.64	cellobiose ***	21686	0–0.0008	0.998
	β -glucosidase + mutarotase	2.64 + 12.5		25687	0–0.0008	0.995

*In each case the activity of added GOD was 5.4 U per electrode.

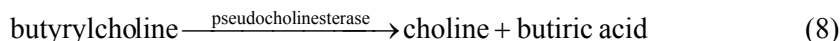
**Activity of enzyme immobilised on electrode.

***For this saccharides the compositions SG60 was not tested.

The sensitivities of the tested electrodes sensitive for disaccharides except that for saccharose are too low to find the practical application for assay of disaccharides. But the improvement of their properties could be achieved by increasing the amount of added hydrolase and assay at optimal pH.

3.3. Electrodes with other oxidases

The enzymes tested were: galactose oxidase, ascorbate oxidase, alcohol oxidase, three types of polyphenolase (laccase, tyrosinase from mushroom and phenolase from potato) and choline oxidase. Choline oxidase was also co-immobilised with pseudo-cholinesterase (Fig. 10) to assay choline esters due to the course of reactions:



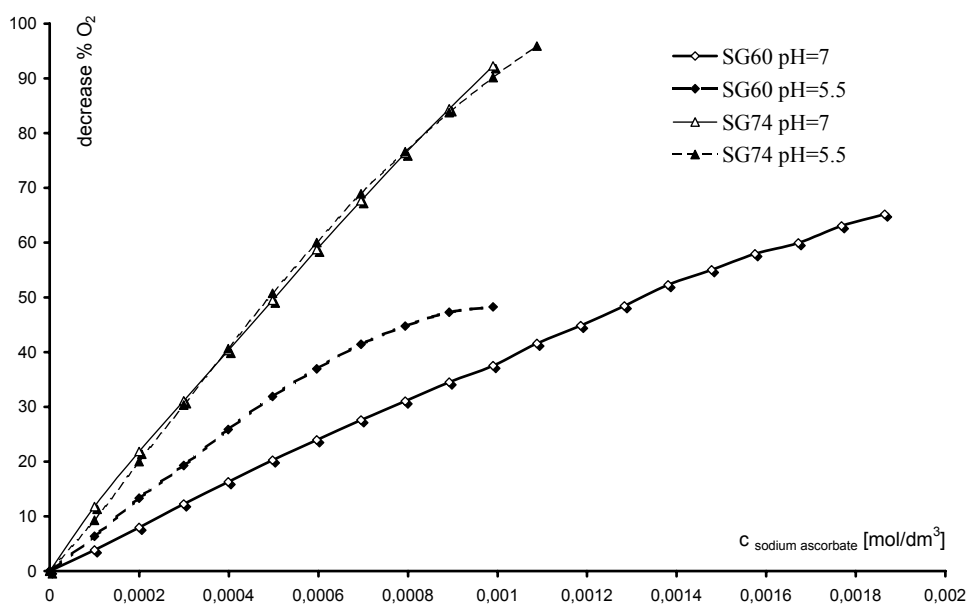


Fig. 8. Calibration curves of electrode with ascorbate oxidase for vitamin C

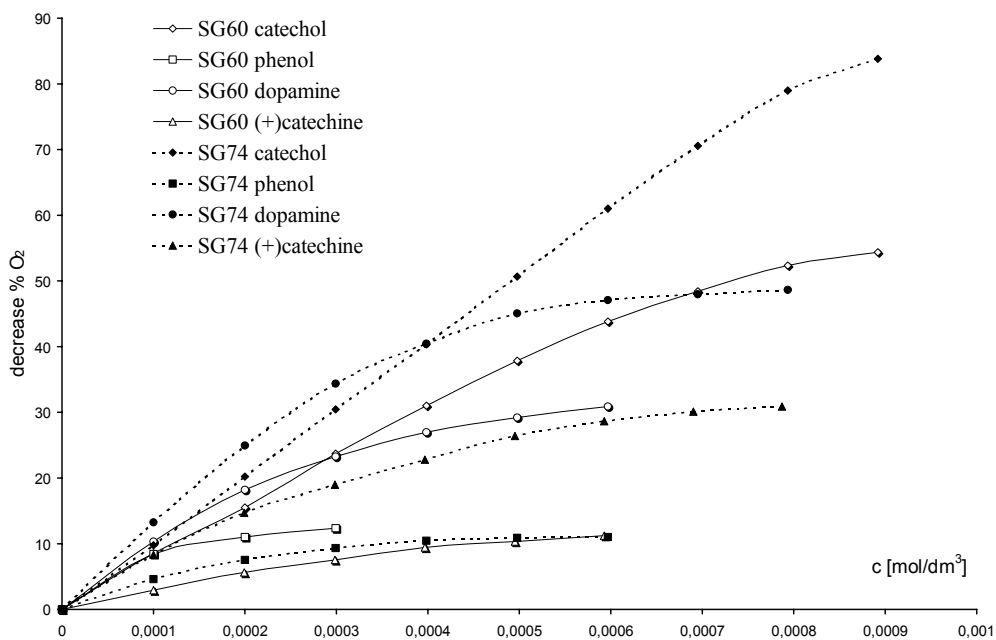


Fig. 9. Calibration curves of electrode with tyrosinase for different substrates at pH 7 (4U of enzyme immobilised on electrode)

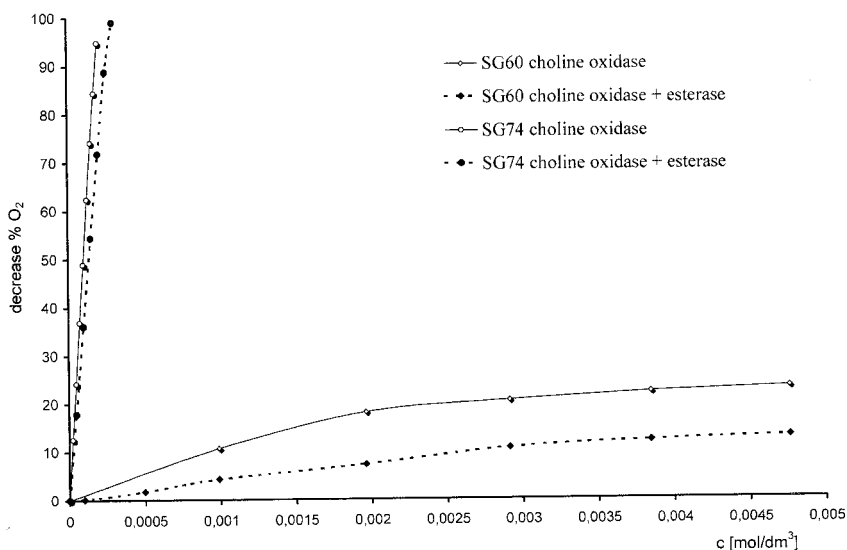


Fig. 10. Calibration curves of electrodes with choline oxidase without and with added pseudocholinesterase at pH 7

Such an electrode is very promising for indirect monitoring of pesticides, which inhibit catalytic properties of esterase [26]. For all enzymes except alcohol oxidase, the compositions of casting solutions tested were SG60 and SG74. Some examples of the calibration curves are shown in Figs. 8–10, and analytical parameters of calibration curves are collected in Table 4.

For all enzymes, the measured electrode signal was greater for sol to buffer ratio 1:4. The electrode with galactose oxidase was tested also for lactose because this enzyme can oxidise not only free galactose, but also galactosides but with lower rate. For some enzymes, the precipitation of the protein could be observed during formation of gel with sol to buffer ratio 1:1 causing a very low electrode signal or even none. It is especially characteristic of choline oxidase and esterase. The ratio of sensitivities for sol SG74 and SG60 is 51.5 and 96.8 for choline oxidase and co-immobilised choline oxidase and esterase, respectively (Fig. 10). The reason is that in sol SG60 the concentration of ethanol is much higher as compared with SG74. It could be also seen that for the same enzyme the response for the substrate with greater molecule is much lower for the denser gel (compare the results with tyrosinase for catechol and (+)catechine, Fig. 9). For sol composition SG60, the ratio of sensitivities for (+)catechine and catechol is 0.34 and for SG74 0.74. It is caused by greater diffusional resistivity of denser gel.

For all oxidases tested, the calibration curves are not linear and their linear ranges are sometimes very narrow. The reason of such non-linearity is that the response of the electrode is controlled by the kinetics of enzyme reaction not by the diffusion of the substrate and oxygen [21]. For some enzymes, there is also another reason of non-

linearity. Polyphenolases, especially tyrosinase, and ascorbate oxidase belong to the group of the enzymes that undergo suicide inactivation by the substrates [27, 28]. The higher is the concentration of the substrate and the longer is the time of enzyme contact with it the lower is the activity of the enzyme. This effect is especially significant for tyrosinase and ortodiphenols. It causes that during prolonged time of measurements and for higher concentrations of substrate, the measured signal of the enzyme electrode with immobilised tyrosinase begun to increase instead decrease after addition of substrate [29, 30]. This was observed for all polyphenolases tested and for ascorbate oxidase at pH 5.5.

Table 4. Analytical parameters of some electrodes with immobilised oxidases

Composition	Enzyme	Activity /U*	Substrate	pH	Linear range /mol/dm ³	Sensitivity /% of O ₂ /mol·dm ⁻³	r		
SG60	Galactose oxidase	2.5	galactose	7	0–0.0012	5615	0.997		
			lactose	6	0–0.005	1144	0.953		
SG74			galactose	7	0–0.004	16745	0.994		
			lactose	6	0–0.006	791	0.998		
SG74	alcohol oxidase	0.2	ethanol	7	0–0.0016	11880	0.985		
			ethanol	7	0–0.0004	42810	0.976		
SG60	ascorbate oxidase	4	sodium ascorbate	7	0–0.0014	38363	0.999		
				5,5	0–0.0006	63568	0.999		
SG74				7	0–0.0007	99356	0.998		
				5,5	0–0.0007	100051	0.999		
SG60	choline oxidase	2	choline	7	0–0.002	9530	0.994		
SG74				7	0–0.000175	490562	0.999		
SG60	choline oxidase + pseudo-cholinesterase	2 + 6	butyryl choline chloride	7	0–0.003	3704	0.998		
SG74				7	0–0.00025	358494	0.999		
SG60	tyrosinase	1.6	catechol	7	0–0.0003	69275	0.996		
				4	catechol	7	0–0.0004	78457	0.999
					dopamine	7	0–0.0002	93830	0.997
					(+)catechine	7	0–0.0002	26373	0.996
SG74	4	catechol	7	0–0.0007	101755	0.999			
			dopamine	7	0–0.0002	126361	0.999		
			(+)catechine	7	0–0.0003	75739	0.997		
SG74	phenolase	4	catechol	7	0–0.0004	39218	0.989		
SG74	laccase	4	catechol	7	0–0.002	15674	0.979		

*Activity of enzyme immobilised on electrode.

To diminish the effect of suicide inactivation the activity of immobilised tyrosinase must be very high. For sol composition SG60 the effect of inactivation by catechol was observed at concentration 0.5 mM when 1.6 U of tyrosinase is immobilised and at

0.9 mM for 4U. Also the sensitivity of the electrode is in first case lower and linear range is narrower.

The presented results for oxidases are only preliminary and are continued especially for tyrosinase.

4. Conclusions

- The technique of immobilisation by sol-gel transition on the tip of oxygen electrode can be applied to different enzymes to obtain enzyme electrodes.
- The ratio of water to sol during gel formation must be high to avoid the denaturation of the enzyme by ethanol during immobilisation, to diminish the diffusional resistance of the gel layer and thus, to obtain electrodes with high sensitivity.
- The addition of APTES does not improve significantly the properties of the electrodes.
- The glucose oxidase entrapped in silica hydrogel is rather unstable and some leakage of the enzyme during storage is observed. The stability could be improved either by crosslinking the protein with for example glutaraldehyde or covering the gel with outer membrane.
- The calibration curves are not linear. The non-linearity is caused by different reasons depending on the enzyme type and immobilised amount of the enzyme.

The investigations of enzyme electrodes with enzymes immobilised by sol-gel technique will be continued especially for tyrosinase. The aim of the further work is to optimise the composition of the casting solution for this particular enzyme to improve stability and avoid inactivation by the substrate, to check the operation parameters of the resulted electrode, influence of pH and temperature and selectivity spectrum.

Acknowledgement

The author is grateful to the Committee for Scientific Research (KBN) for a financial support through grant No. 7 T08E 008 16.

References

- [1] BRAUN S., RAPPOPORT S., ZUSMAN R., AVNIR D., OTTOLENGHI M., *Mater. Lett.*, 10 (1990), 1.
- [2] DAVE B.C., DUNN B., VALENTINE J.S., ZINK J.I., *Anal. Chem.*, 66 (1994), 1120 A.
- [3] WANG J., *Anal. Chim. Acta*, 399 (1999), 21.
- [4] LIN J., BROWN C.W., *Trends Anal. Chem.*, 16 (1997) 200.
- [5] LEE W.-Y., KIM S.-R., KIM T.-H., LEE K.S., SHIN M.-C., PARK J.-K., *Anal. Chim. Acta*, 404 (2000), 195.

- [6] NARANG U., PRASAD P.N., BRIGHT F.V., RAMANATHAN K., KUMAR N.D., MALHOTRA B.D., KAMALA-SANAN M.N., CHANDRA S., *Anal. Chem.*, 66 (1994), 3139.
- [7] WU X., CHOI M.M.F., XIAO D., *Analyst*, 125 (2000), 157.
- [8] KUMAR A., MALHOTRA R., MALHOTRA B.D., GROVER S.K., *Anal. Chim. Acta*, 414 (2000), 43.
- [9] LIU Z., LIU B., KONG J., DENG J., *Anal. Chim. Acta*, 392 (1999), 135.
- [10] LEV O., GLEZER V., *J. Am. Chem. Soc.*, 115 (1993), 2533.
- [11] PANDLEY P.C., UPADHYAY S., PATHAK H.C., *Electroanalysis*, 11 (1999), 59.
- [12] PANDLEY P.C., UPADHYAY S., PATHAK H.C., *Sens. Actuators B*, 60 (1999), 83.
- [13] PARK T.-M., IWUOHA E.I., SMYTH M.R., FREANEY R., MCSHANE A.J., *Talanta*, 44 (1997), 973.
- [14] WANG J., PAMIDI P.V.A., PARK D.S., *Anal. Chem.*, 68 (1996), 2705.
- [15] TATSU Y., YAMASHITA K., YAMAGUCHI M., YAMAMURA M., YAMAMOTO H., YOSHIKAWA S., *Chem. Lett.*, (1992), 1615.
- [16] Lee Y.H., Tsao G.T., [in:] *Advances in Biochemical Engineering*, T.K. Ghose (Ed.), A. Fiechter & N. Blakenbrough, Springer, Berlin, 1979 Vol. 13, 34–86.
- [17] Przybył M., Sugier H., *Anal. Chem. (Warsaw)*, 34 (1989), 63.
- [18] Filipiak M., Fludra K., Gościńska E., *Biosens. Bioelectr.*, 11 (1996), 355.
- [19] THÉVENOT D.R., TOTH K., DURST R.A., WILSON G.S., *Biosens. Bioelectr.*, 16 (2001) 121.
- [20] LEV O., *Analisis*, 20 (1992), 543.
- [21] SCHELLER F., SCHUBERT F., *Biosensors*, Elsevier, Amsterdam, 1992, p. 55.
- [22] LI J., CHIA L.S., GOH N.K., TAN S.N., *Anal. Chim. Acta*, 362 (1998) 203.
- [23] YAO T., TAKASHIMA K., *Biosens. Bioelectr.*, 13 (1998), 67.
- [24] WILSON R., TURNER A.P.F., *Biosens. Bioelectr.*, 7 (1992), 165.
- [25] NARINESINGH D., STOUTE V.A., DAVIS G., NGO T.T., *Analyt. Biochem.*, 194 (1991) 16.
- [26] BERNABEI M., CHIAVARINI S., CREMISINI C., PALLESCHI G., *Biosens. Bioelectr.*, 8 (1993), 265.
- [27] CÉNOVAS F.G., TUDELA J., MADRID C.M., VARÈN R., CARMONA F.G., LOZANO J.A., *Biochim. Biophys. Acta*, 912 (1987), 417.
- [28] TOKUYAMA K., DAWSON C.R., *Biochim. Biophys. Acta*, 56 (1962), 427.
- [29] ZHANG J., LI B., XU G., CHENG G., DONG S., *Analyst*, 124 (1999), 699.
- [30] RIVAS G.A., SOLIS V.M., *Electroanalysis*, 6 (1994), 1136.

Received 16 June 2001
Revised 19 December 2001

Bi-doping effect on the Jahn–Teller phase transition in CsDy(MoO₄)₂ crystal

¹S.S. GERASHCHENKO, ¹O.V. MILOSLAVSKAYA, ¹YU.N. KHARCHENKO,
¹V.I. KUTKO, ¹N.M. NESTERENKO, ²L. MACALIK, ²K. HERMANOWICZ,
²M. MACZKA, ^{2,3}J. HANUZA

¹B. Verkin Institute for Low Temperature Physics & Engineering NAScU, 61164,
47 Lenin Ave., Kharkiv, Ukraine

²Institute of Low Temperature and Structure Research, Polish Academy of Sciences,
2 Okólna St., 50-950 Wrocław, Poland

³Department of Bioorganic Chemistry, Faculty of Engineering and Economics,
University of Economics, 53-345 Wrocław, 118/120 Komandorska str., Poland,

Using spectroscopic and visual optical methods the shift of the critical temperature ($T_{tr} \approx 42$ K) of the first-order phase transition of the Jahn–Teller type to the low-temperature side at doping the CsDy(MoO₄)₂ crystal with Bi³⁺ (concentration up to $x \approx 0.08$) was revealed. Effect of the doping is compared to the effect of uniaxial pressure. Using the result of the Zeeman effect we have calculated the critical value H_c of external magnetic field at which the spontaneous change of the sizes of crystal is suppressed under magnetic field and the high-temperature phase may be induced at $T = 0$ K. It is supposed that doping with Bi³⁺ leads to decrease of the critical magnetic field value for doped CsDy(MoO₄)₂.

Key words: *bi-doping, Jahn–Teller effect, uniaxial pressure*

1. Introduction

CsBi(MoO₄)₂ and CsDy(MoO₄)₂ crystallise in the D_{2h}^3 crystal structure with two molecules in the unit cell [1, 2]. Both crystals undergo different successions of phase transitions which take place at 325 and 125 K for CsBi(MoO₄)₂ and 50 and 42 K for CsDy(MoO₄)₂ [3–6]. The crystal structures below phase transition temperatures are not known. It was shown earlier that the doping of CsDy(MoO₄)₂ with various rare earth ions (Gd, Eu and others) shifted significantly the critical temperature ($T_{tr} = 42$ K) of the first-order Jahn–Teller type phase transition to the low-temperature side [4, 7, 8]. When Dy³⁺ ions concentration became less than critical [8, 9], the low-

temperature phase was quite different from that found for $\text{CsDy}(\text{MoO}_4)_2$. The investigations of phase transitions of Jahn–Teller type in $\text{CsDy}(\text{MoO}_4)_2$ and in the mixed crystals $\text{CsDy}_{1-x}\text{Bi}_x(\text{MoO}_4)_2$ with bismuth ions substituting dysprosium ones are of principal interest because bismuth is not a rare earth element and its ion radius is essentially different from that of dysprosium. Shift of the first-order type phase transition temperature to the low-temperature side was also observed under the external magnetic field: when magnetic field was oriented along axis a ($H \parallel a$), the transition temperature decreased by 5 K from $H \approx 70$ kOe to 170 kOe [10]. Moreover, a small shift of T_{tr} towards lower temperature under external pressure was observed experimentally [11]. Therefore, the comparison of the pressure, magnetic field and doping effects is of special interest.

2. Experimental

The electronic absorption spectra in the NIR region were used to study the phase diagram (x – T_{tr}) of the $\text{CsDy}_{1-x}\text{Bi}_x(\text{MoO}_4)_2$ crystals. The spectra were recorded in the range of 13 000–13 500 cm^{-1} for which the phase transition is particularly well observed. The measurements of the absorption spectra of $\text{CsDy}(\text{MoO}_4)_2$ and $\text{CsDy}_{1-x}\text{Bi}_x(\text{MoO}_4)_2$ at the external magnetic field $H \parallel a$ in the low-temperature phase at $T = 6.5$ K ($T < T_{tr}$) were performed up to 6 T. The absorption spectra in the 13 000–13 500 cm^{-1} range were recorded with the resolution of 0.5 cm^{-1} using the set-up with double monochromator. For the low-temperature measurements the samples in the form of very thin plates (c.a. 0.6 mm thick) were placed in a cryostat.

The crystals have been grown by the method of crystallization of the solution in melt with bismuth content x in the mixture ranging from 5% to 80%. Solubility of ingredients at crystal growing was not under control. The actual crystal composition was determined with the help of X-Ray dispersion methods based on the scanning electron microscope Philips SEM 515 and microanalyzer EDAX 9800. The phase diagram (x – T_{tr}) was also determined by visual method. Visual detecting of the temperature of the first-order Jahn–Teller phase transition was performed by observations of the typical domain structures forming near T_{tr} [9].

3. Results and discussion

The absorption spectra in the energy region 13 000–13 500 cm^{-1} were obtained at c.a. 42 K ($>T_{tr}$) and at c.a. 6.5 K ($<T_{tr}$) temperatures (Fig. 1). The absorption bands are due to transitions inside f-shells of Dy^{3+} ions from the components of the ground multiplet ${}^6\text{H}_{15/2}$ to the excited ${}^6\text{F}_{3/2}$ state split by low-symmetry crystal field into 8 and 2 components, respectively. The phase transition for the crystal studied occurs at about 42 K. At $T > T_{tr}$ two wide components with the energy interval of approximately

41 cm^{-1} were observed in the spectra. For this phase the low-energy satellite appears due to the transition from the first excited level of ${}^6\text{H}_{15/2}$.

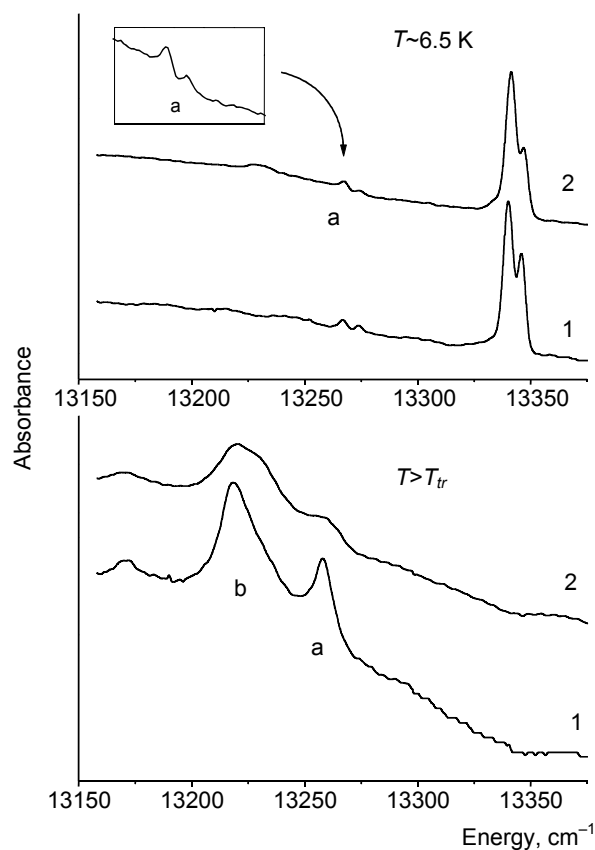


Fig. 1. Absorption spectra of the $\text{CsDy}_{1-x}\text{Bi}_x(\text{MoO}_4)_2$ crystals with $x = 0.01$ (1) and $x = 0.06$ (2) at the temperature higher than T_{tr} and at 6.5 K (transition from ${}^6\text{H}_{15/2}$ to ${}^6\text{F}_{3/2}$)

In Figure 1 one may notice only one doublet band observed at 6.5 K, the energy gap between doublet components is 8 cm^{-1} . The resolved doublet structure of the band was observed owing to the small bandwidth of lines at low temperatures. However, at $T > T_{tr}$ the expected doublet structure of the band is not observed because bandwidths of the lines are too large comparing to the interval between the doublet components.

Similar as for $\text{CsDy}(\text{MoO}_4)_2$ [3], all doped crystals in the low-temperature phase show shifts of the discussed doublet by at least 80 cm^{-1} to the high energy side in comparison with the initial phase at $T > T_{tr}$. This behaviour of the absorption spectra proves that in all crystals of the series the co-operative Jahn–Teller effect results in the

lowering of the ground state by the same value of about 80 cm^{-1} and permits us to use the spectral methods for testing the low-temperature phase.

Additionally, at 6.5 K one can also observe a few other spectral features (see the inset in Fig. 1). This spectrum is inherent for the high temperature phase ($T > T_{tr}$). In this phase the 41 cm^{-1} energy distance between band peaks *a* and *b* corresponds to the distance between ground and the nearest excited levels of the ${}^6\text{H}_{15/2}$ ground multiplet at $T > T_{tr}$.

The real Bi^{3+} content determined by X-Ray methods was quite different from the concentration value in the melt. It appeared that for the crystals with $x = 0.95$ for Dy^{3+} and $x = 0.05$ for Bi^{3+} in the melt, the real Bi^{3+} content in the crystals is $x = 0.03\text{--}0.04$.

For the crystals with the real Bi^{3+} content $x \approx 0.01$ and $x = 0.035$ the transition temperatures were determined visually and were equal to c.a. 36–39 K at cooling and c.a. 34–36 K at heating (see Fig. 2 – centred circles). For the crystals with the highest Bi^{3+} content in the melt the transition temperature is near 26 K. Assuming that the transition temperature depends linearly on x for the crystals with low Bi^{3+} concentrations (dashed line in Fig. 2), one can estimate the real Bi^{3+} content. It may be concluded that in our crystals the Bi^{3+} ion concentration does not exceed $x = 0.08$, i.e. the maximal Bi^{3+} content in crystals is nearly ten times lower than in the melt.

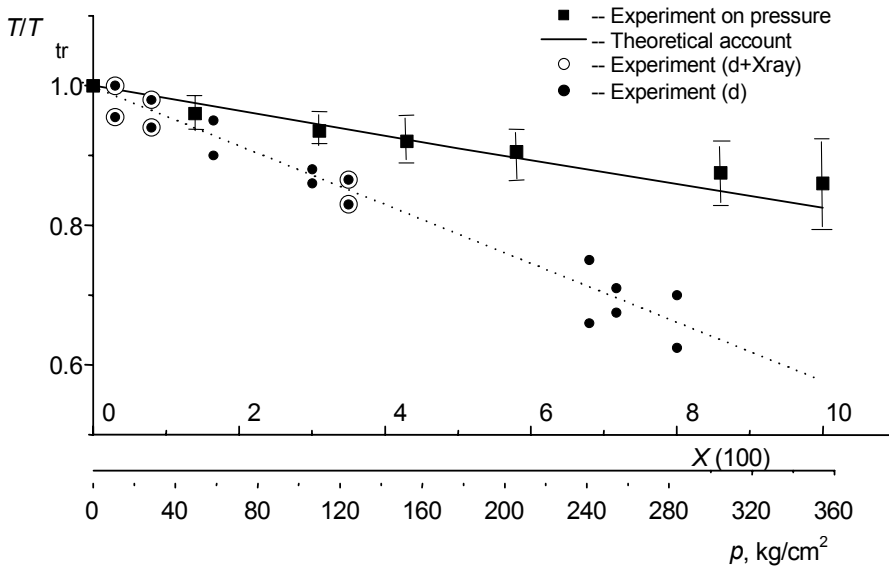


Fig. 2. Dependence of the temperature of phase transition of Jahn–Teller type on concentration in the $\text{CsDy}_{1-x}\text{Bi}_x(\text{MoO}_4)_2$ crystals. The dark squares correspond to the averaged data [11], solid line shows the theoretical estimation, and centred circles correspond to the transition temperatures determined by visual method in the crystals with concentrations taken from X-Ray data. Dashed line goes through these points. The dark circles correspond to the reduced temperature of phase transition, T/T_{tr} . Lower circles (cooling) and higher ones (heating) are shown symmetrically relative to the dashed line

Observation of the domain structure formation allowed us also to conclude that in the mixed crystals the temperature region of coexistence of the initial and low-temperature phases is widened. For some crystals the mixed phase may be observed till temperatures as low as 15 K. This result is confirmed by the absorption spectra investigations (Fig. 1).

Therefore, it was found out that Bi^{3+} doping lowers the temperature of transition without changing the character of transition and also widens the temperature region of coexistence of the initial and low-temperature phases. Besides, the phonon spectra in the mixed crystals as well as electronic spectra does not differ substantially from those in $\text{CsDy}(\text{MoO}_4)_2$. By contrast, an external magnetic field changes the low-energy electronic spectra essentially due to the large g -factor components of g -tensor of the spectroscopic splitting for dysprosium ion ground state. To examine the external magnetic field effect on the electronic spectra we have measured the absorption spectra at magnetic field up to 60 kOe ($H \parallel a$).

The absorption spectra originating from the optical transition ${}^6\text{H}_{15/2} - {}^6\text{F}_{3/2}$ were measured at different values of external magnetic field at 6 K (see Fig. 3). The intensity of the low-frequency component of the absorption band is decreased. This fact results from the decrease of the population of the upper level of the split ground state when magnetic field increases. Therefore, we may conclude that splitting of the absorption band is defined by g -factor of the ground state. A similar behaviour was observed for the absorption band of the “frozen” high-temperature phase in $\text{CsDy}(\text{MoO}_4)_2$ with 0.1% of Bi^{3+} .

Basing on the measured absorption spectra we have constructed the frequency-field dependence of the ${}^6\text{H}_{15/2} - {}^6\text{F}_{3/2}$ optical transition and defined g -factor of the spectroscopic splitting of the ground state for the low- and high-temperature phases. These g -factor values occurred to be $g_1 = 10.8$ and $g_2 = 11.5$ for the low- and high-temperature phase, respectively (Fig. 3).

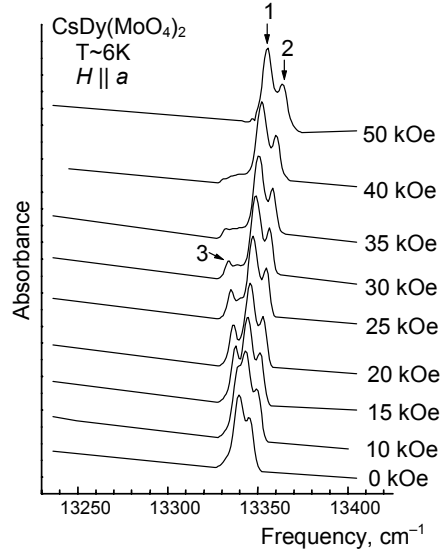


Fig. 3. The bands originating from the optical transition ${}^6H_{15/2} - {}^6F_{3/2}$ in the absorption spectrum of the $\text{CsDy}(\text{MoO}_4)_2$ crystal measured at different magnetic field values (for the low-temperature phase)

We can conclude that magnetic field in the geometry of experiment does not shift the critical temperature but leads only to the splitting of the level, i.e. the value of magnetic field available in our experiment is not high enough to turn the low-temperature phase into the high-temperature one.

At the temperature $T_{tr} \approx 42$ K the $\text{CsDy}(\text{MoO}_4)_2$ crystal undergoes the structural phase transition of the co-operative Jahn–Teller effect type (CJTE) accompanied by significant distortion of the crystal lattice as well as lowering of the ground state of the electron subsystem of Dy^{3+} ions by the value $\Delta E \approx 80 \text{ cm}^{-1}$ [3].

From all results presented it follows that the Jahn–Teller phase transition temperature moves to the low-temperature region for the mixed crystals. The transition temperature is also lowered under external pressure applied along a direction [11]. Taking into account that parameter a for the $\text{CsBi}(\text{MoO}_4)_2$ crystal is less than the corresponding parameter for the $\text{CsDy}(\text{MoO}_4)_2$ crystal, one may assume that doping of the dysprosium crystal results in effective crystal compression along a direction. In other words, impurity effect is qualitatively similar to the effect of uniaxial pressure. We have compared our data with those from Ref. [11].

For further considerations the Clausius–Clapeyron equation in the form $(\Delta P \cdot \Delta V)/L = \Delta T/T_{cr}$ was used. Here $\Delta P \cdot \Delta V = U$, where U is elastic deformation energy emerging at phase transition, L is latent heat at phase transition (jump of enthalpy $L = 0.64 \text{ kJ/mol}$ was earlier determined [13]), T_{cr} is the critical temperature of phase transition without the elastic deformation and ΔT is the change of T_{cr} at the corresponding U deformation.

For evaluation of the temperature T_{cr} we use the fact that a parameter changes in $\text{CsDy}(\text{MoO}_4)_2$ at T_{tr} (a parameter increases abruptly at T_{tr} , $\Delta a/a \approx 0.68\%$ [14]). The related *stretch* lattice deformation along a parameter is 0.3 kJ/mol [15]. It was determined using the simplified model of crystal consisting of alternating $[\text{Dy}(\text{MoO}_4)_2]^-$

layers and Cs^+ ions as well as data obtained for elastic modules from the spectra in Ref. [15]. Assuming that the phase transition occurs at $T_{tr} = T_{cr} - \Delta T = 42$ K, we estimate from Clausius–Clapeyron equation $\Delta T = 35$ K and therefore $T_{cr} = 77$ K. Supposing further that the averaged parameter a in the mixed crystals linearly changes when concentration x increases, we may construct the $T_{cr}(x)$ dependence.

The data from Ref. [11] do not contradict the evaluations presented. After our considerations the effective decrease of the a at Bi^{3+} content $x = 0.1$ is equivalent to the a parameter decrease under the external pressure about $3.6 \cdot 10^2$ kg/cm². For comparison the data from Ref. [11] are shown in Fig. 2. The dependence obtained in our experiments is steeper than that from Ref. [11]. It may be caused by action of the other mechanisms lowering the phase transition temperature. The limited dissolving of bismuth as we suppose is the result of the tendency of bismuth ions to change their valence at high temperatures during the crystal growing.

So we have shown that the external pressure and Bi^{3+} doping stabilize the high-temperature phase. Doping with Bi has little effect on the low-energy phonon spectra as well as on the low-energy electron levels position, though it essentially shifts the transition temperature. Note that the effect of uniform pressure does not explain in full the lowering of the phase transition temperature at Bi^{3+} doping. The additional mechanism of the effective shift of the T_{tr} to the low-temperature side is the result of *percolation* of the low dimension crystal structure with the bismuth ions.

It is well known that the transition temperature of the CJTE type phase transitions is rather sensitive to the action of the external magnetic field. Magnetic field effect on CJTE is possible due to rather strong magnetoelastic coupling between the Jahn–Teller centres; in our case Jahn–Teller centres are dysprosium ions surrounded by oxygen ligands. The transition temperature shift depends on the direction of applied magnetic field because of g -factor anisotropy of the Jahn–Teller centres ground state [16].

Experimental investigations of the external magnetic field influence on the cooperative Jahn–Teller ordering in $\text{KDy}(\text{MoO}_4)_2$ ($T_{tr} \approx 14$ – 15 K) (orthorhombic compound with a similar structure) have shown that at the definite value and direction of external magnetic field the Jahn–Teller ordering is destroyed and transition to non-ordered, or high-temperature phase takes place [16, 17]. Such investigations were undertaken for the $\text{CsDy}(\text{MoO}_4)_2$ crystal [10], but the critical magnetic field was not achieved in the experiments.

For further discussion of the magnetic field effect on the spectra we would take into account the feature of the crystal structure. It is known that the crystals consist of the $[\text{Dy}(\text{MoO}_4)_2]^-$ layered blocks weakly coupled by the alkali ion layers $[\text{Cs}]^+$ [18]. The Dy^{3+} ions chains, including two Dy^{3+} ions coupled by inversion, are considered as arrays formed inside the layers and therefore we take into account only one magnetically equivalent paramagnetic JT centre.

Our investigations as well as the former ones [19] allowed us to determine the values of g -factors of the ground state spectroscopy splitting. They turned out to be $g_a = 11$, $g_b = 1$, $g_c = 13$ for the low-temperature phase, where a , b , c are the ortho-

rhombic cell parameters. One can see that g -factor tensor for the low-temperature phase resembles the structure of g -factor tensor of the ground state for the high-temperature phase of $\text{KDy}(\text{MoO}_4)_2$ [16].

To evaluate the critical value of external magnetic field H_{cr} at which the high-temperature phase may be induced in the crystal at temperatures $T < T_{tr}$, we used the following model. In Figure 4, the positions of the ground levels are shown at $T > T_{tr}$ and $T < T_{tr}$ without external magnetic field (left side). The right side shows magnetic field effect on the levels. Here Δ is the energy of the Jahn–Teller stabilization [15]. If the g -factors are strongly different for the ground and excited electronic states, which are Kramers doublets, the mutual approaching of the levels starts when the external field is switched on. On the other hand, if the g -factors for the ground states of the low-temperature and high-temperature phases are strongly different, we can evaluate the effect of magnetic field on the ground state energy position. When the energy interval between the ground states in the external magnetic field equals to the sum of the spontaneous elastic energy originating in the crystal as a result of the phase transition and additional energy corresponding to the splitting of the ground state, the crystal changes its state and the high-temperature phase spectrum is observed. Taking into account that elastic energy U is about $U \approx 0.3\Delta$ [15] and the maximal g -factor difference for the ground states $\Delta g \approx 18 - 1 = 17$, we can evaluate the critical field H_c :

$$H_c = \frac{\Delta - U}{0.5\Delta g \mu_b}, \quad \mu_b = 9.2 \cdot 10^{-24} \text{ J/10 kOe}$$

Here $\Delta - U \cong 50 \text{ cm}^{-1} = 50 \cdot 1.99 \cdot 10^{-23} \text{ J}$, and we have $H_c = 128 \text{ kOe}$.

So we have shown that at H_{cr} the high-temperature phase may be induced in the low-temperature phase at $T \approx 0$. When magnetic field suppresses the elastic deformation accompanied with Jahn–Teller phase transition in $\text{CsDy}(\text{MoO}_4)_2$, it gives rise to the high-temperature phase in crystal. The maximal difference in the g -factor tensor components for the ground states in the low- and high-temperature phases was found for the magnetic field applied at 14° in ab plane [19].

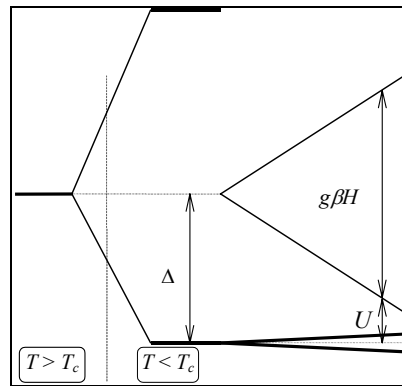


Fig. 4. Scheme of the Dy^{3+} ions energy levels splitting under external magnetic field for $\text{CsDy}(\text{MoO}_4)_2$

Note that by results of Ref. [15] the critical field at $T \approx 0$ was found for $H \approx 170$ kOe. The difference in the value reflects the fact that the magnetic field was applied in two cases at different directions according to the orthorhombic axes. But the value of the field which may destroy the low-temperature phase at a finite temperature, namely at $T \approx T_{tr}$, is much lower than H_c . The experimental shift of the external magnetic field value from 70 kOe to 170 kOe, when temperature is lowered from 42 K to 4.2 K, is not discussed in this paper, but is the question for the future work.

4. Conclusions

The comparison of the concentration dependence of the temperature of Jahn–Teller ordering type phase transition in $\text{CsDy}_{1-x}\text{Bi}_x(\text{MoO}_4)_2$ at low x with P – T phase diagram [11] allowed us to suppose that the effect of impurity compressing the $[\text{Dy}_{1-x}\text{Bi}_x(\text{MoO}_4)_2]$ layers correlates with the effect of the uniaxial pressure. We have observed the shift of T_{tr} to the low-temperature side without changing spectra of the low-temperature phase although the change of the crystal *average* size along a direction took place.

We can also suppose that in $\text{CsDy}(\text{MoO}_4)_2$ phase transition from the low-temperature phase to the high-temperature one may be induced by magnetic field. Estimated value of H_c corresponds to the magnetic field which leads to the transition of the crystal from the low- to the high-temperature phase when the crystal temperature T is about 0 K. The estimation that is based on the molecular field representations gave the value of the external magnetic field that induces this transition. The assumption concerning the lowering of the H_c critical value in the crystals doped by bismuth is quite realistic. Similar effect of the external magnetic field and pressure on the Jahn–Teller ordering in $\text{CsDy}(\text{MoO}_4)_2$ is the question to be necessarily studied further in more details.

References

- [1] KLEVTSOV P.V., KLEVTSOVA R.F., Zh. Strukt. Khimii, 18 (1977), 419.
- [2] VINOKUROV V.A., KLEVTSOV P.V., Kristallografiya, 17 (1972), 127.
- [3] ZVYAGIN A.I., ELCHANINOVA S.D., STETSENKO T.S., PELIKH L.N., KHATSKO E.N., Phys. Nizk. Temp., 1 (1975), 79.
- [4] FOMIN V.I., GNEZDILOV V.P., EREMENKO V.V., NESTERENKO N.M., Sov. Phys. Solid State, 31 (1989), 871.
- [5] ZVYAGIN A.I., KUTKO V.I., Fiz. Nizk. Temp., 13 (1987), 537.
- [6] MACZKA M., KOJIMA S., HANUZA J., J. Phys: Cond. Matter, 10 (1998), 8093.
- [7] ELCHANINOVA S.D., ZVYAGIN A.I., Fiz. Nizk. Temp., 9 (1983), 1200; Sov. J. Low Temp. Phys., 9 (1983), 619.
- [8] GURSKAS A.A., POPOV V.P., SOKOLOV A.G., NESTERENKO N.M., Izvestia AN SSSR, ser. fiz., 53 (1989), 1382.
- [9] NESTERENKO N.M., FOMIN V.I., KUTKO V.I., ZVYAGIN A.I., Preprint 26–82 of Institute for Low Temp. Phys. and Eng. (1982), 1–36.

- [10] ELCHANINOVA S.D., ZVYAGIN A.I., LITVINENKO YU.G., Phys. Tverd. Tela, 22 (1980), 3171.
- [11] SKOROBOGATOVA I.V., SAVCHENKO E.M., ZVYAGIN A.I., Izvestia Acad. Nauk SSSR, ser. fiz., 47 (1983), 491.
- [12] GERASHCHENKO S.S., MILOSLAVSKAYA O.V., KHARCHENKO YU.N., KUTKO V.I., NESTERENKO N.M., MACALIK L., HERMANOWICZ K., HANUZA J., J. Mol. Structure, 563 (2001), 359.
- [13] ANDERS E.YE., ZVYAGIN A.I., SHESTACHENKO L.S., Fiz. Nizk. Temp., 6 (1980), 1356.
- [14] ELCHANINOVA S.D., ZVYAGIN A.I., KOZEI Z.A., Fiz. Nizk. Temp., 8 (1982), 303.
- [15] KUTKO V.I., Low Temp. Phys., 24 (1998), 291.
- [16] LEASK M.J.M., TROPPER A.C., WELLS M.R., J. Phys. C, 14 (1981), 3481.
- [17] KHARCHENKO YU.N., Phys. Nizk. Temp., 22 (1996), 394.
- [18] KLEVTSOVA R.F., BORISOV S.W., Dokl. Akad. Nauk SSSR, 117 (1967), 1334.
- [19] ELCHANINOVA S.D., ANDERS A.G., ZVYAGIN A.I., KOBETS V.I., LITVINENKO YU.G., Phys. Nizk. Temp., 7 (1981), 187.

Received 16 June 2001
Revised 21 January 2002

(Ph₄P)₂[ReCl₅(tcm)] **– a new precursor of molecular magnets**

J. MAŁECKA, A. KOCHEL, J. MROZIŃSKI*

Faculty of Chemistry, University of Wrocław, F. Joliot-Curie 14, 50-383 Wrocław, Poland

New complex of composition (PPh₄)₂[ReCl₅(tcm)] have been obtained and characterized by IR, UV-Vis spectroscopies and magnetic measurements. The rhenium atom is six-fold co-ordinated with five chloride atoms and one tcm group. The compound contains tcm⁻ in monodentate function co-ordinated to metal via the N-atom. The temperature dependence of magnetic susceptibility measured over the range of 1.73–300 K showed the presence of a very weak antiferromagnetic interaction ($zJ' = -0.78 \text{ cm}^{-1}$) between the rhenium atoms.

Key words: *rhenium(IV), complex compound, magnetism, tcm ligand*

1. Introduction

The tricyanomethanide (tcm)⁻ ion presents itself as a rather efficient complexing agent. The tcm⁻ forms co-ordinate bonds with preservation of its planarity. The bonds are N-type metal-to-ligand ones as a consequence of the high electron density on the cyano nitrogen. The tcm⁻ ion shows a tendency to act as a bridge ligand and hence to form co-ordination polymers [1–8]. Because of the high degree of delocalization of the ionic charge, three cyano-N-atoms are equally capable of establishing co-ordinate bonds. This enables tricyanomethanide to act not only as a monodentate ligand but preferably as a bi-, tri- and tetradentate ligand in bridge function. Ag(tcm), which contains layers of two interpenetrating hexagonal sheets [9] upon reaction with (Ph₄P)₂ReCl₆ gives the complex (Ph₄P)₂[ReCl₅(tcm)]. The compound contains tcm⁻ in monodentate function co-ordinated to metal centre via the N-atom.

Rhenium(IV) ion (5d³) of the ground electronic state ⁴A_{2g} term has three unpaired electrons. The fourth oxidation state is particularly stable in association with classical ligands (predominantly σ-donors) and like other d³ ions, it adopts octahedral symmetry.

*Corresponding author; jmroz@wchuwr.chem.uni.wroc.pl.

2. Experimental section

2.1. Synthesis

A mixture of 1.20 g of $(\text{Ph}_4\text{P})_2\text{ReCl}_6$ (1.11 mmol) and 1.43 g of $\text{Ag}(\text{tcm})$ (7.23 mmol) was heated under reflux in 120 ml of acetonitrile ($t = 81\text{ }^\circ\text{C}$). The reaction was stopped after 30 hours. The solution was brown. The grey precipitate (0.81 g), mainly AgCl and unreacted starting material was filtered. To the brown solution *n*-hexane was added to precipitate the product. Yellow crystals of the final product were obtained by slow evaporation from a (1:3) *n*-hexane–2-butanone mixture. Anal. Calcd. for $\text{C}_{52}\text{H}_{40}\text{P}_2\text{Cl}_5\text{N}_3\text{Re}$: C, 55.1; H, 3.5; Cl, 15.7; N, 3.7; Re, 16.4 Found: C, 54.5; H, 3.5; Cl, 15.1; N, 3.2; Re, 15.7.

2.2. Physical measurements

Electronic (reflectance) spectra of undiluted sample of complex $(\text{Ph}_4\text{P})_2[\text{ReCl}_5(\text{tcm})]$ were recorded over the range of 200–800 nm with Hitachi 356 Double Beam Spectrophotometer.

The FIR spectra were measured in Nujol mull ($500\text{--}50\text{ cm}^{-1}$) and MIR spectra in KBr pellet ($4000\text{--}400\text{ cm}^{-1}$) with Bruker IFS 113V Spectrophotometer.

Magnetic susceptibility of the polycrystalline samples was measured over the temperature range of 1.73–300 K using Quantum Design SQUID-based magnetometer MPMS-XL5 type. The superconducting magnet was operated at the magnetic field strength ranging up to 5 kG.

The corrections for diamagnetism were estimated from Pascal constants [10]. The effective magnetic moment was estimated from the equation:

$$\mu_{\text{eff}} = 2.83 [\chi_M^{\text{corr}} T]^{1/2} \text{ B.M.}$$

2. Results and discussion

Proposed molecular structure of $[\text{ReCl}_5(\text{tcm})]^{2-}$ anion is shown in Fig. 1. The complex $(\text{Ph}_4\text{P})_2[\text{ReCl}_5(\text{tcm})]$ of symmetry C_{4v} has 11 normal modes of vibration: $\Gamma_{\text{vib}} = 4A_1 + 2B_1 + B_2 + 4E$ [11]. The type of bond of the tricyanomethanides is reflected in a characteristic way by the IR/Raman spectra of the compound, where most significant variations are observed in the range of the CN stretching vibration band. There are three $\nu(\text{CN})$ vibrations ($2A_1, E_1$) to be expected in metal-N-tricyanomethanides (local C_{2v} symmetry) and two expected $\nu(\text{CN})$ frequencies (A_1, E_1) in metal-C-tricyanomethanides (local C_{3v} symmetry). IR spectrum of $(\text{Ph}_4\text{P})_2[\text{ReCl}_5(\text{tcm})]$

complex shows two bands in the CN vibration region, at 2240 and 2172 cm^{-1} and a shoulder at 2189 cm^{-1} . It may be interpreted that A_1 and B_1 may possibly coincide.

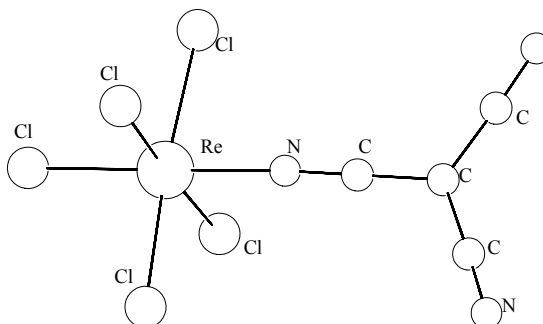


Fig. 1. Proposition of the molecular structure of $[ReCl_5(tcm)]^{2-}$ ion

It is found that, in passing from an octahedral $ML_6(O_h)$ to six co-ordinate square bipyramidal complexes $ML_5Z(C_{4v})$, the t_{2g} orbital splits into two sets: $b_2(xy)$, $e(xz, yz)$ and the e orbital into sets: $a_1(z^2)$, $b_1(x^2-y^2)$. Bands at 25 063 cm^{-1} (399 nm, $A = 0.85$), 29 412 cm^{-1} (340 nm, $A = 0.86$) and 31 270 cm^{-1} (320 nm, $A = 0.89$) of high absorption coefficients can be attributed to ligand metal charge transfer transitions: $N \rightarrow M$, $Cl \rightarrow M$ [12]. Other bands with lower absorption coefficients in the visible region are due to the ligand field (d-d) transitions. These are bands at 13 123 cm^{-1} (762 nm, $A = 0.36$), 14327 cm^{-1} (698 nm, $A = 0.35$), 21 008 cm^{-1} (476 nm, $A = 0.70$) which can be attributed to $b_2 \rightarrow e$ ($xy \rightarrow xz, yz$); $b_2 \rightarrow b_1$ ($xy \rightarrow x^2-y^2$); $e \rightarrow a_1$ ($xz, yz \rightarrow z^2$), respectively. On the basis of the transitions mentioned above and equations estimated for the d orbitals in a field of C_{4v} symmetry [13], $Dq = 1433$ cm^{-1} , $Dt = 277$ cm^{-1} , $Ds = -3913$ cm^{-1} parameters were calculated.

Bands observed in the UV region at 48 544 cm^{-1} (206 nm; $A = 0.96$) and 43 860 cm^{-1} (228 nm; $A = 0.96$) are characteristic of tcm^- [14].

The structure of $[ReCl_5(tcm)]^{2-}$ ion can be described as short square-bipyramid with the electron configuration $(b_2)^1(e)^2$. Such a configuration is also confirmed by the magnetic moment $\mu_{eff} = 3.29$ B.M. ($T = 300$ K) corresponding three unpaired electrons.

The reduction of magnetic moments in comparison with the spin only value (3.87 B.M.) can be explained on the basis of depopulation of spin-orbit coupled excited states and/or zero-field effects. The magnetic susceptibilities of other rhenium(IV) salts have been reported elsewhere [15–20].

Magnetic properties of complex $(Ph_4P)_2[ReCl_5(tcm)]$ under the form of $\chi_M T$ and χ_M vs. T (χ_M being the molar magnetic susceptibility) are plotted in Fig. 2.

To interpret quantitatively the susceptibility data, we used the approaches in which we considered that the magnetic susceptibility of this complex might be described by the susceptibility of the $^4A_{2g}$ term with zero-field splitting [21].

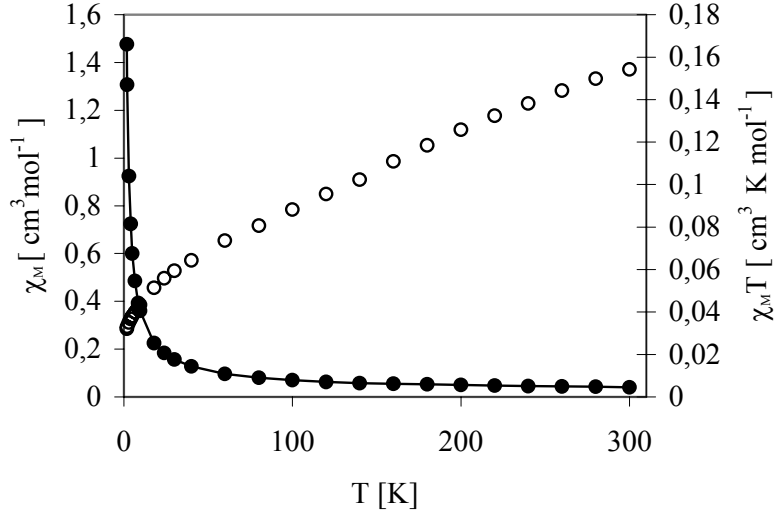


Fig. 2. Thermal dependence of χ_M (●) and $\chi_M T$ (○) for $(\text{Ph}_4\text{P})_2[\text{ReCl}_5(\text{tcm})]$ complex. Solid line is the calculated curve (Eq. (2), (3))

Zero-field splitting and ligand field of symmetry lower than cubic lead to the anisotropy of magnetic properties of an ion. The relevant spin Hamiltonian is defined by the equation:

$$H = D\left[S_z^2 - 1/3S(S+1)\right] + g_{\parallel}DH_zS_z + g_{\perp}B(H_xS_x + H_yS_y) \quad (1)$$

where DS_z^2 represents the splitting into two Kramers doublets in the absence of magnetic field. The parallel and perpendicular zero-field susceptibilities for $S = 3/2$ (Eq. (2)) were corrected by a factor predicted from the molecular field (Eq. (3)) [22]:

$$\chi_{\parallel} = \frac{N\beta^2}{4kT} g_{\parallel}^2 F_{D_{\parallel}}, \quad \chi_{\perp} = \frac{N\beta^2}{4kT} g_{\perp}^2 F_{D_{\perp}} \quad (2)$$

where

$$F_{D_{\parallel}} = \frac{1 + 9\exp\left(-\frac{2D}{kT}\right)}{1 + \exp\left(-\frac{2D}{kT}\right)}, \quad F_{D_{\perp}} = \frac{4 + 6\frac{kT}{2D}\left[1 - \exp\left(-\frac{2D}{kT}\right)\right]}{1 + \exp\left(-\frac{2D}{kT}\right)}$$

$2D$ is the zero-field parameter, N – Avogadro's number, g_{\perp} , g_{\parallel} – the spectroscopic splitting factors, β – the Bohr magneton and k – the Boltzmann constant:

$$\chi'_i = \frac{\chi_i}{1 - \left(\frac{2zJ'}{N g_i^2 \beta^2} \right) \chi_i} \quad (3)$$

where $i = \parallel$ or \perp , zJ' is the exchange parameter and was applied to calculate magnetic exchange effect by means of a molecular field.

Since our data refer to powdered samples, the average magnetic susceptibility is equal to $\chi_{av} = 1/3\chi_{\parallel} + 2/3\chi_{\perp}$. Minimization of the agreement factor R ($R = \Sigma(\chi_{exp} - \chi_{calc})^2 / \Sigma(\chi_{exp})^2$) leads to $2D = 30.47 \text{ cm}^{-1}$, $g_{av} = 1.65$, and $zJ' = -0.78 \text{ cm}^{-1}$ with $R = 8.95 \cdot 10^{-4}$.

A small value of the exchange parameter suggests the presence of very weak anti-ferromagnetic interactions between $[\text{ReCl}_5(\text{tcm})]^{2-}$ ions at crystal lattice. This fact confirm: the calculated in the interval 300–80 K the Curie constant value $C = 1.36 \text{ cm}^3 \cdot \text{K} \cdot \text{mol}^{-1}$ and negative value of the Weiss constant $\theta = -35.4 \text{ K}$. This magnetic interaction might be transmitted by bonding arrangements such as M–L...L–M [19]. The occurrence of a bulky $(\text{Ph}_4\text{P})^+$ cation results in the diamagnetic dilution due to increasing distance between the paramagnetic Re(IV) centres.

On the basis of magnetic data we conclude that Re(IV) in $(\text{Ph}_4\text{P})_2[\text{ReCl}_5(\text{tcm})]$ exhibits a large zero-field splitting parameter together with weak anti-ferromagnetic interactions, but we have obtained only twin crystals. After determination the structure of monocrystals of this complex, further discussion of its physicochemical properties will be possible.

Acknowledgements

This work was financially supported by the Polish State Committee for Scientific Research and European Science Foundation Programme *Molecular Magnets*.

References

- [1] HOSKINS B.F., ROBSON R., *J. Am. Chem. Soc.*, 112 (1990) 1546.
- [2] HIRSCH K.A., WILSON S.C., MOORE J.S., *Chem. Eur. J.*, 3 (1997) 765.
- [3] YAGHI O.M., DAVIS C.E., LI G., LI H., *J. Am. Chem. Soc.*, 119 (1997), 2861.
- [4] ZAWOROTKO M.J., *Chem. Soc. Rev.*, 23 (1994), 284.
- [5] CARLUCCI L., CIANI G., PROSERPIO D.M., SIRONI A., *J. Chem. Soc., Chem. Commun.*, (1994), 2755.
- [6] GOODGAME D.M., MENZER S., SMITH A.M., WILLIAMS D.J., *J. Chem. Soc., Dalton Trans.* (1997), 3213.
- [7] WITHERSBY M.A., BLAKE A.J., CHAMPNESS N.R., HUBBERSTEY P., LI W. S., *Angew. Chem. Int. Ed. Engl.*, 36 (1997), 2327.
- [8] MUNAKATA M., WU L.P., KURODA-SOWA T., MAEKAWA M., MORIWAKI K., KITAGAWA S., *Inorg. Chem.*, 36 (1997), 5416.
- [9] BATTEN S.R., HOSKINS B.F., ROBSON R., *New J. Chem.* (1998), 173.
- [10] KÖNIG E., *Magnetic Properties of Co-ordination and Organometallic Transition Metal Compounds*, Springer-Verlag, Berlin, 1966.

- [11] PREETZ W., RUF D., TENSFELDT D., *Z. Naturforsch.*, 39b (1984), 1100.
- [12] KLOPP U., PREETZ W., *Z. anorg. allg. Chem.*, 619 (1993), 1336.
- [13] LEVER A.B.P., *Inorganic Electronic Spectroscopy*, Elsevier, Amsterdam, 1984.
- [14] BOYD R.H., *J. Phys. Chem.*, 67 (1963), 737.
- [15] MROZIŃSKI J., *Proc. Conf. Coord. Chem.* 54 (1980), 293.
- [16] MROZIŃSKI J., *Bull. Acad. Polon. Sci. Ser. Chim.* 7 (1980), 559.
- [17] MROZIŃSKI J., *Bull. Acad. Polon. Sci. Ser. Chim.* 10 (1980), 789.
- [18] MAŁECKA J., JAGER L., WAGNER CH., MROZIŃSKI J., *Polish. J. Chem.*, 72 (1998), 1879.
- [19] TOMKIEWICZ A., VILLAIN F., MROZIŃSKI J., *J. Mol. Struc.*, 555 (2000), 383.
- [20] TOMKIEWICZ A., BARTCZAK T.J., KRUSZYŃSKI R., MROZIŃSKI J., *J. Mol. Struc.*, 595 (2001), 225.
- [21] FIGGIS B.N., *Trans Faraday Sce.* 56 (1960), 4745.
- [22] CHIOZZONE R., GONZÁLEZ R., KREMER C., DE MUNNO G., CANO J., LLORET F., JULVE M., FAUS J., *Inorg. Chem.*, 38 (1999), 4745.

Received 16 February 2002

Revised 24 April 2002

Determination of the photodynamic activity of porphyrins: Potential photosensitizers for treatment of age-related macular degeneration

CLÁUDIO R. NERI, ANA PAULA J. MAESTRIN PRADO, ANDERSON O. RIBEIRO, OS-
VALDO A. SERRA, YASSUKO IAMAMOTO

Laboratory of Rare Earths/Bioinorganic, Department of Chemistry, FFCLRP University of São Paulo
– Brazil, Av. Bandeirantes 3900, CEP 14040-901, Ribeirão Preto, SP, Brazil

Age-related macular degeneration (AMD) is the leading cause of irreversible visual loss in people between 65 and 74 years. Recently, the photodynamic therapy (PDT) is used as experimental treatment for exudative AMD. In a PDT process, a reaction takes place when a photosensitizer (PS), light of appropriated wavelength, and oxygen are present at the same time. In general, the PS are porphyrins and related systems. The aim of this study was to evaluate the photodynamic activity (PA) of the benzoporphyrin (BPH₂), protoporphyrin-IX (Proto), tetrakis(*p*-hydroxyphenyl)porphyrin (THPPH₂) and tetrakis(2-hydroxy-5-nitrophenyl)porphyrin (T2H5NPPH₂). The PA is related to quantum yields (ϕ_A) for the singlet oxygen (¹O₂) production. Uric acid, a known singlet oxygen scavenger, is utilised as a chemical dosimeter in the PDT. When the uric acid (UA) and PS solution is irradiated with laser light, the UA band absorbance at 293 nm decreases as a rapid evaluation of relative PA of the PS.

Key words: *porphyrins, photodynamic activity, age-related macular degeneration*

1. Introduction

The photodynamic therapy (PDT) is one of the more promising new modalities currently being explored for use in the control and treatment of tumors. PDT is based on the use of a light-sensitive molecule, photosensitizer (PS). Porphyrins, phtalocyanines and chlorins, represent a major class of PS agents useful in an array of medical areas, including oncology, cardiology, ophthalmology, dermatology, immunology, gynecology and urology [1, 2].

Age-related macular degeneration (AMD) is the leading cause of irreversible visual loss. Laser photocoagulation of choroidal neovascular membranes (CNVMs) in AMD is currently the only well-studied and widely accepted treatment modality. But,

the basic premise of PDT is that, through the use of an intravascular compound that causes vascular occlusion by a photochemical reaction, as occurs with laser photocoagulation. Two treatment strategies can be envisioned. First, vessels may be occluded through a purely photodynamic mechanism. Second, photosensitizers may be used to enhance laser photocoagulation ablation of choroidal neovascular membranes thus decreasing rates of persistence, decreasing the thermal energy necessary to achieve occlusion [3].

The red absorption maxima of porphyrins and related compounds allow the activating light to penetrate deeper into tissue. It has been shown that oxygen plays a fundamental role in photochemistry of the many photosensitising drugs used in PDT. When the PS is irradiated in the presence of oxygen, the energy transfer from the excited triplet state of a PS to molecular oxygen leads to generation of singlet oxygen ($^1\text{O}_2$), the (excited) singlet state of molecular oxygen from otherwise benign precursors ($^3\text{O}_2$). This seems to be the first step in the photodynamic action of the most PS used in PDT. Then $^1\text{O}_2$ reacts with cellular targets leading to cell death.

Optimizing the PDT and photodetection of early cancer in a clinical context involves the variation of several parameters, such as the drug dose, light dose, light dose rate, time delay between drug injection and light application, wavelength of excitation of the dye, as well as the chemical purity and stability of the PS and their photodynamic activity [4].

Uric acid, a known singlet oxygen scavenger, is utilised as a chemical dosimeter for the determination of photodynamic activity in the PDT. The PA is related to quantum yields (ϕ_A) for the singlet oxygen ($^1\text{O}_2$) production. When the acid uric (UA) and PS solution is irradiated with laser light, the UA band absorbance at 293 nm decreases as a rapid evaluation of relative PA of the photosensitizer. Based on UA test it is possible to define a photodynamic activity scale, which may be a tool comparing the PA of different photosensitizers or irradiation conditions a proposal for a photodynamic activity scale based on the uric acid test. Fischer investigated the photodynamic activity and used the following relation [5]:

$$PA = \frac{\Delta A_{UA} \cdot 10^5}{E_0 t A_{PS \lambda_{irr}}} \quad (1)$$

where PA is the photodynamic activity ($\text{m}^2/(\text{W}\cdot\text{s})$), ΔA_{UA} – UA absorbance decrease at 293 nm in UA and PS solution after irradiation, E_0 – power density of laser (W/m^2), t – irradiation time (s), $A_{PS \lambda_{irr}}$ – absorbance of PS in UA and PS solution after irradiation [5].

In this work, we determined the PA of the benzoporphyrin (BPH_2), protoporphyrin-IX (Proto), tetrakis(p-hydroxyphenyl)porphyrin (THPPH_2), and tetrakis(2-hydroxy-5-nitrophenyl)porphyrin (T2H5NPPH_2) by modified Fischer's expression using the uric acid (UA) test [4, 5]. Irradiations were performed at 683 nm using an MMD-Optics Laser with the power of 50 mW.

2. Experimental

Materials: Uric acid (UA) was purchased from Merck. Dimethylformamide anhydrous (DMF) and ethanol were purchased from Mallinckrodt. Benzoporphyrin (BPH₂), protoporphyrin-IX (Proto) and tetrakis(*p*-hydroxyphenyl)porphyrin (THPPH₂) were obtained from MidCentury. The precursor tetrakis(2-hydroxy-5-nitrophenyl)porphyrin (T2H5NPPH₂) was synthesized in our laboratory [6] using Adler Longo method. All reagents were used without further purification.

Uric acid test [5]: The samples were irradiated in a quartz cell with solutions containing only PS (10^{-5} mol·dm⁻³) and solutions containing UA (10^{-3} mol·dm⁻³) and a PS (10^{-5} mol·dm⁻³). The irradiations were made at 25 °C for 1 hour, in air-saturated solution. Before and during the irradiation, absorbance spectra were registered each 3 min with a HP 8543 spectrophotometer. The UA procedure was used to investigate the UA absorbance decrease with different irradiation wavelengths in the wavelength range of each PS (BPH₂, Proto, THPPH₂ and T2H5NPPH₂).

Photodynamic activity scale (PA): Based on UA test it is possible to define photodynamic activity scale of different photosensitizers. The data obtained for PS could be mathematically determined by the modified Fischer's expression (2) All laser light is focused into the sample solution.

$$PA = \frac{\Delta A_{UA} \cdot 10^5}{W t A_{PS \lambda_{irr}}} \quad (2)$$

where: PA is the photodynamic activity (1/(mW·s)), ΔA_{UA} – UA absorbance decrease at 293 nm in UA and PS solution after irradiation, W – laser power (mW), t – irradiation time (s), $A_{PS \lambda_{irr}}$ – absorbance of PS in UA and PS solution after irradiation.

3. Results and discussion

The samples were irradiated in a quartz cell with solutions containing only PS (10^{-5} mol·dm⁻³) and solutions containing UA (10^{-3} mol·dm⁻³) and PS (10^{-5} mol·dm⁻³). The PS absorbance did not decrease in the absence of uric acid. The UA has two absorption maxima in the UV/Vis range of the spectrum – 231 and 293 nm (Fig. 1). The parameters (irradiation wavelength, laser power, irradiation time and PS concentration) remained constant.

The absorbance spectrum of the porphyrins containing UA: T2H5NPPH₂, THPPH₂, Proto, and BPH₂, before and after laser irradiation, are shown in Figs. 2–5.

After laser irradiation at 683 nm, the photodegradation of uric acid was observed by changing the concentration of the solutions containing the PS. The PA values were determined by the Fischer's expression modification (2) and are shown in the table.

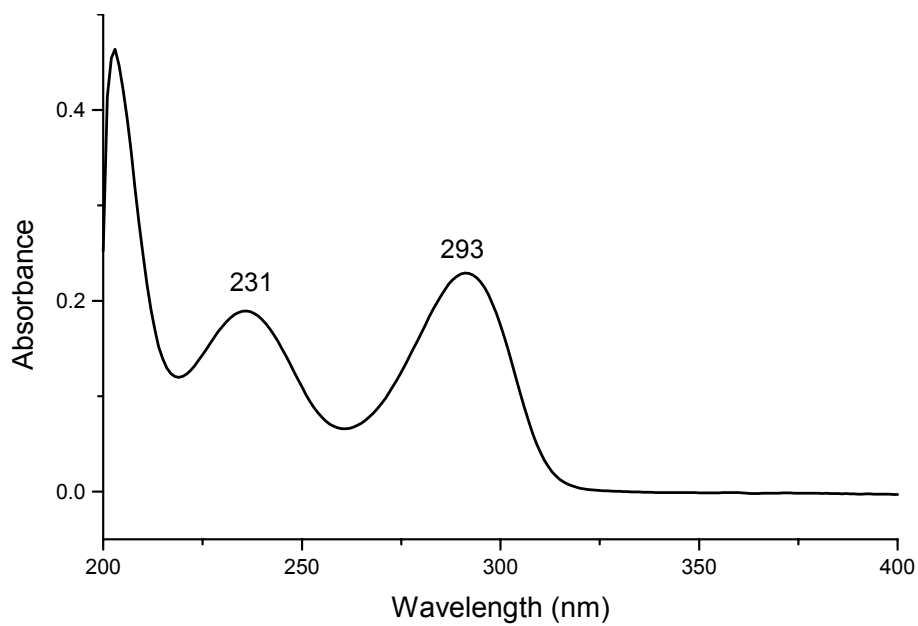
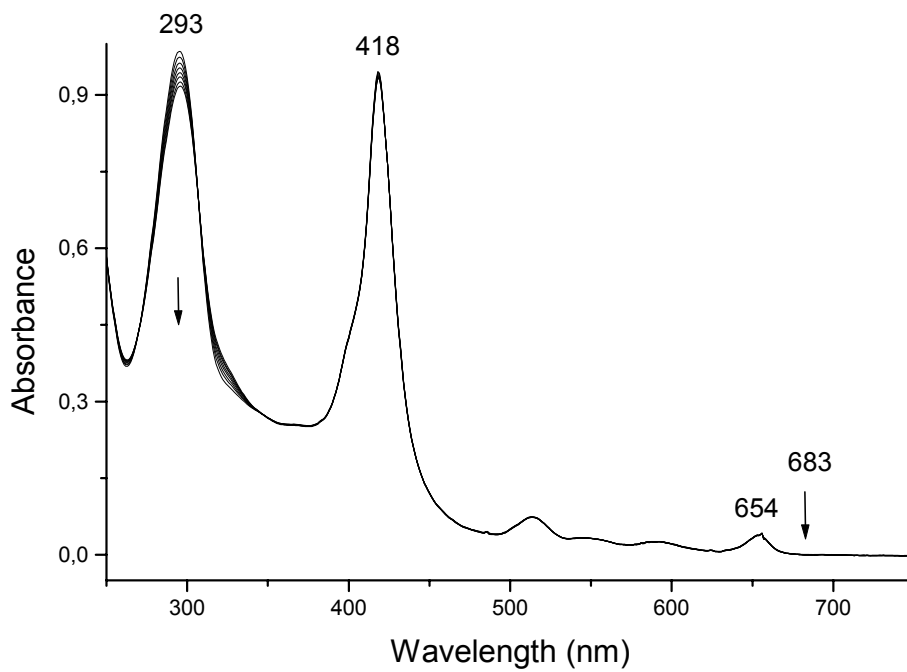


Fig. 1. Absorption spectrum of UA in ethanol

Fig. 2. Absorption spectrum of UA and T2H5NPPH₂ in ethanol

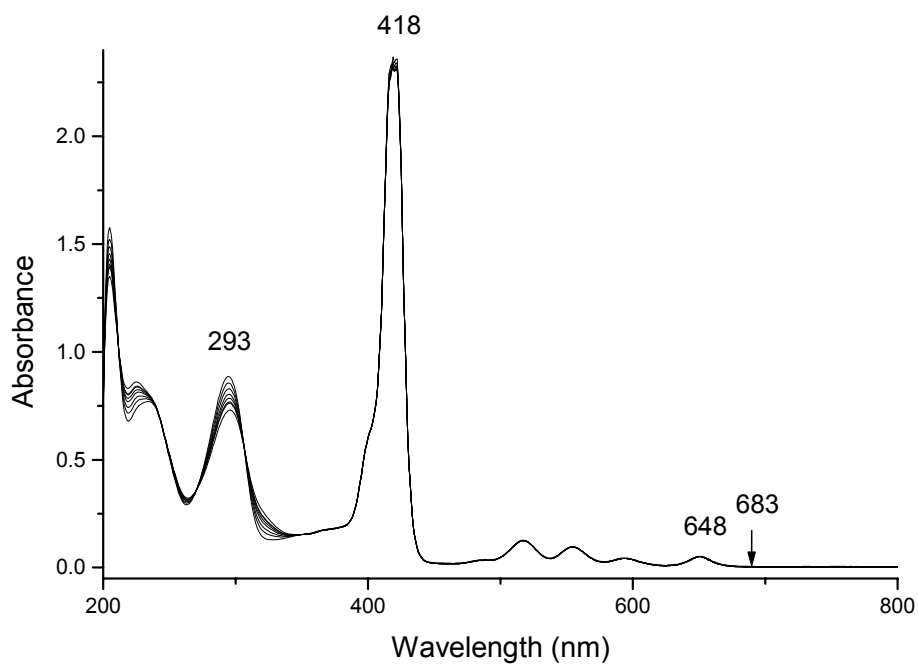


Fig. 3. Absorption spectrum of UA and THPPH₂ in ethanol

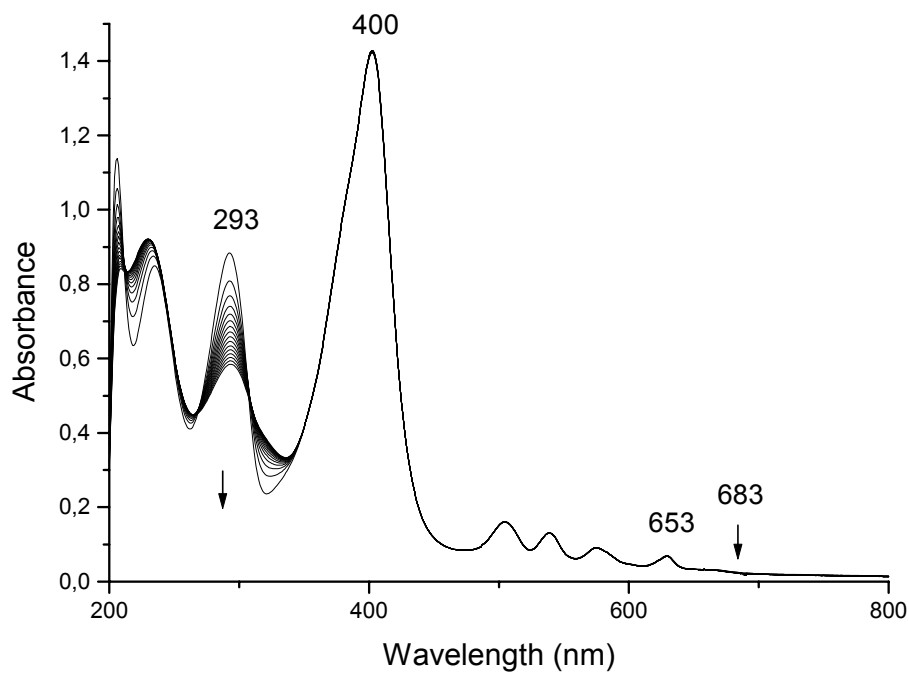


Fig. 4. Absorption spectrum of UA and Proto in ethanol

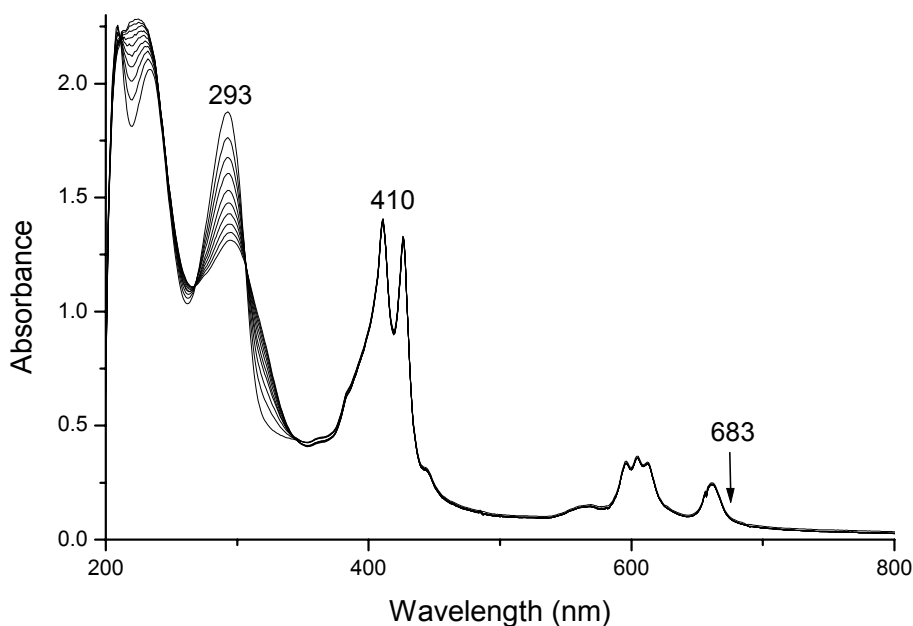


Fig. 5. Absorption spectrum of UA and BPH₂ in ethanol

Table. PA values determined by the Fischer's modification expression to T₂H₅NPPH₂, THPPH₂, Proto and BPH₂ in ethanol

Porphyrine	ΔA_{AU}	t/s	$A_{PS\lambda_{irr}}$	PA
T2H5NPPH ₂	0.070	4200	$2.99 \cdot 10^{-4}$	111
THPPH ₂	0.159	4200	$1.03 \cdot 10^{-3}$	74
Proto	0.279	4200	$2.24 \cdot 10^{-3}$	59
BPH ₂	0.672	4200	$1.10 \cdot 10^{-2}$	29

4. Conclusion

The uric acid test is a suitable tool for a rapid and simple relative determination of the photodynamic activity of the photosensitizers: T2H5NPPH₂, THPPH₂ and Proto in ethanol solutions. It presents a good stability and high values of PA even with a low absorption coefficient at 683 nm. Based on the UA test, it was possible to define a photodynamic activity scale, and compare the relative PA of the different photosensitizers:

$$T2H5NPPH_2 > THPPH_2 > Proto > BPH_2$$

Because the reproducibility of the UA test depends on reproducibility of the environmental and irradiation conditions and reproducibility of PS properties [5]: The presence of the NO₂ and OH groups bounded to the phenyl is responsible for the high stability of the T2H5NPPH₂.

References

- [1] MODY T. D., PANDEY R. K., *J. Porphyrins and Phtalocyanines*, 5 (2001), 103.
- [2] STERNBERG E. D., DOLPHIN D., *Tetrahedron*, 54 (1998), 4151.
- [3] CIULLA T. A., DANIS R. P., HARRIS A., *Surv. Ophthalmol.* 43, 2 (1998), 134.
- [4] ANDREJEVIC S., SAVARY J. F., MONNIER PH., C. FONTOLLIET, D BRAICHOTTE, G. WAGNIÈRES, VAN DEN BERGH H., *J. Photochemistry and Photobiology B: Biology* 36 (1996), 143.
- [5] FISCHER F., GRANCHEW G., SINN H-J., MAIER-BORST W., LORENZ W.J. SCHLAG P.M., *Clinica Chimica Acta*, 274 (1998), 89.
- [6] NERI C.R., MAESTRIN A.P.J., SERRA O.A., VI Encontro Latino Americano de Fotoquímica e Fotobiologia ELAFOT, Teresópolis, Brasil (1999), 12.

Received 16 June 2001
Revised 19 December 2001